

Invited Lecture An Introduction to Cavitation Fundamentals

Christopher E. Brennen
California Institute of Technology, Pasadena, California, USA
brennen@caltech.edu

ABSTRACT

In this opening lecture I will summarize some of the fundamentals of cavitation in the hope that this will allow attendees greater insight into the more advanced lectures which follow. Whether your primary interest is in the turbomachinery field or in the biological and bioengineering contexts in which cavitation is important these fundamentals are important in understanding the observed phenomena.

NOMENCLATURE

A_0	Initial radius of the cloud of bubbles.
A_N	Nuclei capture streamtube area
C_{PMIN}	Minimum pressure coefficient in the flow
f	Frequency
$G(f)$	Spectral density function
I	Acoustic impulse
I^*	Dimensionless acoustic impulse
l	Reference length in the flow
k	Polytropic index
N	Nuclei concentration
n^*	Event rate
p_a	Radiated acoustic pressure
p_s	Acoustic pressure
p_B	Bubble pressure
p_{oo}	Reference pressure
p_v	Vapor pressure
r	Radial Coordinate
R	Bubble radius
R_E	Equilibrium radius of the bubbles
R_H	Headform radius
R_0	Initial radius of the bubbles
R_m	Maximum bubble radius
R_N	Nuclei radius
R	Distance from source
S	Surface tension
t	Time
T_{oo}	Reference temperature
U_{oo}	Reference velocity
V	Bubble volume
T_{oo}	Reference temperature
α_0	Initial void fraction in the cloud.
β	Interaction parameter, $\propto A^2/R^2$ Also a coefficient in section 7

ν_L	Liquid kinematic viscosity
ρ_L	Liquid density
σ	Cavitation number
σ_i	Cavitation inception number
ω_N	Bubble natural frequency
ω_n	Cloud natural frequencies
ω	Radian frequency

1. INTRODUCTION

We begin where cavitation begins namely with the tiny nuclei which grow into observable cavitation bubbles for they hold the key to some of the complications in dealing with the phenomena. We then follow the growth and collapse of cavitation bubbles or other structures as they experience a low pressure episode followed by a pressure recovery. In doing so we will survey the various forms that the bubbles may take as well as phenomena they exhibit.

2. NUCLEATION

When a pure liquid is subjected to a pressure below its vapor pressure (at a given, uniform temperature) it is said to be *under tension*. If there is no vapor present, that state of tension can be stable and, like a solid, a pure liquid can sustain very large negative pressures without rupturing and forming vapor voids. This is not as surprising as it may seem when one considers that a liquid is very similar to a solid in terms of its density and intermolecular forces. Indeed the theoretical tension which a pure liquid (or solid) can sustain is of the order of 3×10^4 to 3×10^5 atmospheres [1]. Of course, in practice, pure solids cannot reach this level of tension and they yield at values about 100 times less because of stress concentrations and other imperfections within their structure. Liquids are similar except that the weaknesses that lower the achievable tension can take various different forms. One of these forms of weakness is the chance formation of small temporary gaps between molecules caused by random thermal motions of the molecules. The process of vapor bubble formation by this mechanism is called *homogeneous nucleation* and the corresponding limiting tension can be predicted by kinetic theory. Another potential weaknesses can

occur at the interface between the liquid and a solid in contact with the liquid. This is termed *heterogeneous nucleation*. Sometimes the solid surface may be that of the containing vessel or it may be a small suspended particle. Thirdly, a liquid can contain very small gas bubbles (microbubbles) which are stabilized by surface tension effects (supplemented sometimes by contaminant molecules) but which grow into macroscopic vapor bubbles under a sufficiently large tension. A fourth type of weakness is that caused by radiation from the outside. A collision between a high energy cosmic particle and a molecule of the liquid can deposit sufficient energy to initiate nucleation when it would otherwise have little chance of occurring. Such, of course, is the principal of the bubble chamber.

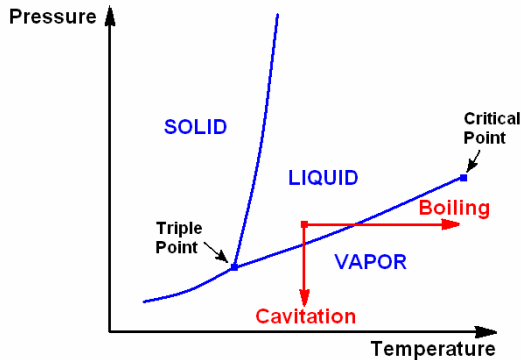


Figure 1. Phase diagram for a simple substance like water where the blue line between the triple point and the critical point is the saturated vapor/liquid line.

Each of these types of weakness will have a level of tension at which they will cause rupture of the liquid and the subsequent formation of vapor bubbles. The weakness that will first cause rupture will be that which requires the lowest tension. However, the relative tensions of each weakness will depend on the specific liquid, the specific thermodynamic state (pressure and temperature) and the specifics of the microbubbles and/or nucleation sites at the containing boundaries. There are certainly liquids which manifest homogeneous nucleation because the tension at which it occurs is smaller than that required to grow the microbubbles present in the liquid. However, this review will confine itself to the case of water (or aqueous solutions) at normal temperatures and pressures and it transpires that, in these circumstances, the tensions needed for homogeneous nucleation are much larger than those needed to grow the naturally occurring microbubbles. Consequently the dominant weaknesses are micron-sized bubbles (microbubbles) of contaminant gas, which could be present in crevices within the solid boundary or within suspended particles or could simply be freely suspended within the liquid. In water, microbubbles of air seem to persist almost indefinitely and are almost impossible to remove completely. They resist being dissolved completely, perhaps because of contamination of the interface.

We use the term *boiling* to refer to a process in which we change the thermodynamic state of a liquid by heating it at relatively constant pressure as shown by the horizontal arrow in figure 1. On the other hand the formation of bubbles resulting from depressurization at relatively constant temperature (the vertical arrow) is called *cavitation* (Note that the tension would be the vertical distance below the saturated vapour/liquid line at which cavitation occurs). Thermodynamically boiling and cavitation are identical for the path taken in crossing the saturated vapor/line line is of little consequence.

However, there are practical differences caused by the fact that while it is feasible to uniformly change the pressure throughout a large volume of liquid, it is very difficult to uniformly change the temperature. Thus boiling normally involves heating the liquid at a boundary and therefore the nucleation sites which are first activated are those at that boundary since the temperature is greatest there. On the other hand cavitation usually occurs in the body of a liquid. Consequently the most vulnerable nucleation sites in most cavitation processes in water are either microbubbles or solid particles containing microbubbles in crevices. Both are termed cavitation nuclei and are the nucleation sites for most aqueous cavitation phenomena. Many studies focus on methods for measuring these nuclei and on the effects that these nuclei have on the observed cavitation phenomena. Typical measurements of cavitation nuclei in water tunnels and in the ocean are shown in Figure 2. Note that most of the relevant nuclei

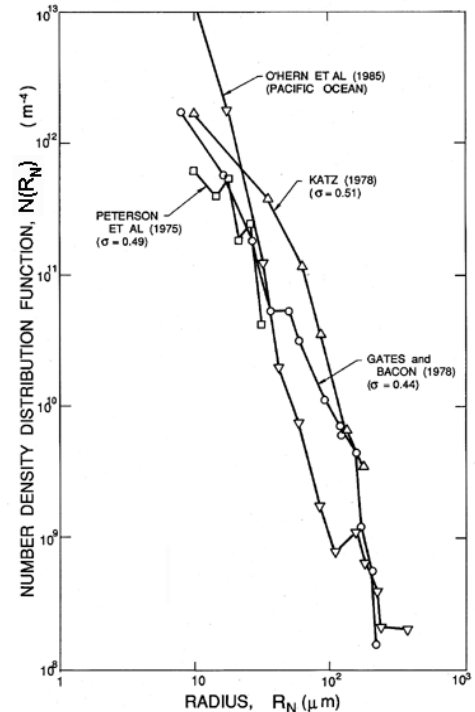


Figure 2. Cavitation nuclei number density distribution functions measured by holography in three different water tunnels (Peterson *et al.* [2], Gates and Bacon [3], Katz [4]) at the cavitation numbers, σ , as shown) and in the ocean off Los Angeles, Calif. (O'Hern *et al.* [5]).

range from about 5 μm to 100 μm in size. Smaller bubbles are stabilized by surface tension while the population of larger bubbles is very small since they tend to rise up and out of the liquid.

In most conventional engineering contexts, the prediction and control of nucleation sites is very uncertain even when dealing with a simple liquid like water. In other fluids such as cryogenic liquids or in complex biological substances, there is a much greater dearth of information.

3. CAVITATION INCEPTION

For cavitation in flowing systems it is conventional to characterize how close the pressure in the liquid flow is to the vapor pressure (and therefore the potential for cavitation) by means of the cavitation number, σ , defined as $\sigma = 2(p_{\infty} - p_v)/\rho_L U_{\infty}^2$ where U_{∞} , p_{∞} and T_{∞} are respectively a reference velocity, pressure and temperature in the flow (usually upstream quantities), ρ_L is the liquid density and $p_v(T_{\infty})$ is the saturated vapor pressure.

In a particular flow as σ is reduced, cavitation will first be observed to occur at some particular value of σ called the incipient cavitation number and denoted by σ_i . Further reduction in σ below σ_i would cause an increase in the number and size of the vapor bubbles. Suppose that prior to cavitation inception, the magnitude of the lowest pressure in the single phase flow is given by the minimum value of the coefficient of pressure, C_{pmin} . Note that C_{pmin} is a *negative* number and that its value could be estimated from either experiments or calculations of the single phase flow. Then, if cavitation inception were to occur when the minimum pressure reaches the vapor pressure it would follow that the value of the critical inception number, σ_i , would be simply given by

$$\sigma_i = -C_{pmin}.$$

Unfortunately, many factors can cause the actual values of σ_i to depart radically from $-C_{pmin}$ and much research has been conducted to explore these departures because of the importance of determining σ_i accurately. Among the important factors are

- the ability of the liquid to sustain a tension so that bubbles do not grow to observable size until the pressure falls a finite amount below the vapor pressure. The magnitude of this tension is a function of the nuclei present in the liquid.
- the fact that cavitation nuclei require a finite residence time in which to grow to observable size.
- the fact that measurements or calculations usually yield a minimum coefficient of pressure that is a time-averaged value. On the other hand many of the flows with which one must deal in practice are turbulent and, therefore, nuclei in the middle of turbulent eddies may experience pressures below the vapor pressure even when

the mean pressure is greater than the vapor pressure.

Moreover, since water tunnel experiments designed to measure σ_i are often carried out at considerably reduced scale, it is also critical to know how to scale up these effects to accurately anticipate inception at the full scale.

A detailed examination of these effects is beyond the scope of this presentation and the reader is referred to Knapp, Daily and Hammitt [6], Acosta and Parkin [7], Arakeri [8] and Brennen [9] for further discussion.

4. BUBBLE GROWTH

Once initiated the growth and collapse of a bubble containing gas and vapor in reduced pressure surroundings will be governed by the Rayleigh-Plesset equation or variations of it. This connects the instantaneous bubble radius, $R(t)$, to the prevailing pressure, $p_{\infty}(t)$, far from the bubble:

$$\frac{p_B(t) - p_{\infty}(t)}{\rho_L} = R \frac{d^2 R}{dt^2} + \frac{3}{2} \left(\frac{dR}{dt} \right)^2 + \frac{4\nu_L}{R} \frac{dR}{dt} + \frac{2S}{\rho_L R}$$

where ν_L is the liquid kinematic viscosity and S is the surface tension. A number of assumptions were made in deriving this equation including bubble spherical symmetry and that the thermal effects discussed later are negligible. Clearly the Rayleigh-Plesset equation is quite non-linear and solutions of it display features caused by that non-linearity. While bubble growth tends to be a fairly steady (though often explosive) as sketched in Figure 3, collapse tends to be catastrophic and to terminate in a minute bubble in which the non-condensable gas is so highly compressed that the adiabatic heating is substantial (see below).

It will be useful to develop an estimate of the maximum size to which a cavitation bubble grows during its trajectory through a region where the pressure is below the vapor pressure. In a typical external flow around a body characterized by the dimension, ℓ , it follows from the Rayleigh-Plesset equation that the rate of growth is roughly given by

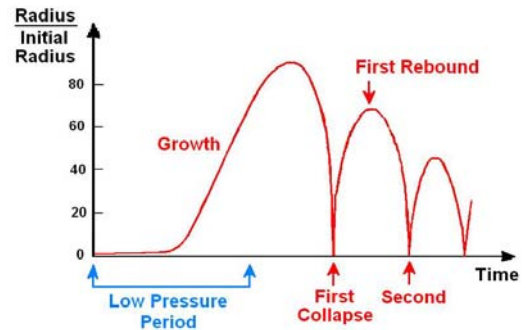


Figure 3. Typical bubble radius response to an episode of low pressure according to the Rayleigh-Plesset equation.

$$\frac{dR}{dt} = U_{\infty}(-\sigma - C_{pmin})^{\frac{1}{2}}$$

It should be emphasized this equation implies explosive growth of the bubble, in which the volume is increasing like t^3 .

To obtain an estimate of the maximum size to which the cavitation bubble grows, R_m , a measure of the time it spends below vapor pressure is needed. Assuming that the pressure distribution near the minimum pressure point is roughly parabolic [9] the length of the region below vapor pressure will be proportional to

$$\ell(-\sigma - C_{pmin})^{\frac{1}{2}}$$

and therefore the time spent in that region will be the same quantity divided by U_{∞} . The result is that an estimate of maximum size, R_m , is

$$R_m \approx 2\ell(-\sigma - C_{pmin})$$

where the factor 2 comes from the more detailed analysis of Brennen [9]. Note that, whatever their initial size, all activated nuclei grow to roughly the same maximum size because both the asymptotic growth rate and the time available for growth are essentially independent of the size of the original nucleus. For this reason all of the bubbles in a bubbly cavitating flow grow to roughly the same size independent of the size of the initial nucleus [9].

5. THERMAL EFFECTS

The above discussion (and the quoted version of the Rayleigh-Plesset equation) assumed that no significant temperature differences were generated in the liquid during growth. This is only the case in some liquids at lower temperatures (for example, water at normal temperatures). In other liquids or at higher temperatures, temperature differences develop between the bulk of the liquid and the vapor/liquid interface which substantially alter and inhibit the growth rate. This is termed the *thermal effect* or *thermodynamic benefit* for, by inhibiting growth, it reduces the deleterious effects of cavitation. The primary effect is caused by the major increase in the vapor density with increasing temperature. At low temperatures, the low vapor density means that only a small mass of liquid needs to be vaporized in order to allow bubble growth and this results in only minor cooling of the interface and therefore only a minor depression in the bubble temperature, pressure and growth rate. The effects become much greater at higher liquid temperatures. In water significant thermal effects do not usually begin until the temperature exceeds about 60°C. In cryogenic liquids they can be very important.

6. BUBBLE NATURAL FREQUENCIES

One derivation from the above Rayleigh-Plesset equation which is useful to mention is the natural frequency of oscillation of a single bubble in an infinite liquid domain. By examining the relation between small amplitude pressure perturbations and the linearized oscillations in the bubble radius that those pressure

fluctuations produce, it is readily shown that the bubble has a natural frequency, ω_N , given by

$$\omega_N = \left[\frac{1}{\rho_L R_E^2} \left\{ 3k(\bar{p}_{\infty} - p_V) + 2(3k - 1) \frac{S}{R_E} \right\} \right]^{\frac{1}{2}}$$

where R_E is the mean or equilibrium radius of the bubble, $(p_{\infty} - p_V)$ is the mean liquid pressure minus vapor pressure and k is a polytropic index for the non-condensable gas in the bubble. This yields natural frequencies typified by those for water in Figure 4. Notice that bubbles in the range 10 μ m to 100 μ m have natural frequencies in the range 10 to 100kHz.

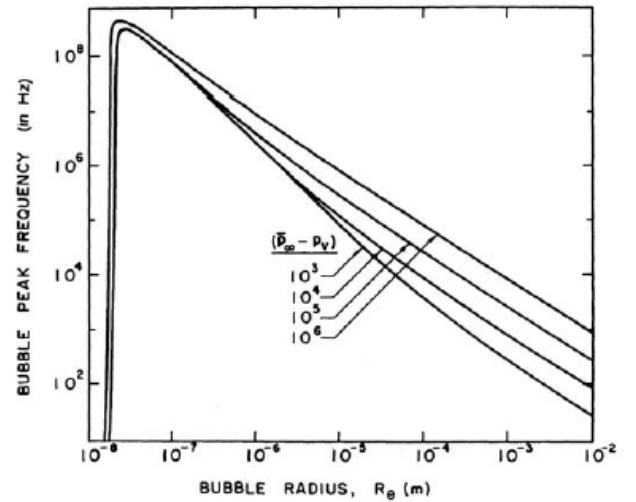


Figure 4. Bubble resonant frequencies in water at 300°K as a function of the radius of the bubble for various pressure levels, $(p_{\infty} - p_V)$.

7. CAVITATION BUBBLE COLLAPSE

One of the important non-linear effects in bubble dynamics is that vapor or cavitation bubble collapse in the absence of thermal effects can lead to very large interface velocities and very high localized pressures. This violence has important technological consequences for it can damage nearby solid surfaces in critical ways. Here we briefly review the fundamental processes associated with the phenomena of cavitation bubble collapse. For further details, the reader is referred to more specialized texts such as Knapp *et al.* [10], Young [11] or Brennen [9].

Integration of the Rayleigh-Plesset equation allows approximate evaluation of the magnitudes of the velocities, pressures, and temperatures generated by cavitation bubble collapse under a number of assumptions including that the bubble remains spherical. Though it will be later described that collapsing bubbles do not remain spherical, the spherical analysis provides a useful starting point. When a cavitation bubble grows from a small nucleus to many times its original size, the collapse will begin at a maximum radius, R_m , with a

partial pressure of gas, p_{Gm} , that is very small indeed. In a typical cavitating flow R_m is of the order of 100 times the original nuclei size, R_o . Consequently, if the original partial pressure of gas in the nucleus was about 1bar the value of p_{Gm} at the start of collapse would be about 10^{-6} bar. Using a typical value of the liquid pressure decrease causing cavitation, it can be demonstrated [9] that the maximum bubble pressure generated in the first collapse would be about 10^{10} bar and the maximum temperature would be 4×10^4 times the ambient temperature! Many factors, including the diffusion of gas from the liquid into the bubble and the effect of liquid compressibility, mitigate this result. Nevertheless, the calculation illustrates the potential for the generation of high pressures and temperatures during collapse and the potential for the generation of shock waves and noise. Early work on collapse by Herring [12], Gilmore [13]] and others focused on the inclusion of liquid compressibility in order to learn more about the production of shock waves in the liquid generated by bubble collapse. Modifications to the Rayleigh-Plesset equation that would allow for liquid compressibility were developed and these are reviewed by Prosperetti and Lezzi [12]. A commonly used variant is that proposed by Keller and Kolodner [13].

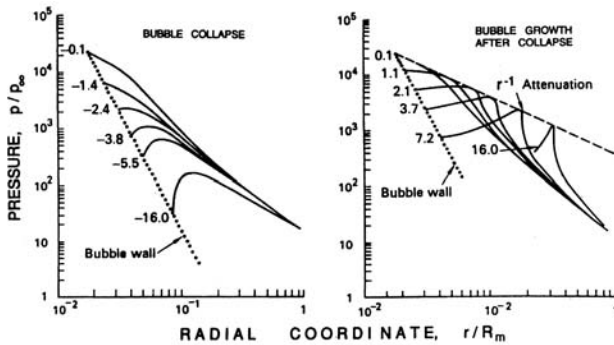


Figure 5. Typical results of Hickling and Plesset [14] for the pressure distributions in the liquid before collapse (left) and after collapse (right) (without viscosity or surface tension). The values attached to each curve are proportional to the time before or after the minimum size

However, as long as there is some non-condensable gas present in the bubble to decelerate the collapse, the primary importance of liquid compressibility is not the effect it has on the bubble dynamics (which is slight) but the role it plays in the formation of shock waves during the rebounding phase that follows collapse. Hickling and Plesset [14] were the first to make use of numerical solutions of the compressible flow equations to explore the formation of pressure waves or shocks during the rebounding phase that follows collapse. Figure 5 presents an example of their results for the pressure distributions in the liquid before (left) and after (right) the moment of minimum size. The graph on the right clearly shows the propagation of a pressure pulse or shock away from the bubble following the minimum size. As indicated in that figure, Hickling and Plesset concluded

that the pressure pulse exhibits approximately geometric attenuation (like r^{-1}) as it propagates away from the bubble. Other numerical calculations have since been carried out by Ivany and Hammitt [15], Tomita and Shima [16], and Fujikawa and Akamatsu [17], among others.

Even if thermal effects are negligible for most of the collapse phase, they play a very important role in the final stage of collapse when the bubble contents are highly compressed by the inertia of the in-rushing liquid. The pressures and temperatures that are predicted to occur in the gas within the bubble during spherical collapse are very high indeed. Since the elapsed times are so small (of the order of microseconds), it would seem a reasonable approximation to assume that the noncondensable gas in the bubble behaves adiabatically. Typical of the adiabatic calculations is the work of Tomita and Shima [16] who obtained maximum gas temperatures as high as 8800°K in the bubble center. Such elevated temperatures and pressures only exist for a fraction of a microsecond but they can produce remarkable effects such as sonoluminescence, flashes of light during bubble collapse.

All of the above analyses assume spherical symmetry. We will now focus attention on the stability of shape of a collapsing bubble before continuing discussion of the origins of cavitation damage.

8. SHAPE DISTORTION DURING BUBBLE COLLAPSE

Like any other accelerating liquid/gas interface, the surface of a bubble is susceptible to Rayleigh-Taylor instability [18,19]. As expected a bubble is most unstable to non-spherical perturbations when it experiences the large, positive values of d^2R/dt^2 that occur during the last stage of collapse. This has several different consequences. When the bubble surroundings are strongly asymmetrical (for example the bubble is close to a solid wall or a free surface) the dominant perturbation that develops is a re-entrant jet. Of particular interest for cavitation damage is the fact that a nearby solid boundary can cause a re-entrant microjet directed toward that boundary. The surface of the bubble furthest from the wall accelerates inward more rapidly than the side close to the wall and this results in a high-speed re-entrant microjet that penetrates the bubble and can achieve very high speeds. Such microjets were first observed experimentally by Naude and Ellis [20] and Benjamin and Ellis [21]. The series of photographs shown in figure 6 represent a good example of the experimental observations of a developing re-entrant jet. Figure 7 presents a comparison between the re-entrant jet development in a bubble collapsing near a solid wall as observed by Lauterborn and Bolle [23] and as computed by Plesset and Chapman [24].

Note also that depth charges rely for their destructive power on a re-entrant jet directed toward the submarine upon the collapse of the explosively generated bubble.

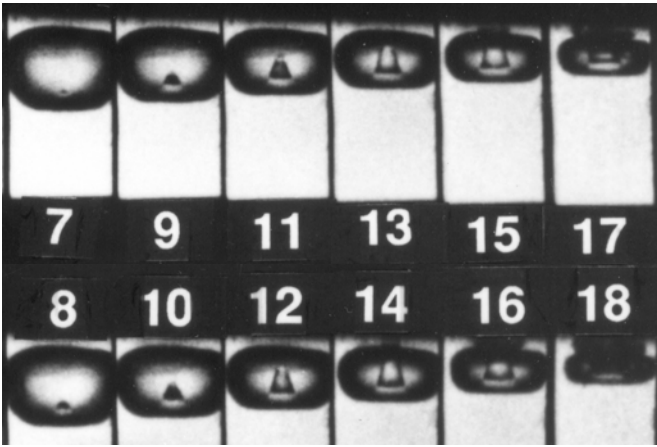


Figure 6. Series of photographs showing the development of the microjet in a bubble collapsing very close to a solid wall (at top of frame). The interval between the numbered frames is $2\mu\text{s}$ and the frame width is 1.4mm [22].

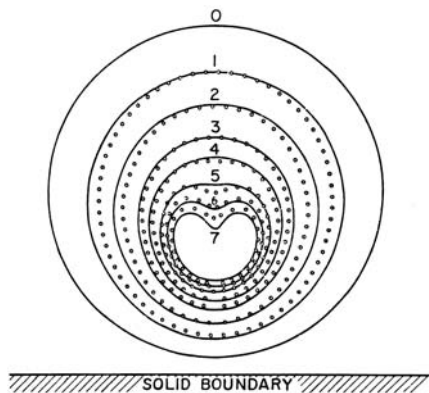


Figure 7. The collapse of a cavitation bubble close to a solid boundary in a quiescent liquid. The theoretical shapes of Plesset and Chapman [24] (solid lines) are compared with the experimental observations of Lauterborn and Bolle [23] (points) [25].

Other strong asymmetries can also cause the formation of a re-entrant jet. A bubble collapsing near a free surface produces a re-entrant jet directed away from the free surface [26]. Indeed, there exists a critical flexibility for a nearby surface that separates the circumstances in which the re-entrant jet is directed away from rather than toward the surface. Gibson and Blake [27] demonstrated this experimentally and analytically and suggested flexible coatings or liners as a means of avoiding cavitation damage. Another possible asymmetry is the proximity of other, neighboring bubbles in a finite cloud of bubbles. Chahine and Duraiswami [28] showed that the bubbles on the outer edge of such a cloud will tend to develop jets directed toward the center of the cloud.



Figure 8. Photographs of an ether bubble in glycerine before (left) and after (center and right) a collapse and rebound, both bubbles being about 5-6mm across [29].

When there is no strong asymmetry, the analysis of the Rayleigh-Taylor instability shows that the most unstable mode of shape distortion can be a much higher-order mode. These higher order modes can dominate when a vapor bubble collapses far from boundaries. Thus observations of collapsing cavitation bubbles, while they may show a single vapor/gas volume prior to collapse, just after minimum size the bubble appears as a cloud of much smaller bubbles. An example of this is shown in figure 8.

Brennen [9] shows how the most unstable mode depends on two parameters representing the effects of surface tension and non-condensable gas in the bubble. That most unstable mode number was later used in one of several analyses seeking to predict the number of fission fragments produced during collapse of a cavitating bubble [30].

9. CAVITATION DAMAGE

Perhaps the most ubiquitous engineering problem caused by cavitation is the material damage that cavitation bubbles can cause when they collapse in the vicinity of a solid surface. Consequently, this subject has been studied quite intensively for many years (see, for example, ASTM [31], Thiruvengadam [32, 33], Knapp, Daily, and Hammitt [6]). The problem is a difficult one because it involves complicated unsteady flow phenomena combined with the reaction of the particular material of which the solid surface is made. Though there exist many empirical rules designed to help the engineer evaluate the potential cavitation damage rate in a given application, there remain a number of basic questions regarding the fundamental mechanisms involved. Cavitation bubble collapse is a violent process that generates highly localized, large-amplitude shock waves and microjets. When this collapse occurs close to a solid surface, these intense disturbances generate highly localized and transient surface stresses. With softer material, individual pits caused by a single bubble collapse are often observed. But with the harder materials used in most applications it is the repetition of the loading due to repeated collapses that causes local surface fatigue failure and the subsequent detachment of pieces of material. Thus cavitation damage to metals usually has the crystalline appearance of fatigue failure. The damaged runner and pump impeller in figures 9 and 10 are typical examples.

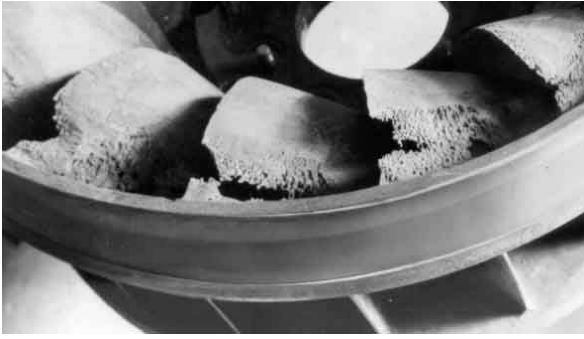


Figure 9. Major cavitation damage to the blades at the discharge from a Francis turbine.



Figure 10. Photograph of localized cavitation damage on the blade of a mixed flow pump impeller made from an aluminum-based alloy.

The issue of whether cavitation damage is caused by microjets or by shock waves generated when the remnant cloud of bubble reaches its minimum volume (or by both) has been debated for many years. In the 1940s and 1950s the focus was on the shock waves generated by spherical bubble collapse. When the phenomenon of the microjet was first observed, the focus shifted to studies of the impulsive pressures generated by microjets. First Shima *et al.* [34] used high speed Schlieren photography to show that a spherical shock wave was indeed generated by the remnant cloud at the instant of minimum volume. About the same time, Fujikawa and Akamatsu [17] used a photoelastic material so that they could simultaneously observe the stresses in the solid and measure the acoustic pulses and were able to confirm that the impulsive stresses in the material were initiated at the same moment as the acoustic pulse. They also concluded that this corresponded to the instant of minimum volume and that the waves were not produced by the microjet. Later, however, Kimoto [35] observed stress pulses that resulted both from microjet impingement and from the remnant cloud collapse shock.

The microjet phenomenon in a quiescent fluid has been extensively studied analytically as well as experimentally. Plesset and Chapman [24] numerically calculated the distortion of an initially spherical bubble as it collapsed close to a solid boundary and, as figure 7 demonstrates, their profiles are in good agreement with

the experimental observations of Lauterborn and Bolle [23].

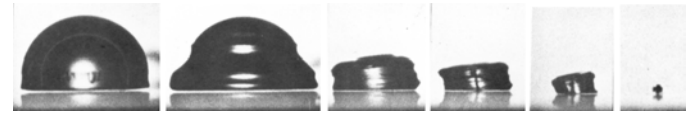


Figure 11. Series of photographs of a hemispherical bubble collapsing against a wall showing the *pancaking* mode of collapse [21].

It must also be noted that there are many circumstances in which it is difficult to discern a microjet. Some modes of bubble collapse near a wall involve a *pancaking* mode exemplified by the photographs in figure 11 and in which no microjet is easily recognized.

Finally, it is important to emphasize that virtually all of the observations described above pertain to bubble collapse in an otherwise quiescent fluid. A bubble that grows and collapses in a flow is subject to other deformations that can significantly alter its collapse dynamics, modify or eliminate the microjet and alter the noise and damage potential of the collapse process. In the next section some of these flow deformations will be illustrated.

10. CAVITATION BUBBLES IN FLOWS

We end our brief survey of the dynamics of cavitating bubbles with some experimental observations of single bubbles (single cavitation *events*) in real flows for these reveal the complexity of the micro-fluid-mechanics of individual bubbles. The focus here is on individual events springing from a single nucleus. The interactions between bubbles at higher nuclei concentrations will be discussed later.

Pioneering observations of individual cavitation events were made by Knapp and his associates at the California Institute of Technology in the 1940s (see, for example, Knapp and Hollander [36]) using high-speed movie cameras capable of 20,000 frames per second. Shortly thereafter Plesset [37], Parkin [38], and others began to model these observations of the growth and collapse of traveling cavitation bubbles using modifications of Rayleigh's original equation of motion for a spherical bubble. However, observations of real flows demonstrate that even single cavitation bubbles are often highly distorted by the pressure gradients in the flow.

Ceccio and Brennen [39] and Kuhn de Chizelle *et al.* [40,41] have made an extended series of observations of cavitation bubbles in the flow around axisymmetric bodies, including studies of the scaling of the phenomena. The observations at lower Reynolds numbers are exemplified by the photographs of bubble profiles in figure 12 and 13. In all cases the shape during the initial growth phase is that of a spherical cap, the bubble being separated from the wall by a thin layer of liquid of the same order of magnitude as the boundary

layer thickness. Later developments depend on the geometry of the headform and the Reynolds number. In some cases as the bubble enters the region of adverse pressure gradient, the exterior frontal surface is pushed inward, causing the profile of the bubble to appear wedge-like. Thus the collapse is initiated on the exterior frontal surface of the bubble, and this often leads to the bubble fissioning into forward and aft bubbles as seen in figure 12.



Figure 12. A series of photographs illustrating, in profile, the growth and collapse of a traveling cavitation bubble in a flow around a 5.08cm diameter headform at $\sigma = 0.45$ and a speed of 9m/s. The sequence is top left, top right, bottom left, bottom right, the flow is from right to left. The lifesize width of each photograph is 0.73cm [39].

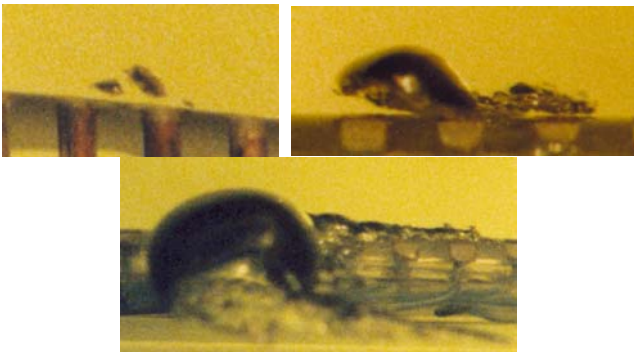


Figure 13. Examples of bubble fission (upper left), the instability of the liquid layer under a traveling cavitation bubble (upper right) and the attached tails (lower) [39] from experiments with a 5.08cm diameter ITTC headform at $\sigma = 0.45$ and a speed of 8.7m/s. The flow is from right to left. The lifesize widths of the photographs are 0.63cm, 0.80cm and 1.64cm respectively.

At the same time, the bubble acquires significant spanwise vorticity through its interactions with the boundary layer during the growth phase. Consequently, as the collapse proceeds, this vorticity is concentrated and the bubble evolves into one (or two or possibly more) short cavitating vortices with spanwise axes. These vortex bubbles proceed to collapse and seem to rebound as a cloud of much smaller bubbles.

Ceccio and Brennen [39] (see also Kumar and Brennen [42]) conclude that the flow-induced fission prior to collapse can have a substantial effect on the noise produced.



Figure 14. Typical cavitation events from the scaling experiments of Kuhn de Chizelle *et al.* [41] showing transient bubble-induced patches, the left one occurring on a 50.8cm diameter Schiebe headform at $\sigma = 0.605$ and a speed of 15m/s, the right one on a 25.4cm headform at $\sigma = 0.53$ and a speed of 15 m/s. The flow is from right to left. The lifesize widths of the photographs are 6.3cm (left) and 7.6cm (right).

Two additional phenomena were observed. In some cases the layer of liquid underneath the bubble would become disrupted by some instability, creating a bubbly layer of fluid that subsequently gets left behind the main bubble (see figure 13). Second, it sometimes happened that when a bubble passed a point of laminar separation, it triggered the formation of local *attached cavitation* streaks at the lateral or spanwise extremities of the bubble, as seen in figure 13. Then, as the main bubble proceeds downstream, these *streaks* or *tails* of attached cavitation are stretched out behind the main bubble, the trailing ends of the tails being attached to the solid surface. Tests at much higher Reynolds numbers (Kuhn de Chizelle *et al.* [40,41]) revealed that these events with tails occurred more frequently and would initiate attached cavities over the entire wake of the bubble as seen in figure 14. Moreover, the attached cavitation would tend to remain for a longer period after the main bubble had disappeared. Eventually, at the highest Reynolds numbers tested, it appeared that the passage of a single bubble was sufficient to trigger a patch of attached cavitation (figure 14, right), that would persist for an extended period after the nucleus had long disappeared.

In summary, cavitation bubbles are substantially deformed and their dynamics and acoustics altered by the flow fields in which they occur. This necessarily changes the noise and damage produced by those cavitation events.

11. CAVITATION NOISE

The violent and catastrophic collapse of cavitation bubbles results in the production of noise that is a consequence of the momentary large pressures that are generated when the contents of the bubble are highly compressed. Consider the flow in the liquid caused by the unsteady volume, $V(t)$, of a growing or collapsing cavity. In the far field the flow will approach that of a

simple source/sink, and will therefore be associated with a radiated acoustic pressure, $p_a(t)$, given by

$$p_a = \frac{\rho_L}{4\pi R} \frac{d^2V}{dt^2}$$

where we denote the distance from the cavity center to the point of measurement by R (for a more thorough treatment see Dowling and Ffowcs Williams [43] and Blake [44]). Thus the noise pulse generated at bubble collapse occurs because of the very large and positive values of d^2V/dt^2 when the bubble is close to its minimum size. It is conventional (see, for example, Blake [44]) to present the sound level using a root mean square pressure or *acoustic* pressure, p_s , defined by

$$p_s^2 = \overline{p_a^2} = \int_0^\infty G(f) df$$

and to represent the distribution over the frequency range, f , by the spectral density function, $G(f)$.

To the researcher or engineer, the crackling noise that accompanies cavitation is one of the most evident characteristics of the phenomenon. The onset of cavitation is often detected first by this noise rather than by visual observation of the bubbles. Moreover, for the practical engineer it is often the primary means of detecting cavitation in devices such as pumps and valves. Indeed, several empirical methods have been suggested that estimate the rate of material damage by measuring the noise generated (for example, Lush and Angell [45]).

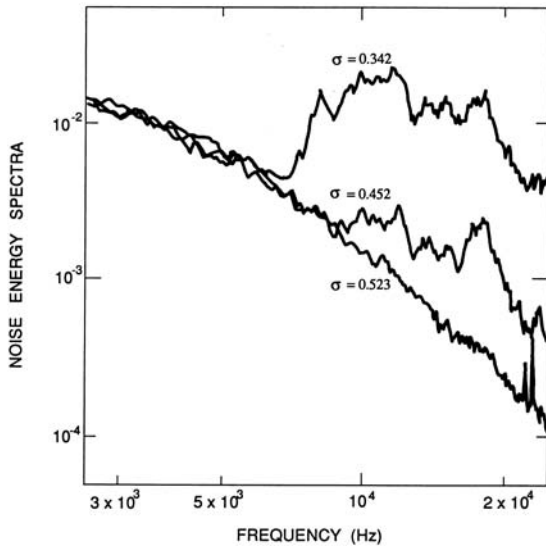


Figure 15. Acoustic power spectra from a model spool valve operating under noncavitating ($\sigma=0.523$) and cavitating ($\sigma=0.452$ and 0.342) conditions (from the investigation of Martin *et al.* [49]).

The noise due to cavitation in the orifice of a hydraulic control valve is typical, and spectra from such

an experiment are presented in figure 15. The lowest curve at $\sigma=0.523$ represents the turbulent noise from the noncavitating flow. Below the incipient cavitation number (about 0.523 in this case) there is a dramatic increase in the noise level at frequencies of about 5kHz and above. The spectral peak between 5kHz and 10kHz corresponds closely to the expected natural frequencies of the nuclei present in the flow (see above). Most of the analytical approaches to cavitation noise build on knowledge of the dynamics of collapse of a single bubble. Fourier analyses of the radiated acoustic pressure due to a single bubble were first visualized by Rayleigh [46] and implemented by Mellen [47] and Fitzpatrick and Strasberg [48].

Since the volume of the bubble increases from near-zero to a finite value and then returns to near-zero, it follows that for frequencies less than the inverse of the time for this process, the Fourier transform of the volume is independent of frequency. Consequently d^2V/dt^2 will be proportional to f^2 and therefore $G(f)$ is proportional to f^4 [48]. This is the origin of the left-hand asymptote in figure 16.

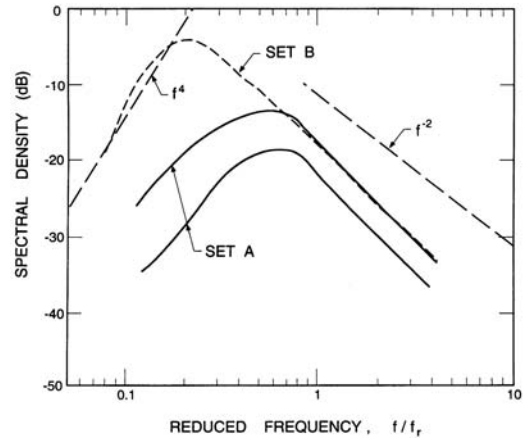


Figure 16. Acoustic power spectra of the noise from a cavitating jet. Shown are mean lines through two sets of data constructed by Blake and Sevik [51] from the data by Jorgensen [50]. Typical asymptotic behaviors are also indicated. The reference frequency, f_r , is $(p_{\infty}/\rho_L d^2)^{1/2}$ where d is the jet diameter.

The behavior at intermediate frequencies has been the subject of more speculation and debate. Mellen [47] and others considered the typical equations governing the collapse of a spherical bubble in the absence of thermal effects and noncondensable gas and concluded that, since the velocity dR/dt is proportional to $R^{-3/2}$, it follows that R is proportional to $t^{2/5}$. Therefore the Fourier transform of d^2V/dt^2 leads to the asymptotic behavior of $G(f)$ proportional to $f^{2/5}$. The error in this analysis is the neglect of the noncondensable gas. When this is included and when the collapse is sufficiently advanced, the behavior is quite different. Moreover, the values of d^2V/dt^2 are much larger during

this rebound phase, and therefore the frequency content of the rebound phase will dominate the spectrum. It is therefore not surprising that the $f^{2/5}$ is not observed in practice. Rather, most of the experimental results seem to exhibit an intermediate frequency behavior like f^1 or f^2 . Jorgensen [50] measured the noise from submerged, cavitating jets and found a behavior like f^2 at the higher frequencies; however, most of the experimental data for cavitating bodies or hydrofoils exhibit a weaker decay. The data by Arakeri and Shangumanathan [54] from cavitating headform experiments show a very consistent f^1 trend over almost the entire frequency range, and very similar results have been obtained by Ceccio and Brennen [39].

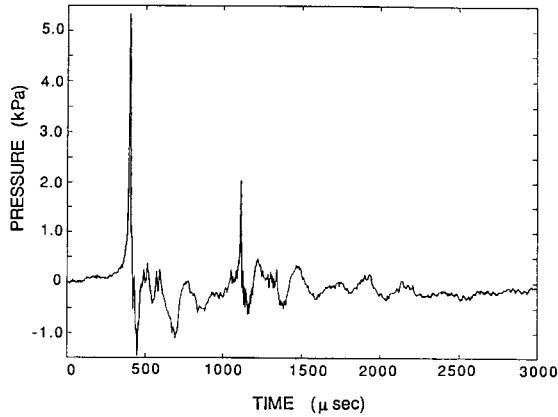


Figure 17. A typical acoustic signal from a single collapsing bubble [39].

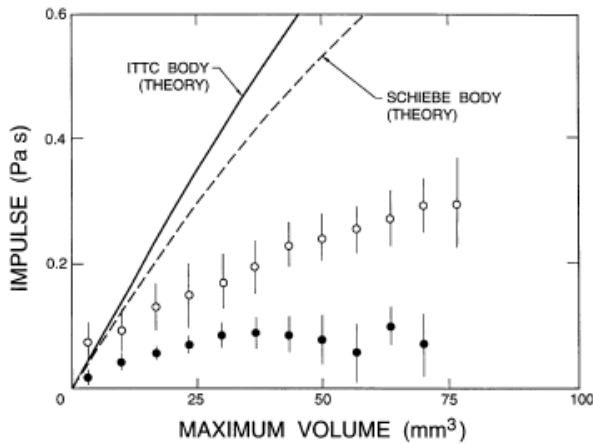


Figure 18. Comparison of the acoustic impulse, I , produced by the collapse of a single cavitation bubble on two axisymmetric headforms as a function of the maximum volume prior to collapse. Open symbols: Schiebe body; closed symbols: ITTC body; vertical lines indicate one standard deviation. Also shown are the corresponding results from the solution of the Rayleigh-Plesset equation [39].

Ceccio and Brennen [39] recorded the noise from individual cavitation bubbles in a flow and a typical

acoustic signal from their experiments is reproduced in figure 17. The large positive pulse at about 450 μ s corresponds to the first collapse of the bubble. This first pulse in figure 17 is followed by some facility-dependent oscillations and by a second pulse at about 1100 μ s. This corresponds to the second collapse that follows the rebound from the first collapse.

A good measure of the magnitude of the collapse pulse is the acoustic impulse, I , defined as the area under the pulse or

$$I = \int_{t_1}^{t_2} p_a dt$$

where t_1 and t_2 are times before and after the pulse at which p_a is zero. For later purposes we also define a dimensionless impulse, I^* , as

$$I^* = 4\pi IR / \rho_L U \ell^2$$

where U and ℓ are the reference velocity and length in the flow. The average acoustic impulses for individual bubble collapses on two axisymmetric headforms (ITTC and Schiebe bodies) are compared in figure 18 with impulses predicted from integration of the Rayleigh-Plesset equation. Since these theoretical calculations assume that the bubble remains spherical, the discrepancy between the theory and the experiments is not too surprising. Indeed one interpretation of figure 18 is that the theory can provide an order of magnitude estimate and an upper bound on the noise produced by a single bubble. In actuality, the departure from sphericity produces a less focused collapse and therefore less noise.

The next step is to consider the synthesis of cavitation noise from the noise produced by individual cavitation bubbles or events. If the impulse produced by each event is denoted by I and the number of events per unit time is denoted by n^* , the sound pressure level, p_s , will be given by $p_s = I n^*$. Consider the scaling of cavitation noise that is implicit in this construct. Both the experimental results and the analysis based on the Rayleigh-Plesset equation indicate that the nondimensional impulse, I^* , produced by a single cavitation event is strongly correlated with the maximum volume of the bubble prior to collapse and is almost independent of the other flow parameters. It follows [9] that

$$I^* = \frac{1}{U \ell^2} \left\{ \left(\frac{dV}{dt} \right)_{t_2} - \left(\frac{dV}{dt} \right)_{t_1} \right\}$$

and the values of dV/dt at the moments $t=t_1, t_2$ when $d^2V/dt^2=0$ may be obtained from the Rayleigh-Plesset equation. If the bubble radius at the time t_1 is denoted by R_x and the coefficient of pressure in the liquid at that moment is denoted by C_{px} , then

$$I^* \approx 8\pi \left(\frac{R_x}{\ell} \right)^2 (C_{px} - \sigma)^{\frac{1}{2}}$$

Numerical integrations of the Rayleigh-Plesset equation for a range of typical circumstances yield $R_x/R_m \sim 0.62$ where R_m is the maximum volumetric radius and that

$$(C_{px} - \sigma) \propto R_m/\ell$$

(in these calculations ℓ was the headform radius) so that

$$I^* \approx \beta \left(\frac{R_m}{\ell} \right)^{\frac{5}{2}}$$

The aforementioned integrations of the Rayleigh-Plesset equation yield the factor of proportionality, β , of about 35. On the other hand the experimental data on I^* [39, 40, 41] suggest a maximum value of β of about 4. We note that a quite similar relation between I^* and R_m/ℓ emerges from the analysis by Esipov and Naugol'nykh [52] of the compressive sound wave generated by the collapse of a gas bubble in a compressible liquid.

Consequently, the evaluation of the impulse from a single event is completed by an estimate of R_m such as that presented earlier. Since that estimate has R_m independent of U for a given cavitation number, it follows that I is linear with U . The event rate, n^* , can be considerably more complicated to evaluate than might at first be thought but begins with an evaluation of all the nuclei of concentration N (number per unit volume) flowing through an appropriate streamtube of cross-sectional area, A_N , with velocity, U_{oo} , so that $n^* = NAU_{oo}$. Then

$$PS \approx \frac{\beta}{3} \rho_L U_{\infty}^2 A_N N R_H^2 (-\sigma - C_{pmin})^{\frac{5}{2}} / R$$

where we have omitted some of the constants of order unity. For the relatively simple flows considered here, this equation yields a sound pressure level that scales with U_{oo}^2 and with ℓ^4 because A_N is proportional to ℓ^2 . This scaling with velocity does correspond roughly to that which has been observed in some experiments on traveling bubble cavitation, for example, those of Blake, Wolpert, and Geib [53] and Arakeri and Shangumanathan [54]. The former observe that p_s is proportional to U_{oo}^m where $m = 1.5$ to 2 . Different scaling laws will apply when the cavitation is generated by turbulent fluctuations such as in a turbulent jet (see, for example, Franklin and McMillan [55]). Then the typical tension experienced by a nucleus as it moves along a disturbed path in a turbulent flow is very much more difficult to estimate. Consequently, the models for the sound pressure due to cavitation in a turbulent flow and the scaling of that sound with velocity are less well understood.

12. CLOUD CAVITATION

In many cavitating liquid flows, when the number and concentration of the bubbles exceeds some critical level, the flow becomes unsteady and large clouds of cavitating bubbles are periodically formed and then collapse when convected into regions of higher pressure. This phenomenon is known as cloud cavitation and when it occurs it is almost always associated with a substantial increase in the cavitation noise and damage. We note that sometimes the clouds are large as in breaking waves and large shed vortices (Figure 19). But they can also be small, for example due to fission of a single collapsed cavitation bubble (Figure 8).

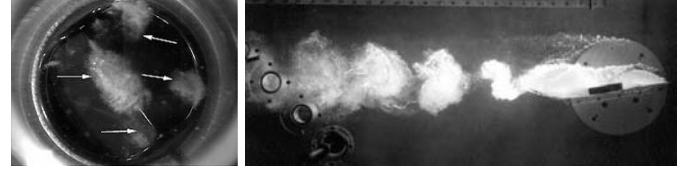


Figure 19. Examples of bubble clouds. Left: clouds formed downstream of an artificial heart valve closure (Rambod *et al.* [69]). Right: clouds formed in the wake of an oscillating hydrofoil

The highly destructive consequences of cloud cavitation have been known for a long time and have been documented, for example, by Knapp [56], Bark and van Berlekom [57] and Soyama *et al.* [58]. The generation of these cavitation clouds may occur naturally as a result of the shedding of bubble-filled vortices, or it may be the response to a periodic disturbance imposed on the flow. Common examples of imposed fluctuations are the interaction between rotor and stator blades in a pump or turbine, the interaction between a ship's propeller and the non-uniform wake created by the hull and the periodic opening and closing of a heart valve. As a result numerous investigators (for example, Wade and Acosta [59], Bark and van Berlekom [57], Shen and Peterson [60,61], Bark [62], Franc and Michel [63], Hart *et al.* [64], Kubota *et al.* [65], Le *et al.* [66], de Lange *et al.* [67]) have studied the complicated flow patterns involved in the production and collapse of cloud cavitation, most of them examining a single hydrofoil. The radiated noise produced is characterized by pressure pulses of very short duration and large magnitude. These pressure pulses have been measured by Bark [62], Bark and van Berlekom [57], Le *et al.* [66], Shen and Peterson [60,61] and McKenney and Brennen [68].

Here we briefly review analyses of cloud cavitation in simplified geometries that allow us to anticipate the behavior of clouds of cavitation bubbles and the parameters that influence that behavior. These simpler geometries allow some anticipation of the role of cloud cavitation in more complicated flows such as those in cavitating pumps.

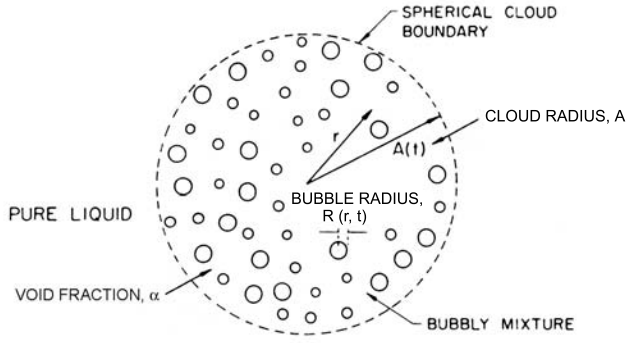


Figure 20. Schematic of a spherical cloud of cavitation bubbles [71,72].

Though the first analysis that indicated how bubbles might behave collectively was conducted by van Wijngaarden [70] on a plane layer of bubbles next to a wall, it is more convenient to focus attention on a finite spherical cloud surrounded by pure liquid and to briefly review the dynamics and acoustics of such a cloud. We begin with the simplified case shown in figure 20 in which all the bubbles in the cloud have the same equilibrium size, R_0 , and are uniformly distributed within the cloud. Thus the population as represented by the initial equilibrium void fraction, α_0 , is uniform within the cloud. Radial position within the cloud is denoted by r and the initial radius of the cloud by A_0 .

d'Agostino and Brennen [71,72] showed that a linearized dynamics analysis of such a cloud reveals that it has its own, infinite set of natural frequencies denoted by ω_n and given by

$$\omega_n = \omega_N \left[1 + \frac{4}{3\pi^2(2n-1)^2} \frac{A_0^2}{R_0^2} \frac{\alpha_0}{1-\alpha_0} \right]^{-\frac{1}{2}}$$

for $n = 1, 2, 3, \dots$ and where ω_N is the previously quoted natural frequency of an individual bubble oscillating alone in an infinite liquid. The above is an infinite series of frequencies of which ω_1 is the lowest. The higher frequencies approach ω_N as n tends to infinity.

As expected these natural frequencies correspond to modes with more and more nodes as n increases (see Brennen [9]). Note that the lowest natural frequency, ω_1 , is given by

$$\omega_1 = \omega_N \left[1 + \frac{4}{3\pi^2} \frac{A_0^2}{R_0^2} \frac{\alpha_0}{1-\alpha_0} \right]^{-\frac{1}{2}}$$

Note also that this can be much smaller than ω_N if the initial void fraction, α_0 , is much larger than the square of the ratio of bubble size to cloud size, $\alpha_0 \gg R_0^2/A_0^2$. If the reverse is the case ($\alpha_0 \ll R_0^2/A_0^2$) all the natural frequencies of the cloud are contained in a small range just below ω_N . This defines a special parameter, $\beta = \alpha_0 A_0^2/R_0^2$, that governs the cloud interaction effects and that is termed the "Cloud Interaction Parameter".

If $\beta \ll 1$ there is relatively little bubble interaction effect and all the bubbles oscillate at close to the frequency, ω_N , as if each were surrounded by nothing but liquid. On the other hand when $\beta > 1$ the cloud has natural frequencies much less than ω_N and there are strong interaction effects between the bubbles in the cloud.

Note that in various applications the magnitude of β could take a wide range of values from much less than unity to much greater than unity. It will be small in small clouds with a few large bubbles and a low void fraction but could be large in large clouds of small bubbles with higher void fraction.

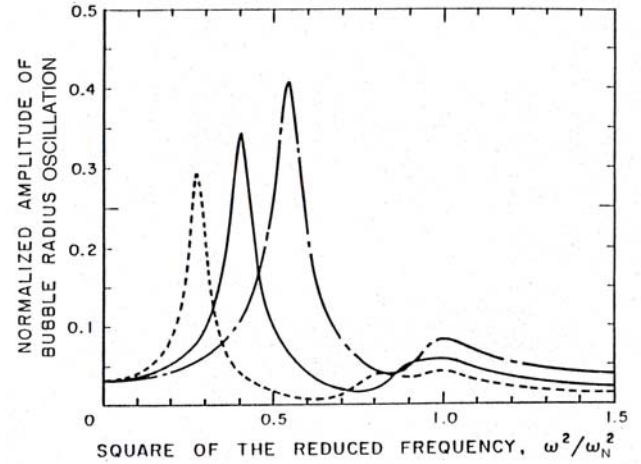


Figure 21. The amplitude of the bubble radius oscillation at the cloud surface as a function of frequency for damped oscillations at three values of $\beta = 0.8$ (solid line), $\beta = 0.4$ (dot-dash line), and $\beta = 1.65$ (dashed line). From d'Agostino and Brennen [72].

d'Agostino and Brennen [71,72] examined the forced linearized response of a cloud to oscillations in the pressure in the liquid far from the bubble. When a reasonable estimate of the damping is included, the attenuation of the higher frequencies is much greater so the dominant peak in the response occurs at the lowest natural frequency of the cloud, namely ω_1 . The response at the bubble natural frequency, ω_N , becomes much less significant. This conclusion and the effect of varying the cloud interaction parameter, β , is shown in figure 21, where the amplitude of bubble radius oscillation at the cloud surface is presented as a function of frequency. Note that increasing β causes a reduction in both the amplitude and frequency of the dominant response at the lowest natural frequency of the cloud.

The above results are all from linear analyses and we conclude our discussion of cloud effects by describing calculations of the large amplitude non-linear analyses. If a spherical cloud is subjected to an episode of sufficiently low pressure it will cavitate, in other words the bubbles will grow explosively to many times their original size. Subsequently, if the pressure far from the

cloud increases again (as, for example, when the cloud is convected out of the region of low pressure) the bubbles will collapse violently. We previously described the response of a single bubble to such a pressure episode; the response of a cloud of bubbles is more complex.

A valuable perspective on the subject was that introduced by Morch [73,74,75] and Hanson, Kedrinskii and Morch [76]. They suggested that the collapse of a cloud of bubbles involves the formation and inward propagation of a shock wave and that the geometric focusing of this shock at the center of cloud creates the enhancement of the noise and damage potential associated with cloud collapse. Wang and Brennen [77,78] and Reisman et al. [79] employed the use of continuity and momentum equations coupled to the Rayleigh-Plesset equation in order to model the two-phase flow within the cloud. Here we briefly review their numerical calculations that detailed the dynamics of a spherical cloud of cavitating bubbles..

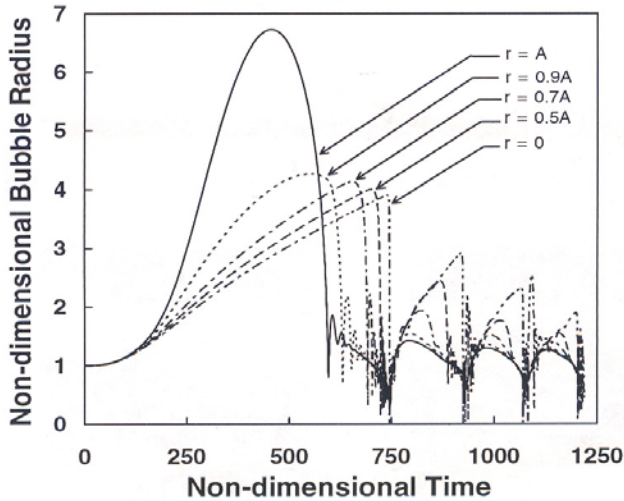


Figure 22. Typical time history of the bubble size at six different Lagrangian positions in a spherical cloud in response to an episode of reduced pressure in the surrounding liquid (between $t=0$ and $t=250$). This figure is for the parameter β much greater than unity [77,78].

It transpires that the response of a cloud to an episode of reduced pressure in the surrounding liquid is quite different depending on the magnitude of β . When β is much greater than unity the typical cloud response to an episode of reduced pressure is shown in figure 22 (upper). Note that the bubbles on the surface of the cloud grow more rapidly than those in the interior which are effectively shielded from the reduced pressure in the surrounding liquid. More importantly the bubbles on the surface collapse first and a collapse front propagates inward from the cloud surface developing into a substantial shock wave. Due to geometric focusing this shock wave strengthens as the shock proceeds inwards

and creates a very large pressure pulse when it reached the center of the cloud.

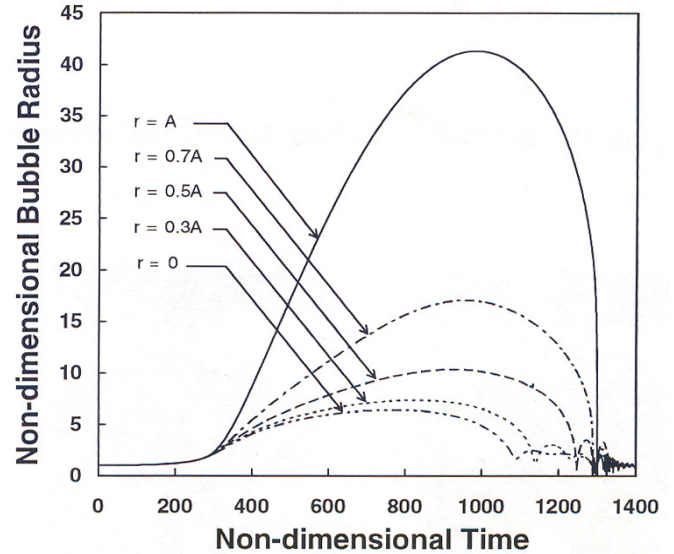


Figure 23. As Figure 22 but for β order unity or less [77,78].

On the other hand when β is small, the response of the cloud is quite different as shown in figure 23. Then the bubbles at the center of the cloud collapse first, resulting in an outgoing collapse front that weakens geometrically resulting in a quite different and much more benign dynamic.

While real bubble clouds are often far from spherical the potential for similar shielding and focussing effects still clearly exist.

13. CONCLUDING COMMENTS

This condensed review is an attempt to summarize at least some of the fundamental analyses and observations pertaining to cavitating flow. Of necessity we have omitted a huge literature of experimental observations and we have not covered important new results using modern computational techniques as well as research methodologies that use parallel experimental observations and computations of these high-speed events. Many challenges remain; for example the desire to accurately compute these complex, high-speed multiphase flows, an objective made doubly difficult by the multiple time and space scales of the flows.

ACKNOWLEDGEMENTS

My sincerest thanks to all graduate students and post-doctoral fellows who contributed to the results described herein. I am also appreciative of the support from the Office of Naval Research who sponsored a good fraction of the research described.

REFERENCES

- [1] Brennen, C.E. 2005. Fundamentals of multiphase flow. Cambridge University Press.
- [2] Peterson, F.B., Danel, F., Keller, A.P., and Lecoffre, Y. 1975. Comparative measurements of bubble and particulate spectra by three optical methods. Proc. 14th Int. Towing Tank Conf.
- [3] Gates, E.M. and Bacon, J. 1978. Determination of cavitation nuclei distribution by holography. J. Ship Res., 22, No. 1, 29-31.
- [4] Katz, J. 1978. Determination of solid nuclei and bubble distributions in water by holography. Calif. Inst. of Tech., Eng. and Appl. Sci. Div. Rep. No. 183-3.
- [5] O'Hern, T.J., Katz, J., and Acosta, A.J. 1985. Holographic measurements of cavitation nuclei in the sea. Proc. ASME Cavitation and Multiphase Flow Forum, 39-42.
- [6] Knapp, R.T., Daily, J.W., and Hammitt, F.G. 1970. Cavitation. McGraw-Hill, New York.
- [7] Acosta, A.J. and Parkin, B.R. 1975. Cavitation inception--a selective review. J. Ship Res., 19, 193-205.
- [8] Arakeri, V.H. 1979. Cavitation inception. Proc. Indian Acad. Sci., C2, Part 2, 149-177.
- [9] Brennen, C.E. 1995. Cavitation and bubble dynamics. Oxford University Press.
- [10] Knapp, R.T., Daily, J.W., and Hammitt, F.G. 1970. Cavitation. McGraw-Hill, New York.
- [11] Young, F.R. 1989. Cavitation. McGraw-Hill Book Company.
- [12] Herring, C. 1941. The theory of the pulsations of the gas bubbles produced by an underwater explosion. US Nat. Defence Res. Comm. Report.
- [13] Gilmore, F.R. 1952. The collapse and growth of a spherical bubble in a viscous compressible liquid. Calif. Inst. of Tech. Hydrodynamics Lab. Rep. No. 26-4.
- [12] Prosperetti, A. and Lezzi, A. 1986. Bubble dynamics in a compressible liquid. Part 1. First-order theory.
- [13] Keller, J.B. and Kolodner, I.I. 1956. Damping of underwater explosion bubble oscillations. J. Appl. Phys., 27, 1152-1161.
- [14] Hickling, R. and Plesset, M.S. 1964. Collapse and rebound of a spherical bubble in water. Phys. Fluids, 7, 7-14.
- [15] Ivany, R.D. and Hammitt, F.G. 1965. Cavitation bubble collapse in viscous, compressible liquids - numerical analysis. ASME J. Basic Eng., 87, 977-985.
- [16] Tomita, Y. and Shima, A. 1977. On the behaviour of a spherical bubble and the impulse pressure in a viscous compressible liquid. Bull. JSME, 20, 1453-1460.
- [17] Fujikawa, S. and Akamatsu, T. 1980. Effects of the non-equilibrium condensation of vapour on the pressure wave produced by the collapse of a bubble in a liquid. J. Fluid Mech., 97, 481-512.
- [18] Birkhoff, G. 1954. Note on Taylor instability. Quart. Appl. Math., 12, 306-309.
- [19] Plesset, M.S. and Mitchell, T.P. 1956. On the stability of the spherical shape of a vapor cavity in a liquid. Quart. Appl. Math., 13, No. 4, 419-430.
- [20] Naude, C.F. and Ellis, A.T. 1961. On the mechanism of cavitation damage by non-hemispherical cavities in contact with a solid boundary. ASME. J. Basic Eng., 83, 648-656.
- [21] Benjamin, T.B. and Ellis, A.T. 1966. The collapse of cavitation bubbles and the pressures thereby produced against solid boundaries. Phil. Trans. Roy. Soc., London, Ser. A, 260, 221-240.
- [22] Tomita, Y. and Shima, A. 1990. High-speed photographic observations of laser-induced cavitation bubbles in water. Acustica, 71, No. 3, 161-171.
- [23] Lauterborn, W. and Bolle, H. 1975. Experimental investigations of cavitation bubble collapse in the neighborhood of a solid boundary. J. Fluid Mech., 72, 391-399.
- [24] Plesset, M.S. and Chapman, R.B. 1971. Collapse of an initially spherical vapor cavity in the neighborhood of a solid boundary. J. Fluid Mech., 47, 283-290.
- [25] Plesset, M.S. and Prosperetti, A. 1977. Bubble dynamics and cavitation. Ann.Rev. Fluid Mech., 9, 145-185.
- [26] Chahine, G.L. (1977). Interaction between an oscillating bubble and a free surface. ASME J. Fluids Eng., 99, 709-716.
- [27] Gibson, D.C. and Blake, J.R. (1982). The growth and collapse of bubbles near deformable surfaces. Appl. Sci. Res., 38, 215-224.
- [28] Chahine, G.L. and Duraiswami, R. (1992). Dynamical interactions in a multibubble cloud. ASME J. Fluids Eng., 114, 680-686.
- [29] Frost, D. and Sturtevant, B. 1986. Effects of ambient pressure on the instability of a liquid boiling explosively at the superheat limit. ASME J. Heat Transfer, 108, 418--424.
- [30] Brennen, C.E. (2002). Fission of collapsing cavitation bubbles. J. Fluid Mech., 472, 153-166.
- [31] ASTM. 1967. Erosion by cavitation or impingement. Amer. Soc. for Testing and Materials, ASTM STP408
- [32] Thiruvengadam, A. 1967. The concept of erosion strength. In Erosion by cavitation or impingement. Am. Soc. Testing Mats. STP 408, 22-35.
- [33] Thiruvengadam, A. 1974. Handbook of cavitation erosion. Tech. Rep. 7301-1, Hydronautics, Inc., Laurel, Md.
- [34] Shima, A., Takayama, K., Tomita, Y., and Ohsawa, N. 1983. Mechanism of impact pressure generation from spark-generated bubble collapse near a wall. AIAA J., 21, 55-59.
- [35] Kimoto, H. 1987. An experimental evaluation of the effects of a water microjet and a shock wave by a local pressure sensor. Int. ASME Symp. on Cavitation Res. Facilities and Techniques, FED 57, 217-224.
- [36] Knapp, R.T. and Hollander, A. 1948. Laboratory investigations of the mechanism of cavitation. Trans. ASME, 70, 419-435.
- [37] Plesset, M.S. 1949. The dynamics of cavitation bubbles. ASME J. Appl. Mech., 16, 228-231.
- [38] Parkin, B.R. 1952. Scale effects in cavitating flow. Ph.D. Thesis, Calif. Inst. Of Tech.

- [39] Ceccio, S.L. and Brennen, C.E. 1991. Observations of the dynamics and acoustics of travelling bubble cavitation. *J. Fluid Mech.*, 233, 633-660.
- [40] Kuhn de Chizelle, Y., Ceccio, S.L., Brennen, C.E., and Gowing, S. 1992a. Scaling experiments on the dynamics and acoustics of travelling bubble cavitation. *Proc. 3rd I. Mech. E. Int. Conf. on Cavitation*, Cambridge, England, 165-170.
- [41] Kuhn de Chizelle, Y., Ceccio, S.L., Brennen, C.E., and Shen, Y. 1992b. Cavitation scaling experiments with headforms: bubble acoustics. *Proc. 19th ONR Symp. on Naval Hydrodynamics*, 72-84.
- [42] Kumar, S. and Brennen, C.E. 1993. A study of pressure pulses generated by travelling bubble cavitation. *J. Fluid Mech.*, 255, 541-564.
- [43] Dowling, A.P. and Ffowcs Williams, J.E. 1983. *Sound and sources of sound*. Ellis Horwood Ltd. and John Wiley and Sons.
- [44] Blake, W.K. 1986b. *Mechanics of flow-induced sound and vibration*. Academic Press.
- [45] Lush, P.A. and Angell, B. 1984. Correlation of cavitation erosion and sound pressure level. *ASME. J. Fluids Eng.*, 106, 347-351.
- [46] Rayleigh, Lord (Strutt, J.W.). 1917. On the pressure developed in a liquid during the collapse of a spherical cavity. *Phil. Mag.*, 34, 94-98.
- [47] Mellen, R.H. 1954. Ultrasonic spectrum of cavitation noise in water. *J. Acoust. Soc. Am.*, 26, 356-360.
- [48] Fitzpatrick, H.M. and Strasberg, M. 1956. Hydrodynamic sources of sound. *Proc. First ONR Symp. on Naval Hydrodynamics*, 241-280.
- [49] Martin, C.S., Medlarz, H., Wiggert, D.C., and Brennen, C. 1981. Cavitation inception in spool valves. *ASME. J. Fluids Eng.*, 103, 564-576.
- [50] Jorgensen, D.W. 1961. Noise from cavitating submerged jets. *J. Acoust. Soc. Am.*, 33, 1334-1338.
- [51] Blake, W.K. and Sevik, M.M. 1982. Recent developments in cavitation noise research. *Proc. ASME Int. Symp. on Cavitation Noise*, 1-10.
- [52] Esipov, I.B. and Naugol'nykh, K.A. 1973. Collapse of a bubble in a compressible liquid. *Akust. Zh.*, 19, 285-288.
- [53] Blake, W.K., Wolpert, M.J. and Geib, F.E. 1977. Cavitation noise and inception as influenced by boundary-layer development on a hydrofoil. *J. Fluid Mech.*, 80, 617-640.
- [54] Arakeri, V.H. and Shangumanathan, V. 1985. On the evidence for the effect of bubble interference on cavitation noise. *J. Fluid Mech.*, 159, 131-150.
- [55] Franklin, R.E. and McMillan, J. 1984. Noise generation in cavitating flows, the submerged jet. *ASME J. Fluids Eng.*, 106, 336-341.
- [56] Knapp, R.T. 1955. Recent investigations of the mechanics of cavitation and cavitation damage. *Trans. ASME*, 77, 1045-1054.
- [57] Bark, G., and Berlekom, W.B. 1978. Experimental Investigations of Cavitation Noise. *Proc. 12th ONR Symp. on Naval Hydrodynamics*, 470-493.
- [58] Soyama, H., Kato, H., and Oba, R. 1992. Cavitation Observations of Severely Erosive Vortex Cavitation Arising in a Centrifugal Pump. *Proc. Third I.Mech.E. Int. Conf. on Cavitation*, 103-110.
- [59] Wade, R.B. and Acosta, A.J. 1966. Experimental Observations on the Flow Past a Plano-Convex Hydrofoil. *ASME J. Basic Eng.*, 88, 273-283.
- [60] Shen, Y., and Peterson, F.B. 1978. Unsteady Cavitation on an Oscillating Hydrofoil. *Proc. 12th ONR Symposium on Naval Hydrodynamics*, 362-384.
- [61] Shen, Y., and Peterson, F.B. 1980. The Influence of Hydrofoil Oscillation on Boundary Layer Transition and Cavitation Noise. *Proc. 13th ONR Symposium on Naval Hydrodynamics*, 221-241.
- [62] Bark, G. 1985. Developments of Distortions in Sheet Cavitation on Hydrofoils. *Proc. ASME Int. Symp. on Jets and Cavities*, 470-493.
- [63] Franc, J.P., and Michel, J.M. 1988. Unsteady Attached Cavitation on an Oscillating Hydrofoil. *J. Fluid Mech.*, 193, 171-189.
- [64] Hart, D.P., Brennen, C.E. and Acosta, A.J. 1990. Observations of cavitation on a three dimensional oscillating hydrofoil. *ASME Cavitation and Multiphase Flow Forum*, FED-98, 49-52.
- [65] Kubota, A., Kato, H., Yamaguchi, H. and Maeda, M. 1989. Unsteady structure measurement of cloud cavitation on a foil section using conditional sampling. *ASME J. Fluids Eng.*, 111, 204-210.
- [66] Le, Q., Franc, J. M. and Michel, J. M. 1993. Partial cavities: global behaviour and mean pressure distribution. *ASME J. Fluids Eng.*, 115, 243-248.
- [67] de Lange, D.F., de Bruin, G.J. and van Wijngaarden, L. 1994. On the mechanism of cloud cavitation - experiment and modeling. *Proc. 2nd Int. Symp. on Cavitation*, Tokyo, 45-50.
- [68] McKenney, E.A. and Brennen, C.E. 1994. On the dynamics and acoustics of cloud cavitation on an oscillating hydrofoil. *Proc. ASME Symp. on Cavitation and Gas-Liquid Flows in Fluid Machinery and Devices*, FED-190, 195-202.
- [69] Rambod, E., Beizaie, M., Shusser, M., Milo, S. and Gharib, M. 1999. A physical model describing the mechanism for formation of gas microbubbles in patients with mitral mechanical heart valves. *Ann. Biomed. Eng.*, 27, 774-792.
- [70] van Wijngaarden, L. 1964. On the collective collapse of a large number of gas bubbles in water. *Proc. 11th Int. Conf. Appl. Mech.*, Springer-Verlag, Berlin, 854-861.
- [71] d'Agostino, L. and Brennen, C.E. 1983. On the acoustical dynamics of bubble clouds. *ASME Cavitation and Multiphase Flow Forum*, 72-75.
- [72] d'Agostino, L. and Brennen, C.E. 1989. Linearized dynamics of spherical bubble clouds. *J. Fluid Mech.*, 199, 155-176.
- [73] Morch, K.A. 1980. On the collapse of cavity cluster in flow cavitation. *Proc. First Int. Conf. on Cavitation and*

Inhomogenities in Underwater Acoustics, Springer Series in Electrophysics, 4, 95--100.

[74] Morch, K.A. 1981. Cavity cluster dynamics and cavitation erosion. Proc. ASME Cavitation and Polyphase Flow Forum, 1--10.

[75] Morch, K.A. 1982. Energy considerations on the collapse of cavity cluster. Appl. Sci. Res., 38, 313.

[76] Hanson, I., Kedrinskii, V.K. and Morch, K.A. 1981. On the dynamics of cavity clusters. J. Appl. Phys., 15, 1725--1734.

[77] Wang, Y.-C. and Brennen, C.E. 1995a. The noise generated by the collapse of a cloud of cavitation bubbles. Proc. ASME/JSME Symp. on Cavitation and Gas-Liquid Flow in Fluid Machinery and Devices, FED-226, 17--29.

[78] Wang, Y.-C. and Brennen, C.E. 1995b. Shock wave and noise in the collapse of a cloud of cavitation bubbles. Proc. 20th Int. Symp. on Shock Waves, 1213--1218.

[79] Reisman, G.E., Wang, Y.-C. and Brennen, C.E. 1998. Observations of shock waves in cloud cavitation. J. Fluid Mech., 355, 255--283.

Cavitation Erosion: From Pitting to Mass Loss

Jean-Pierre FRANC
Grenoble University
LEGI, BP 53, 38041 Grenoble Cedex 9, France
Jean-Pierre.Franc@legi.grenoble-inp.fr

ABSTRACT

This paper describes the chain of phenomena leading to cavitation erosion. It aims at suggesting a method of prediction of cavitation erosion based on a physical analysis of the various steps of the damage process. The approach is based on the concept of impact load generated by the collapse of a cavitation bubble and the associated “cavitation intensity” defined as the statistical distribution of impact loads. It is guessed that an accurate determination of the so-called cavitation intensity together with a detailed analysis of the material response to repeated impact loads should make it possible in the future to predict quantitatively cavitation erosion damage from an essentially numerical approach.

1. INTRODUCTION

The present contribution follows the oral presentation given at the WIMRC 3rd International Cavitation Forum 2011. It gives a summary of the main issues and conclusions and directly refers to the slides given at the end of the paper.

The prediction of cavitation erosion damage by numerical simulation is a big challenge. Several difficulties can be identified.

First of all, cavitation erosion is caused by the collapse of small bubbles or vortices whose characteristic size is generally much smaller than the size of the large scale cavitating structures such as e.g. the cavity which develops at the leading edge of a blade. The change from a macro- to a micro-scale is a difficult issue.

Secondly, the collapse of a cloud of micro structures is difficult to model in detail. The impact loads generated on a neighboring wall are of short duration in comparison to the characteristic times of the large scale structures. Hence, in addition to a change of length scale, a change of time scale is needed to accurately predict high-speed cavitation impacts.

Moreover, the response of the material to repeated impacts of small size, high amplitude and small characteristic time is a complex issue. Parameters such as strain rate, microstructure, modes of plastic deformation, modes of failure have to be included in the analysis, and this is still a big challenge.

Four different steps are considered here in the erosion process (slide 2):

1. The large scale vapor structures break up into small bubbles.

2. Each bubble, when collapsing, generates a localized, high intensity, short duration pressure pulse on the neighboring wall.
3. Each impact load, if strong enough, creates a pit on the surface.
4. Repeated impulsive loading of the material generates pitting, failure and finally mass loss.

Each step is rapidly discussed in the following sections.

2. STEP 1: PRODUCTION OF SMALL SCALE VAPOR STRUCTURES

The production of large scale vapor structures is generally well predicted by conventional CFD cavitation models (slide 3). As an example, the mechanism of cloud cavitation has been analyzed by several investigators and it is generally considered that the shedding frequency follows a Strouhal scaling law. However, as far as cavitation erosion is concerned, it is necessary to have a detailed knowledge of the bubble content (density, size, bubble-to-wall distance...) in such a cloud since each bubble is expected to produce its own elementary damage when collapsing (slide 4). Attempts are presently being made to model the production of small scale vapor structures and the impact loads due to their collapse (slide 5, see for instance [1]).

3. STEP 2: IMPACT LOADS DUE TO CAVITATION BUBBLE COLLAPSES

Whatever maybe the physical mechanism (re-entrant jet or shock wave, slide 7), the collapse of a bubble induces an impact load on the wall of short duration ($\sim \mu\text{s}$), high intensity ($\sim \text{GPa}$) and on a limited surface area (a few tens of μm typically, slide 8). We suggest to define the intensity of a cavitating flow by the rate of impact loads per unit surface area (slide 9). The cavitation intensity (CI) depends upon the location on the wall since the erosion is obviously not uniform everywhere. Each impact load should be characterized by several parameters. Two major parameters are the amplitude and the characteristic size of the impacted area. Additional parameters such as the time evolution of the amplitude (which controls the strain rate) or the radial distribution of the impact pressure could also be of importance in the resulting damage.

The measurement of impact loads is a difficult task. A few results are presented here of measurements conducted in the erosion facility of the Grenoble University (slides 10-12). Using a conventional pressure sensor flush mounted in the region of

maximum cavitation erosion (slide 13), it was possible to measure pressure pulse height spectra (PPHS) under various operating conditions (slide 14-16). It was observed that the peak rate follows an exponential law with the amplitude (slide 17). As shown in slide 18, the different spectra obtained at different velocities could be reduced to a unique non-dimensional spectrum using appropriate scaling laws on pulse rate and pulse amplitude.

Several investigators have introduced a global estimate of the cavitation intensity based on an acoustic approach originally proposed by Hammitt [2]. This estimate consists in cumulating the amplitudes squared for all detected pressure pulses as shown by the equation of slide 19. Several investigators (see for instance [3],[4], slides 20-21) found a linear correlation between mass loss and the so-defined cavitation intensity. Okada et al. [4] have even shown that this relationship depends upon the material but is independent of test conditions and type of apparatus (Venturi or vibratory system).

4. STEP 3: PITTING

Typical pitting test results obtained at Grenoble are presented in slides 23 to 34. Pitting tests were proposed many years ago by Knapp [5] in order to characterize the cavitation intensity. They consist in conducting short duration tests on mirror polished samples and analyzing the resulting pits in terms of density, diameter, depth, volume (slides 23-24). The analysis generally requires defining a cut-off depth whose influence on the results is not yet quite clear (slide 25).

The cumulative pitting rate generally follows an exponential law with pit size. It is shown in slide 26 that this law depends upon two parameters which are identified as the coverage time (slide 27) and a characteristic pit size (slide 28). The coverage time is a fundamental parameter in cavitation erosion not only for the incubation period but also for the most advanced stages of erosion when material is removed as shown in slide 45. It is the time required for the material surface to be fully covered, one time only, by cavitation impacts. As for the second parameter, the characteristic pit size, it represents the size of the pits which contribute predominantly to the coverage mechanism (slide 28). It is shown on slide 29 that simple scaling laws for pitting rate can be derived to account for both a change of flow velocity and a change of material.

The effect of material properties on pitting rate is discussed on slides 32 to 34 on the basis of pitting tests conducted on three different materials. It is generally assumed that a plastic deformation (pit) is formed if the amplitude of the pressure pulse exceeds a threshold value depending upon the material. Its elastic limit is often considered as a relevant threshold. Results presented in slides 32-33 show that the conventional elastic limit determined from standard tensile tests is not fully appropriate. It is conjectured that tests under compressive loading would be more representative for cavitation erosion studies. Moreover, the analysis should include strain rate which is known to be quite high in cavitation erosion and to influence significantly the mechanical properties of several materials (slide 34).

The plastic deformation which results from the collapse of a cavitation bubble can be considered as the signature of the collapse. In particular, it is believed that the impact load generated by the collapsing bubble can be inferred from the

resulting pit shape. Such an approach considers the material as a kind of sensor. A possible technique to estimate the impact load is to use the similarity between an indent generated after applying a given load on a spherical indenter by a conventional nano-indentation test and the pit which results from the collapse of a cavitation bubble (cf. slide 35). Loading conditions during cavitation can then be deduced from joint pitting and nano-indentation tests. This approach is presently investigated at EPFL [6, 7]. Computations of the response of the material to an impact load using a finite element code could also be helpful to determine, by an inverse technique, the amplitude of the impact load required to generate a pit of given shape.

5. STEP 4: MASS LOSS

The repeated impulsive loading of the material finally results in failure and mass loss. Long duration tests are generally needed to go through the incubation period and reach the most advanced stages of erosion where mass loss actually occurs. Typical mass loss curves are presented in slides 42-43 together with visualizations of the eroded surface (slides 40-41).

A model of response of a ductile material to the repeated impulsive loading is presented in slide 44. The material behavior is represented on its stress-strain curve. During the incubation period, the material is progressively hardened by successive impacts. Plastic deformation occurs in the most superficial layers and results in an increased strain. A failure criterion should be used to define the end of the incubation period and the subsequent onset of mass loss. In the present state of development of the model, failure is assumed to occur when the maximum strain in the material exceeds a threshold value, considered as the ultimate strain of the material. The computation of mass loss is based on the assumption that the material cannot sustain a strain greater than its ultimate strain. All the material layers where the local strain exceeds this threshold are supposed to be removed by cavitation erosion. This gives a way to compute the erosion rate. Further details on this model are available in references [8, 9].

In the simplified case of cavitation impacts of constant load, simple equations can be derived for the incubation time and the erosion rate [9]. These equations are presented in slide 45. The incubation time appears to be proportional to the coverage time defined previously. In addition, the erosion rate measured in terms of the mean depth of penetration rate (MDPR) appears to be inversely proportional to the incubation time and proportional to the thickness of the hardened layer. It is shown on slide 46 that this model is successful to explain the strong correlation between the erosion rate and the inverse of the incubation period which has been identified experimentally by several investigators (see for instance [10]).

6. CONCLUSION

Significant progress is being made with the analysis and modeling of the chain of phenomena leading to cavitation erosion damage. As discussed by Kato [11], the prediction of cavitation damage by a numerical approach is becoming more and more realistic. In our opinion, such an approach should be based on the concept of impact load generated on a wall by the collapse of a cavitation bubble and more generally on the spectrum of impact loads generated by the collapse of the small-

scale vapor structures forming a cavitation cloud. This concept is already widely used and CFD computations of cavitating flow are more and more promising in the field of prediction of impact loads. On the other hand, significant progress is being made in the analysis of the response of the material to repeated impact loads. By coupling a CFD computation of cavitation, oriented towards the prediction of impact loads, to a model of material response to such a specific loading, it should be possible to derive a method of prediction of cavitation erosion mostly based upon a numerical approach.

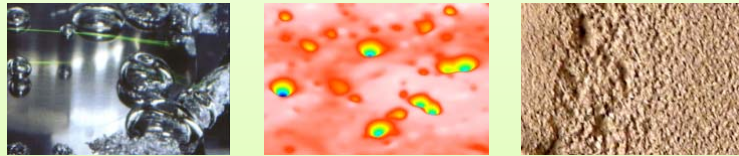
ACKNOWLEDGMENTS

The author is very grateful to Dr. Ki-Han Kim (Office of Naval Research) and Dr. Richard Vogelsong (Office of Naval Research Global) for supporting this research work. Many thanks to Dr. Ayat Karimi and Dr. Davide Carnelli (EPFL, Lausanne, Switzerland), Dr. Martin Donnelly (NSWCCD, USA), Dr. Farrel Martin (NRL, USA) and Dr. Georges L. Chahine (Dynaflow, Inc., USA) for their help in the research work. The author wish to thank also Dr. Steffen Schmidt (TU München, Germany) and Dr. Eric Johnsen (University of Michigan, USA) for providing videos presented during the conference.

REFERENCES

- Schmidt, S.J., I.H. Sezal, G.J. Schnerr, and M. Thalhamer, *Shock Waves as Driving Mechanism for Cavitation Erosion*, in *8th International Symposium on Experimental and Computational Aerothermodynamics of Internal Flows*. 2007: Lyon, France.
- Hammit, F.G., *Cavitation Erosion: The State of the Art and Predicting Capability*. Applied Mechanics Reviews, 1979. **32**(6): p. 665-675.
- Steller, J., A. Krella, J. Koronowicz, and W. Janicki, *Towards quantitative assessment of material resistance to cavitation erosion*. Wear, 2005. **258**(1-4): p. 604-613.
- Okada, T., Y. Iwai, S. Hattori, and N. Tanimura, *Relation between impact load and the damage produced by cavitation bubble collapse*. Wear, 1995. **184**(2): p. 231-239.
- Knapp, R.T., *Recent Investigations of the Mechanics of Cavitation and Cavitation Damage*. Transactions of the ASME, 1955(October): p. 1045-1054.
- Carnelli, D., A. Karimi, and J.P. Franc, *Evaluation of the Pressure of Cavitation Impacts Based on Pitting and Depth Sensing Nanoindentation Techniques*. Submitted for publication in Wear, 2011.
- Carnelli, D., A. Karimi, and J.P. Franc, *Application of Spherical Nanoindentation to Determine the Pressure of Cavitation Impacts from Pitting Tests*. Submitted for publication in Journal of Materials Research, 2011.
- Karimi, A. and W.R. Leo, *Phenomenological Model for Cavitation Rate Computation*. Materials Science & Engineering, 1987. **95**: p. 1-14.
- Franc, J.-P., *Incubation Time and Cavitation Erosion Rate of Work-Hardening Materials*. Journal of Fluids Engineering, 2009. **131**(2): p. 021303.
- Zhou, Y.K. and F.G. Hammit, *Cavitation erosion incubation period*. Wear, 1983. **86**(2): p. 299-313.
- Kato, H., A. Konno, M. Maeda, and H. Yamaguchi, *Possibility of Quantitative Prediction of Cavitation Erosion Without Model Test*. Journal of Fluids Engineering, 1996. **118**(3): p. 582-588.

Cavitation Erosion: From Pitting to Mass Loss



J.P. Franc
Grenoble University (LEGI), France

1/48

The chain of phenomena

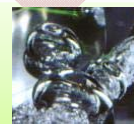
STEP 1

Large scale vapor structures break up into many small bubbles



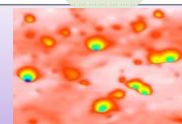
STEP 2

When collapsing (individually or collectively), each bubble generates a localized, high intensity, short duration impact load on the wall



STEP 3

Each impact load, if strong enough, creates a pit on the surface



STEP 4


Repeated impulsive loading of the material generates pitting, failure and mass loss



2/48

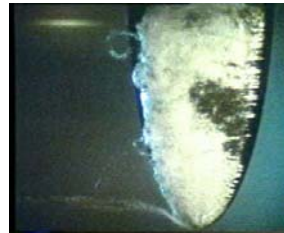
Bubble production (1/3)

- Large scale structures generally follow a Strouhal scaling law



$$\frac{f l}{V} \cong Cte$$

- ... but what about small scale structures ?

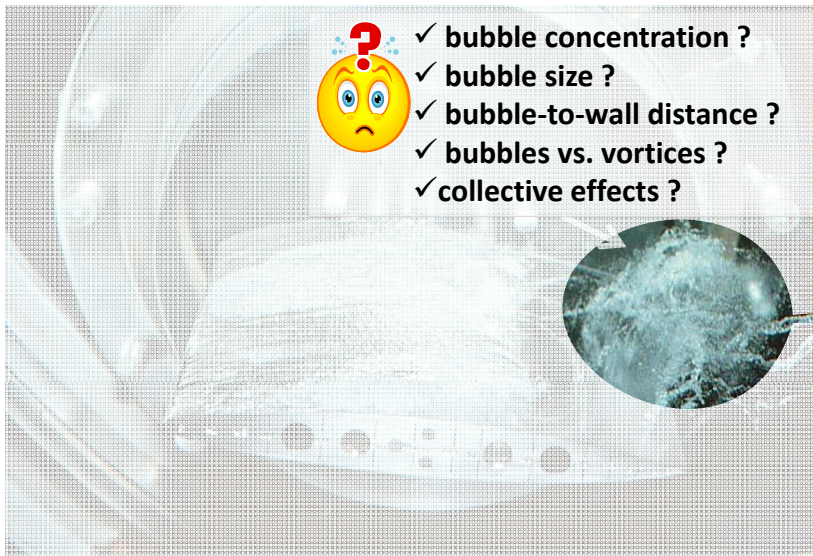


3/48

Bubble production (2/3)

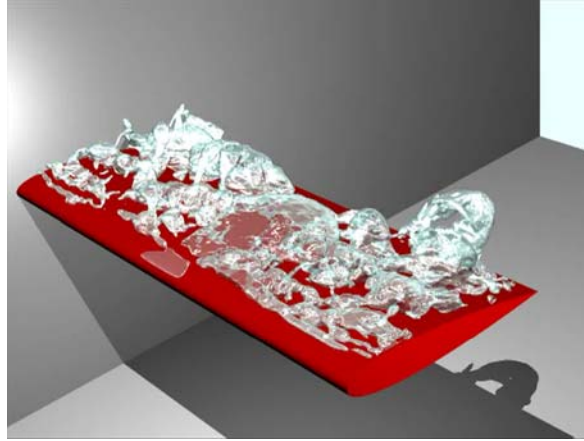


- ✓ bubble concentration ?
- ✓ bubble size ?
- ✓ bubble-to-wall distance ?
- ✓ bubbles vs. vortices ?
- ✓ collective effects ?



4/48

Bubble production (3/3)



Schmidt et al.
TU München

5/48

The chain of phenomena

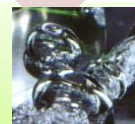
STEP 1

Large scale vapor structures break up into many small bubbles



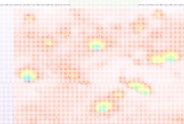
STEP 2

When collapsing (individually or collectively), each bubble generates a localized, high intensity, short duration impact load on the wall



STEP 3

Each impact load, if strong enough, creates a pit on the surface



STEP 4

Repeated impulsive loading of the material generates pitting, failure and mass loss



6/48

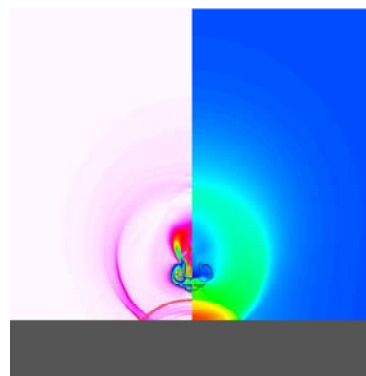
Mechanisms of impact load generation

Re-entrant jet



Chahine et al.
Dynaflow, Inc.

Shock wave

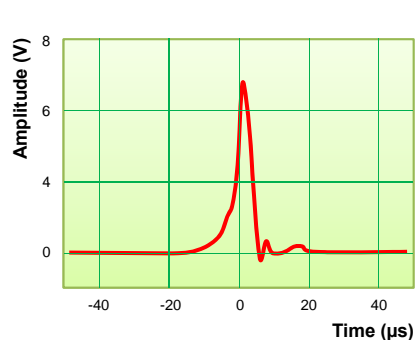


Johnsen
Univ. Michigan

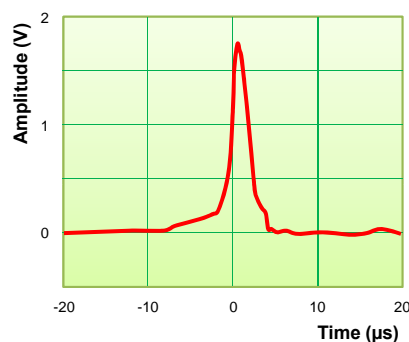
7/48

Cavitation impact loads

- Whatever maybe the mechanisms, the collapse of a bubble induces an impact load on the wall
- ✓ short duration ($\sim \mu\text{s}$)
- ✓ high intensity ($\sim \text{GPa}$)
- ✓ small surface area ($\sim \mu\text{m}$)



Soyama et al.
1998



Nguyen Trong
1993

8/48

Tentative definition of "Cavitation Intensity"

Cavitation Intensity = Rate of impact loads per unit surface area
a function of:

Location

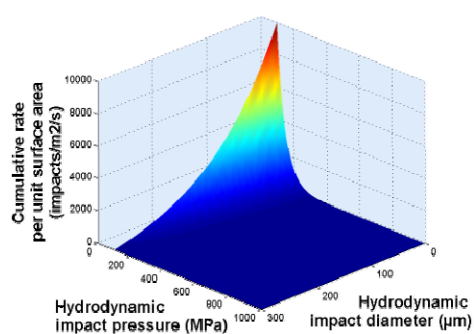
Load
(MPa or N)

Size
(μm)

Time
evolution
(strain rate...)

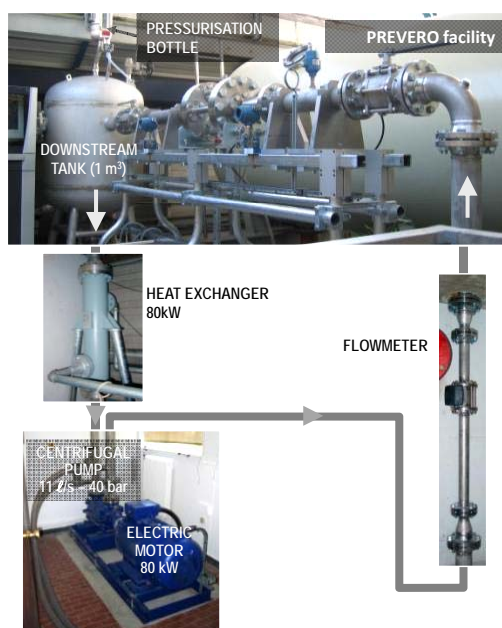
Radial
distribution

...

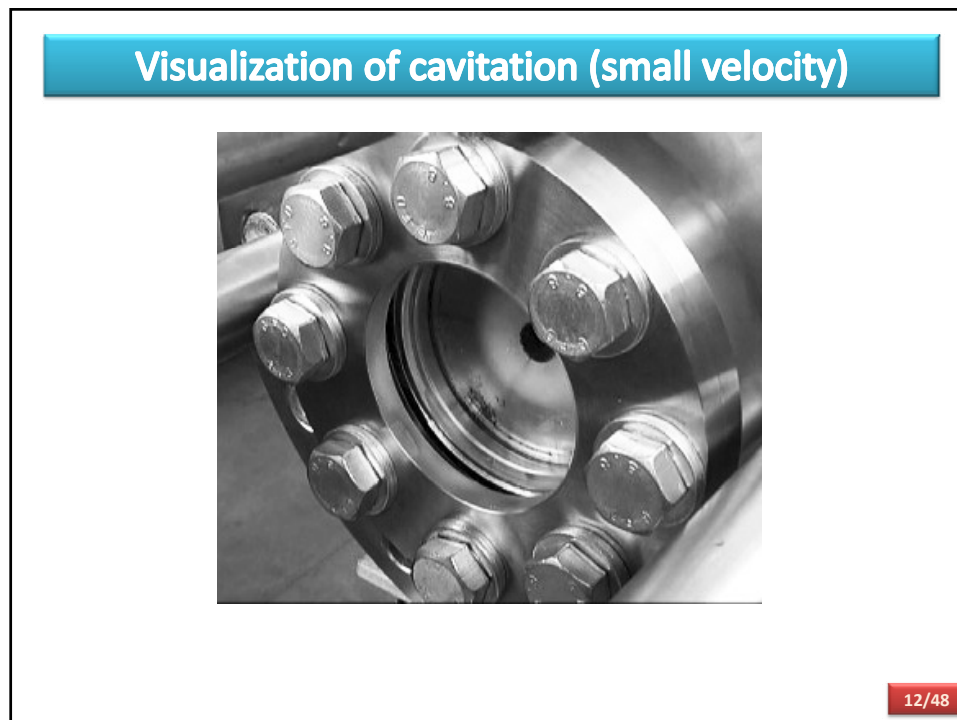
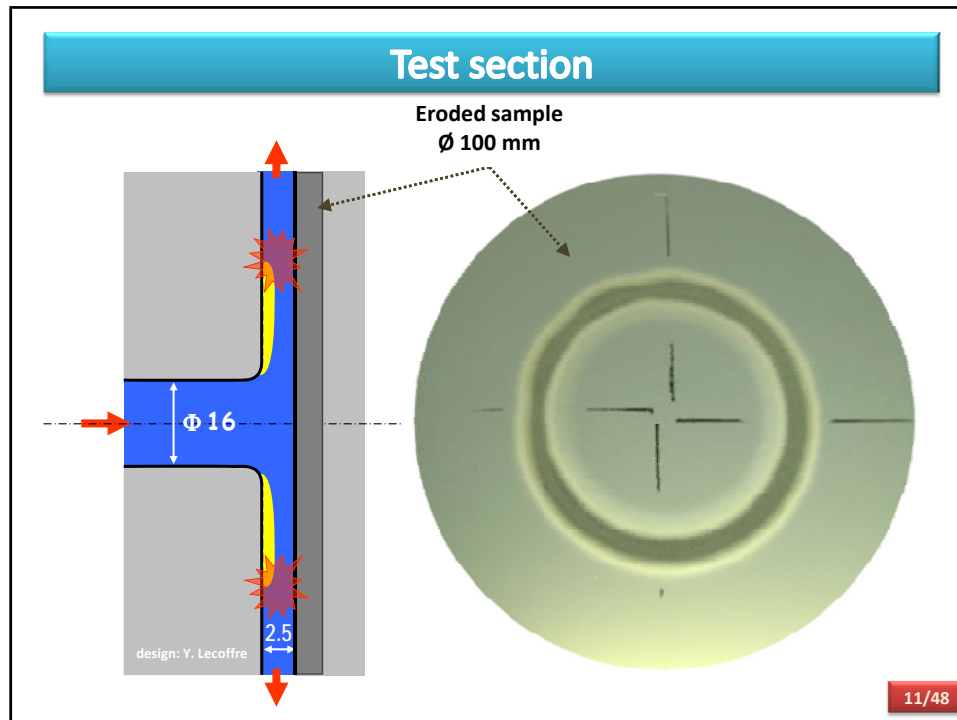


9/48

LEGI hydrodynamic cavitation erosion facility



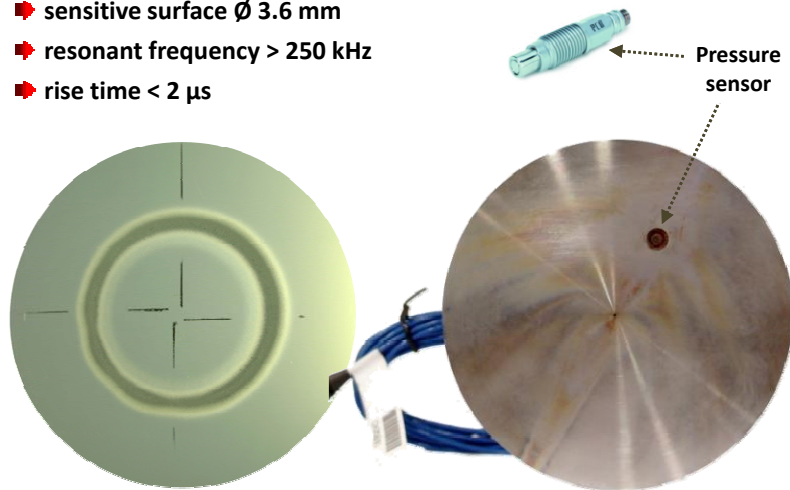
10/48



Impact load measurements

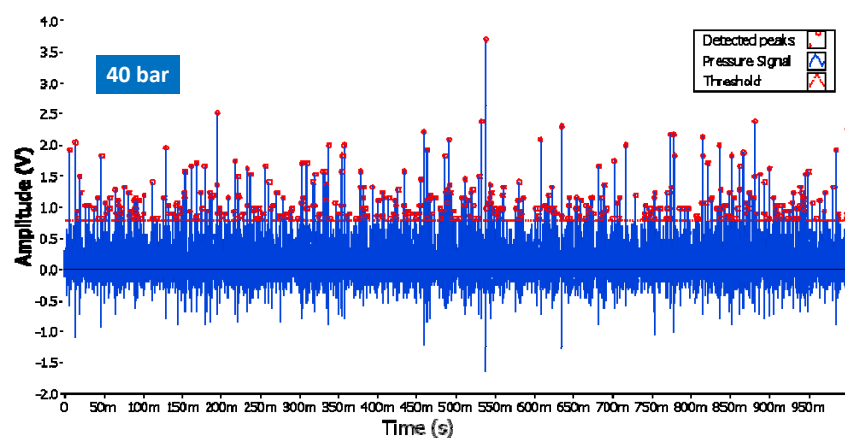
■ Commercial pressure sensor flush mounted

- sensitive surface \varnothing 3.6 mm
- resonant frequency > 250 kHz
- rise time < 2 μ s



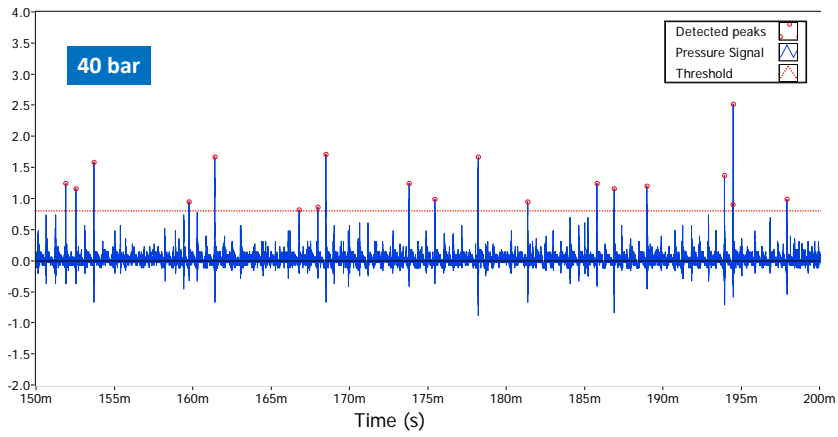
13/48

Typical signal



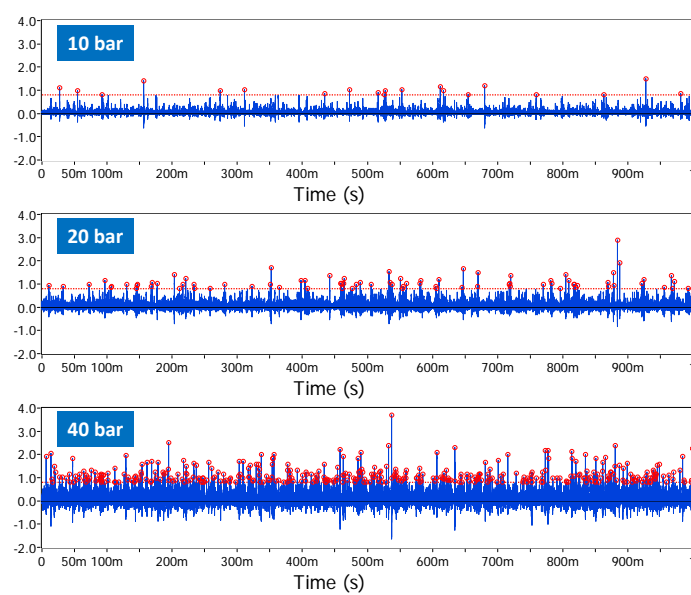
14/48

Typical signal



15/48

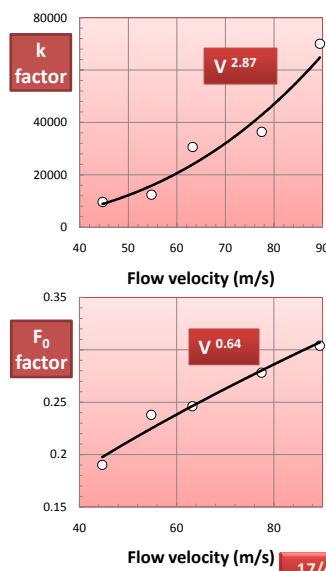
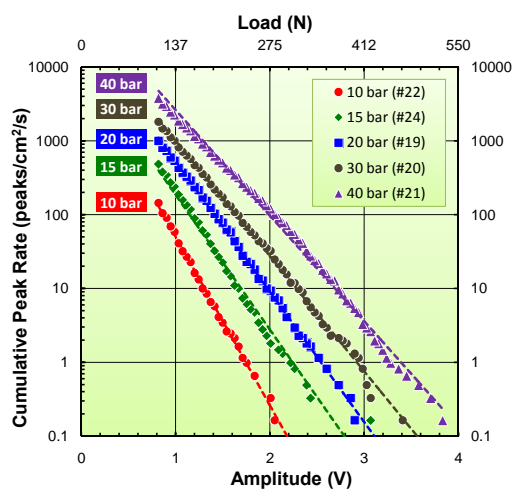
Influence of operating conditions



16/48

Pressure Peak Height Spectra (PPHS)

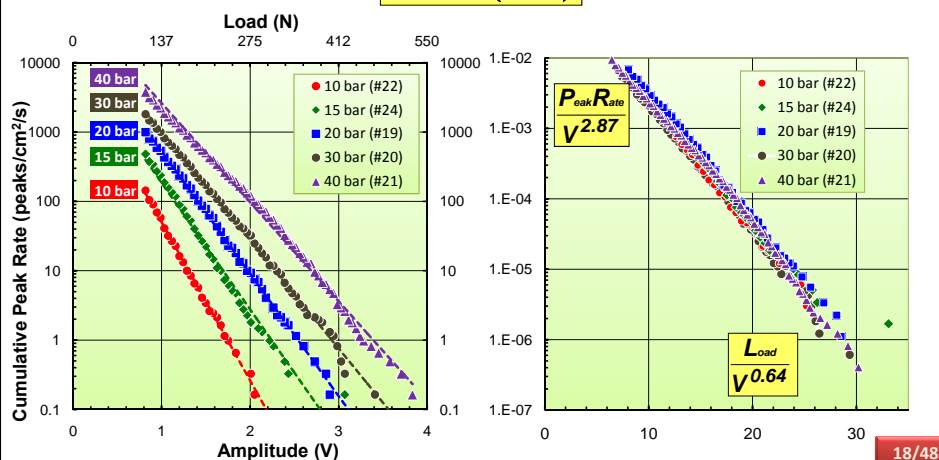
■ Peak rate follows an exponential law: $PR = k e^{-\frac{F}{F_0}}$



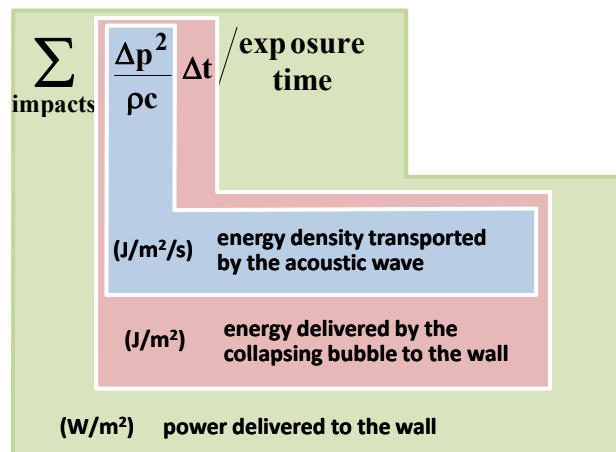
Scaling law for peak rate

■ PPHS at different velocities collapse when using the following scaling law:

$$\frac{P_{\text{peak}} R_{\text{rate}}}{V^{2.87}} = f\left(\frac{L_{\text{load}}}{V^{0.64}}\right)$$



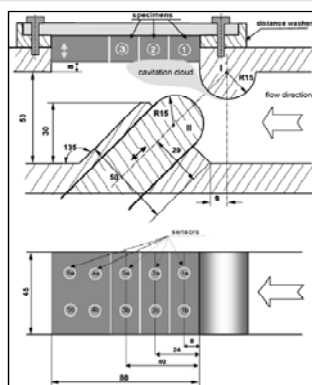
Erosive potential and PPHS (1/3)



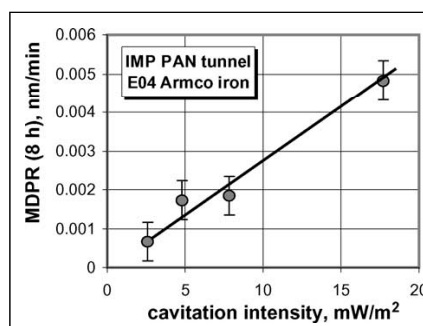
Hammitt (1979)

19/48

Erosive potential and PPHS (2/3)



Schematic of the cavitation chamber



Correlation between the cavitation intensity and the mean depth of penetration rate for E04 Armco iron



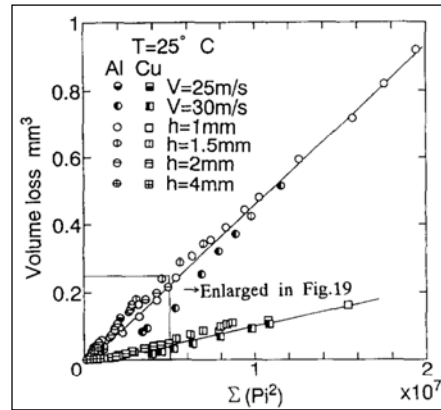
Visualization of cavitation (upstream pressure 12 bar, downstream pressure 1.2 bar, slot width 5 mm)

Krella and Czyzniewski (2008)
Steller et al. (2005)

20/48

Erosive potential and PPHS (3/3)

- linear relationship between volume loss and cumulative impact energy
- depends upon the material
- but independent of test conditions such as:
 - ✓ type of apparatus
 - ✓ flow velocity for Venturi tests
 - ✓ distance of specimen for vibratory tests



Okada et al. (1995)

21/48

The chain of phenomena

STEP 1

Large scale vapor structures break up into many small bubbles



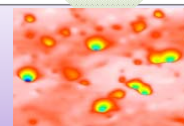
STEP 2

When collapsing (individually or collectively), each bubble generates a localized, high intensity, short duration impact load on the wall



STEP 3

Each impact load, if strong enough, creates a pit on the surface



STEP 4

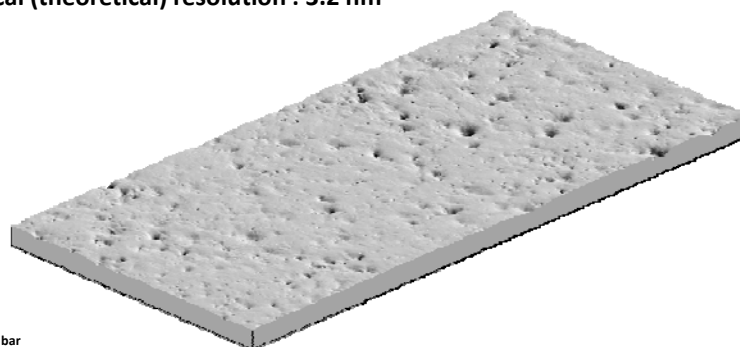
Repeated impulsive loading of the material generates pitting, failure and mass loss



22/48

Pitting tests analysis technique

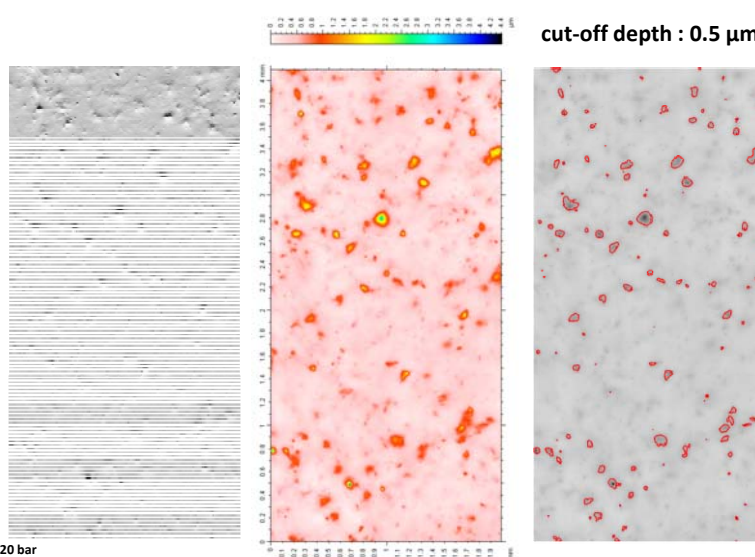
- Typical analyzed surface : 2 mm x 4 mm
- Several surfaces are analyzed if pit number is not enough for a statistical analysis
- Horizontal resolution : $1\ \mu\text{m} \times 1\ \mu\text{m}$
- Vertical (theoretical) resolution : 3.2 nm



SS A2205 – 20 bar
2 mm x 4 mm
ONR_12_surface_2

23/48

Identification of pits

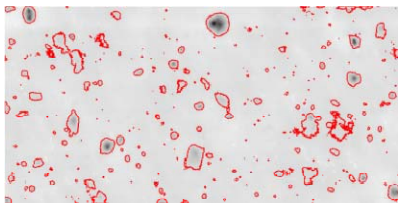


SS A2205 – 20 bar
2 mm x 4 mm
ONR_12_surface_2

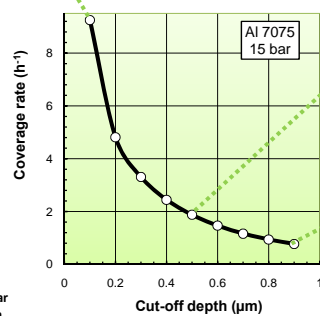
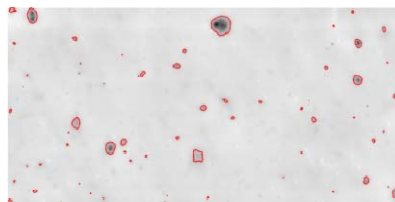
24/48

Influence of cut-off depth

cut-off depth : 0.1 μm

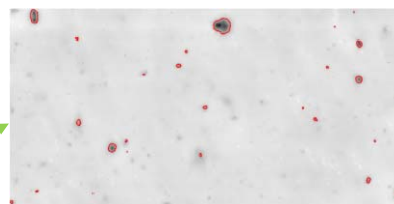


cut-off depth : 0.5 μm



Al7075 – 15 bar
2 mm x 4 mm
ONR_2_surface_3

cut-off depth : 0.9 μm



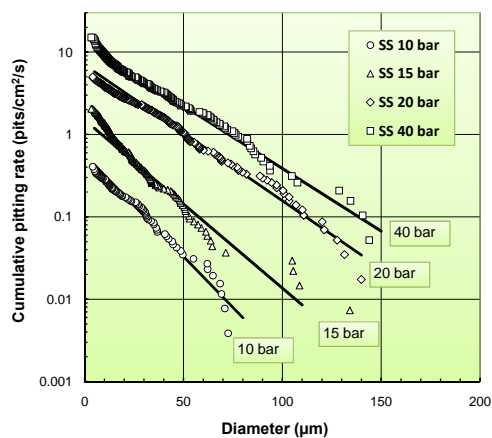
25/48

Distribution law for pitting rate

■ Cumulative pitting rate follows an exponential law: $N = \frac{8}{\pi \delta^2 \tau} e^{-\frac{2D}{\delta}}$

■ Two parameters:

- δ (length unit)
- τ (time unit)



26/48

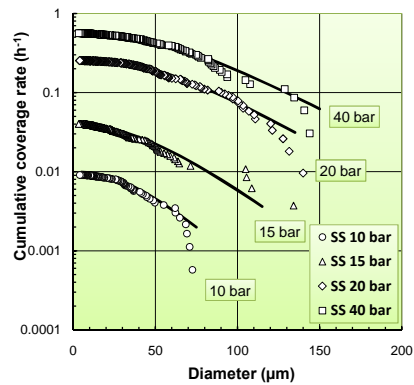
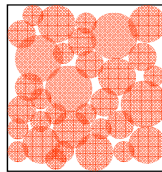
Interpretation of τ factor

■ Coverage rate:

$$\beta = \int_0^{\infty} \left(-\frac{dN}{dD} \right) \frac{\pi D^2}{4} dD = \frac{1}{\tau} \left(1 + \frac{2D}{\delta} + \frac{2D^2}{\delta^2} \right) e^{-\frac{2D}{\delta}}$$

■ if $D \rightarrow 0$ then $\beta \rightarrow (1/\tau)$

■ τ is the "coverage time"



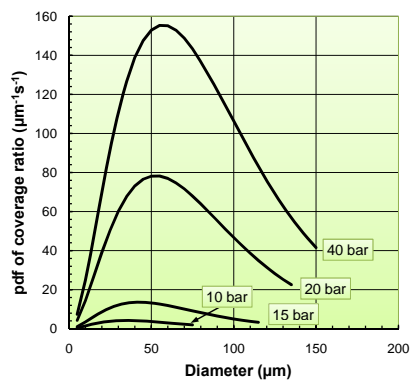
27/48

Interpretation of δ factor

■ PDF of coverage rate

$$-\frac{d\beta}{dD} = \frac{4}{\delta^3 \tau} D^2 e^{-\frac{2D}{\delta}}$$

■ Maximum occurs for $D = \delta$ i.e. pits in a bandwidth around δ contribute predominantly to cavitation erosion



28/48

Scaling laws for pitting tests

Cumulative pitting rate

$$N = \frac{8}{\pi \delta^2 \tau} e^{-\frac{2D}{\delta}}$$

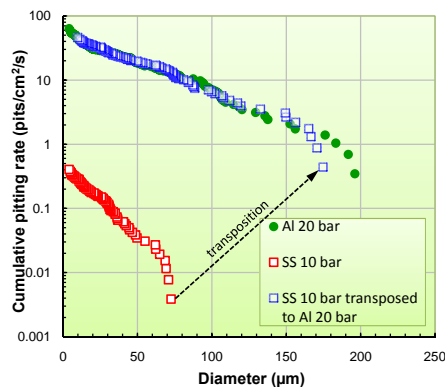
Scaling laws

$$\Rightarrow D \propto \delta$$

$$\Rightarrow N \propto \frac{1}{\delta^2 \tau}$$

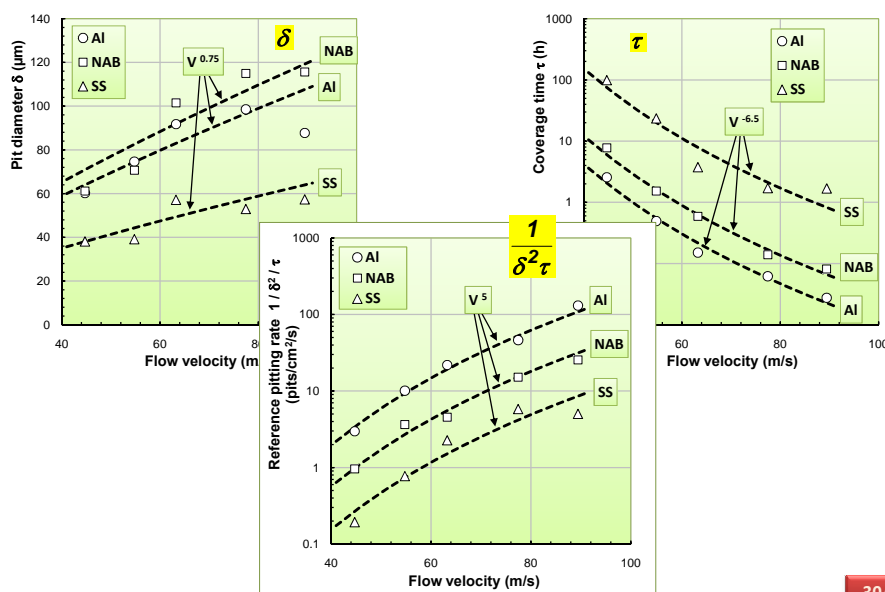
Non-dimensional pitting rate

$$\left. \begin{aligned} N^* &= \delta^2 \tau N \\ D^* &= \frac{D}{\delta} \end{aligned} \right\} \Rightarrow N^* = \frac{8}{\pi} e^{-2D^*}$$



29/48

Effect of flow velocity



30/48

Effect of material properties on maximum pit size

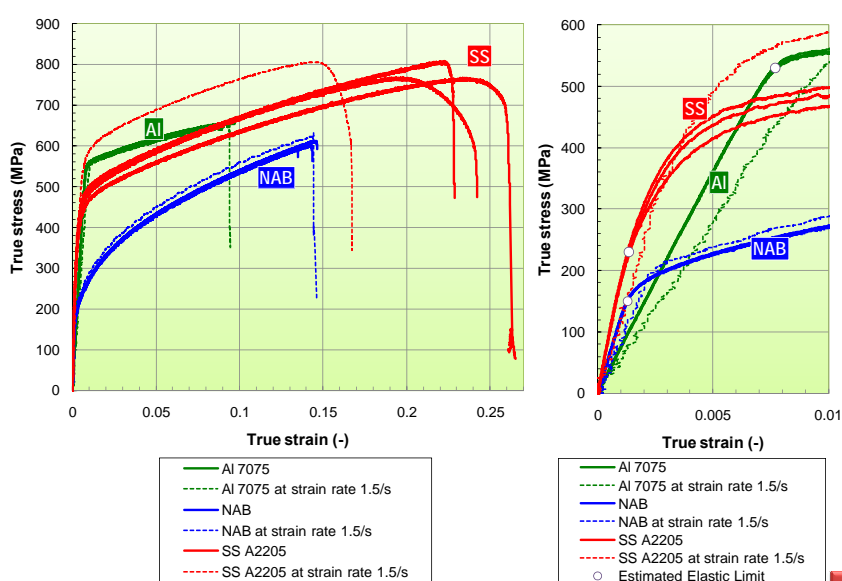
Operating conditions	Material	Maximum pit size measured D_{\max}	δ	D_{\max} / δ
40 bar	Al	203 μm	88 μm	2.3
	NAB	224 μm	116 μm	1.9
	SS	144 μm	57 μm	2.5
10 bar	Al	137 μm	60 μm	2.3
	NAB	112 μm	61 μm	1.8
	SS	73 μm	38 μm	1.9

■ Maximum pit size can reasonably well be predicted by the same scaling law i.e.

$$D_{\max} \sim \delta$$

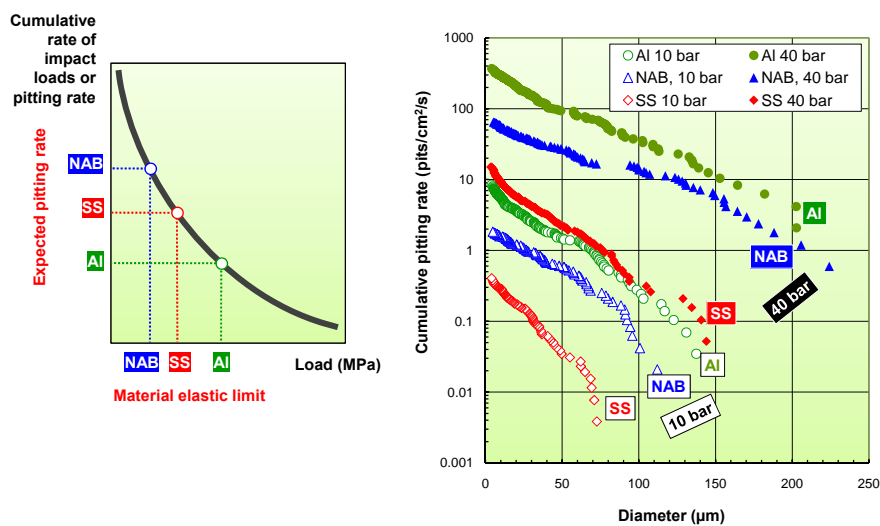
31/48

Effect of material properties on pitting rate



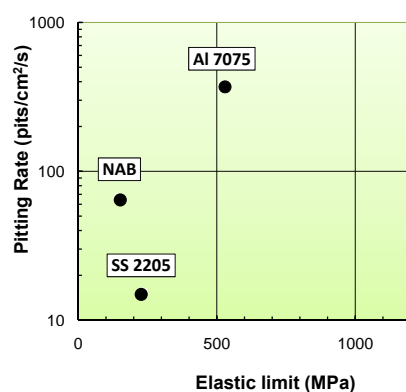
32/48

Effect of material properties on pitting rate



33/48

Effect of material properties on pitting rate (cont'd)

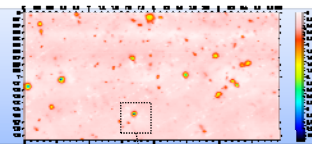


- Pitting damage is not correlated in simple terms with the elastic limit determined from conventional tensile tests
- Material properties under compressive loading would be more appropriate
- What about the effect of strain rate ?
- What about the influence of the pit analysis technique (cut-off depth...) ?

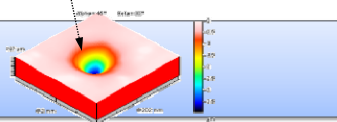
34/48

A method for estimating CI from pitting tests

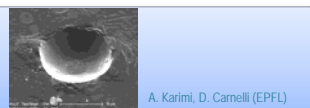
Conduct pitting tests
on polished samples



Analyze pits and determine diameter,
volume, depth...



Determine material properties
and response to impact loads
from nano-indentation tests

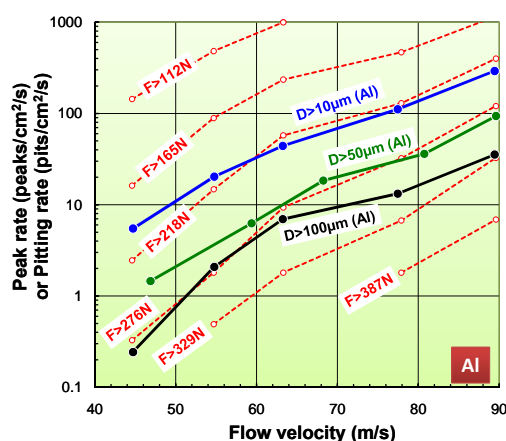


A. Karimi, D. Cornelli (EPFL)

For each pit, infer loading conditions
from pit characteristics and nano-indentation tests

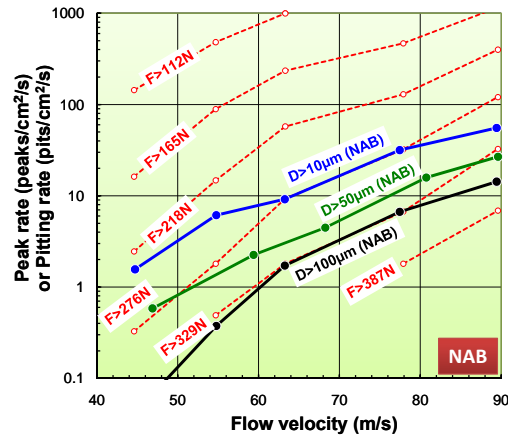
Determine the cavitation intensity of the flow
i.e. histogram of impact loads

Comparison Peak Rate / Pitting Rate



■ Peak rate and pitting
rate exhibit a similar
behavior with flow
velocity

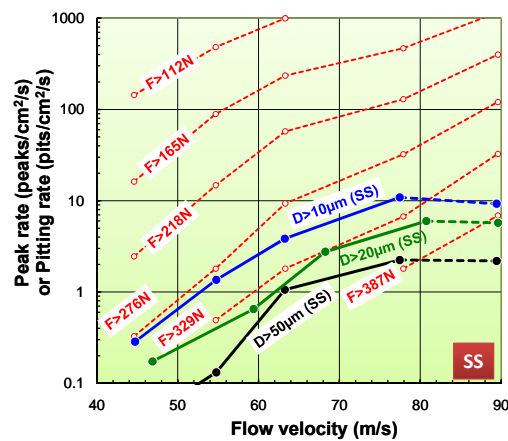
Comparison Peak Rate / Pitting Rate



■ Peak rate and pitting rate exhibit a similar behavior with flow velocity

37/48

Comparison Peak Rate / Pitting Rate



■ Peak rate and pitting rate exhibit a similar behavior with flow velocity

38/48

The chain of phenomena

STEP 1

Large scale vapor structures break up into many small bubbles



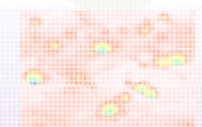
STEP 2

When collapsing (individually or collectively), each bubble generates a localized, high intensity, short duration impact load on the wall



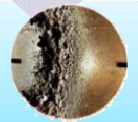
STEP 3

Each impact load, if strong enough, produces a pit on the surface



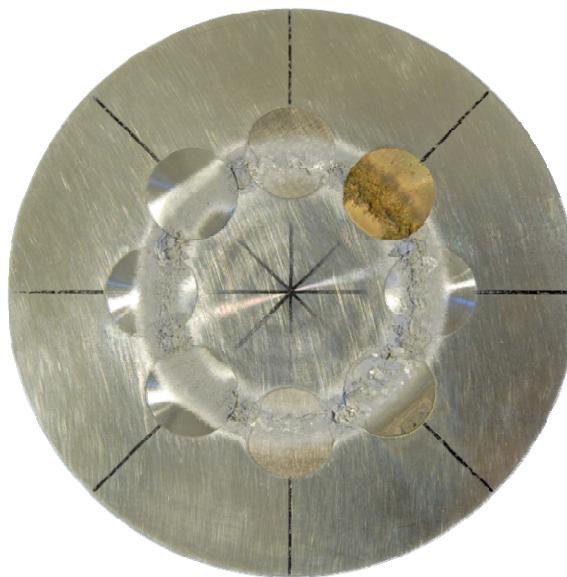
STEP 4

Repeated impulsive loading of the material generates failure and mass loss

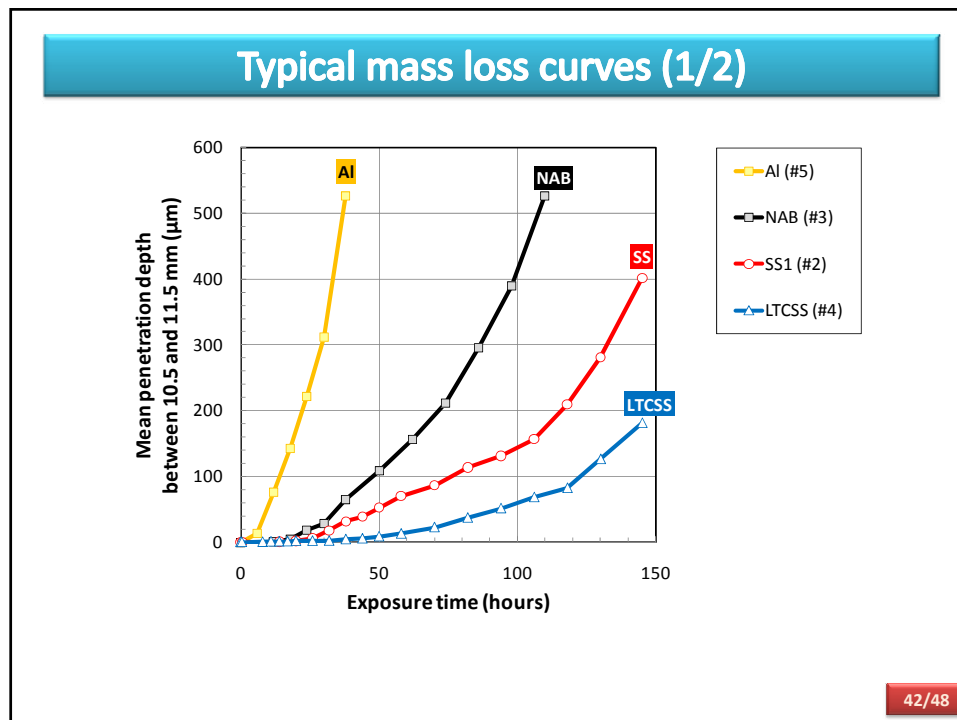
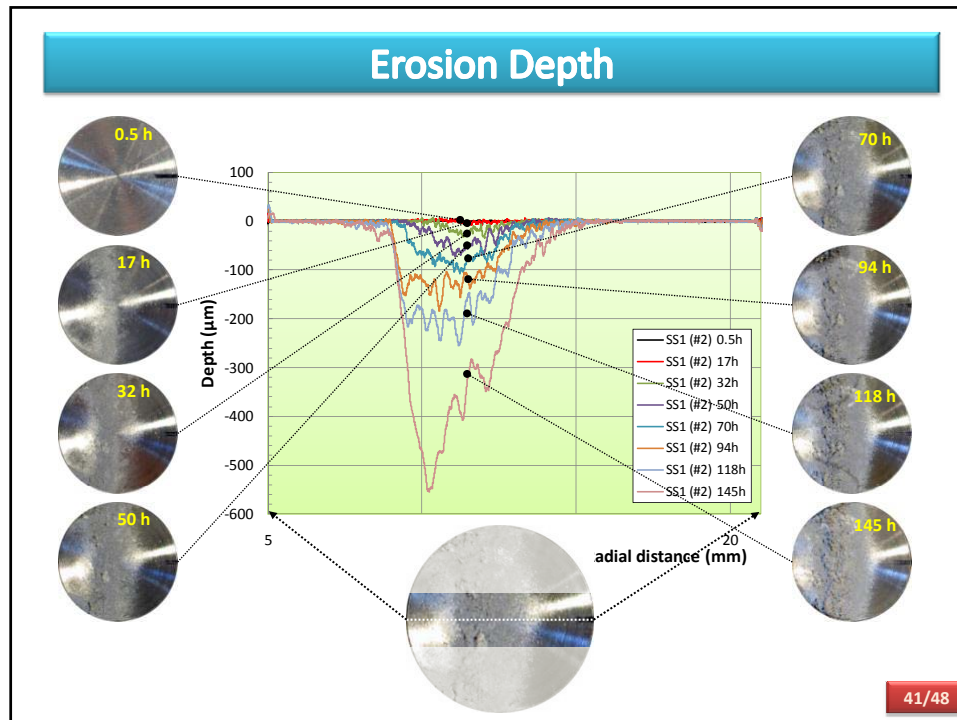


39/48

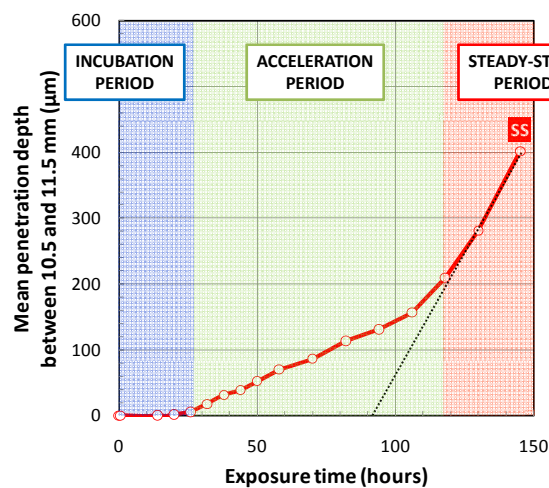
Visualization of mass loss



40/48

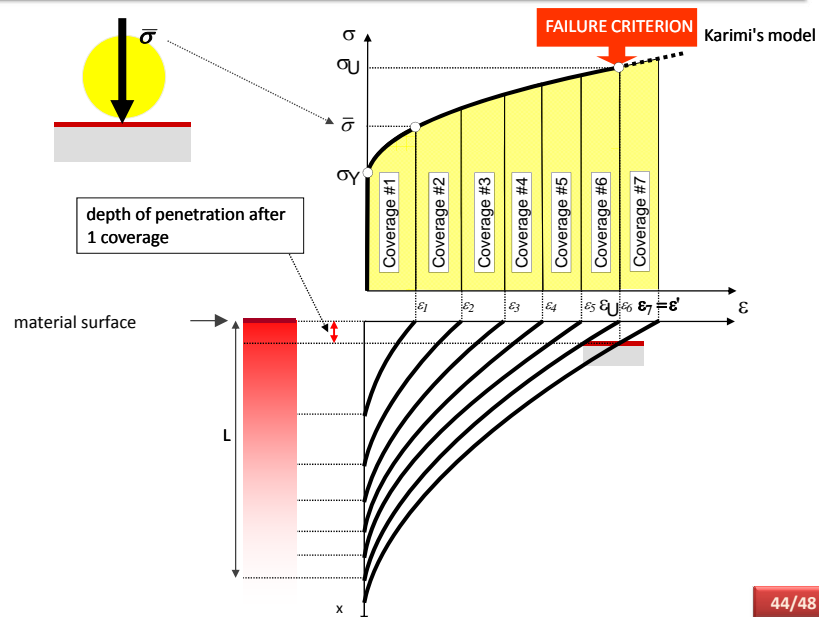


Typical mass loss curves (2/2)



43/48

Modeling of material response



44/48

Basic formulas (in the simplified case of impacts of constant load)

■ Incubation period

$$T_i = \tau \frac{W(\varepsilon_U)}{W(\varepsilon_1)}$$

coverage time τ energy to failure $W(\varepsilon_U)$ energy of a single impact $W(\varepsilon_1)$ number of coverages to failure

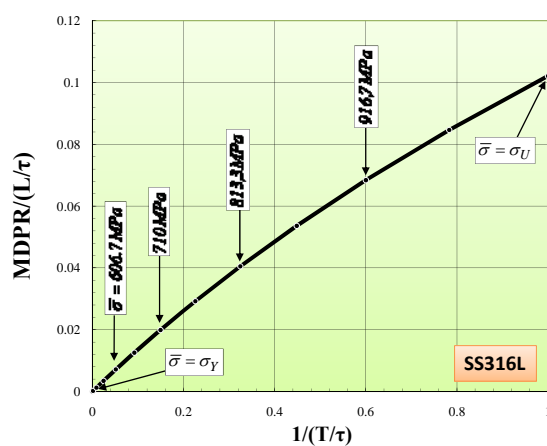
■ Steady-state erosion rate

$$\text{MDPR} = \frac{L}{\tau} \left[\left(\frac{\varepsilon'}{\varepsilon_U} \right)^{1/\theta} - 1 \right]$$

thickness of hardened layer L shape factor of hardness profile θ ultimate strain (failure criterion) ε_U

45/48

Prediction of incubation time / erosion rate relationship

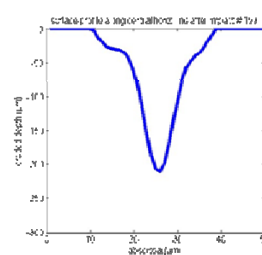
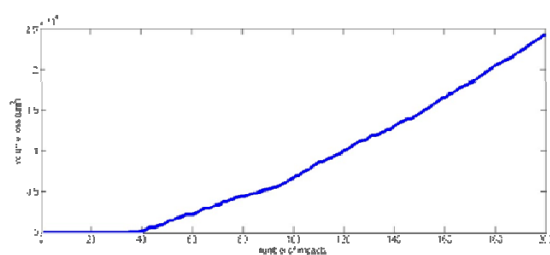
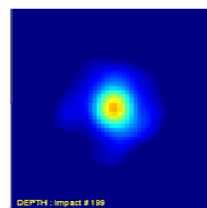
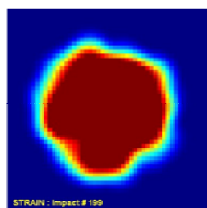
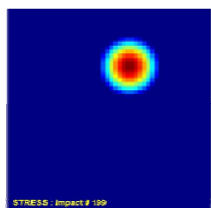


$$\frac{1}{\text{MDPR}} = k T_i^\alpha$$

(0.6 < α < 1)

46/48

Simulation example



47/48

ACKNOWLEDGMENTS

K.H. Kim (ONR, USA)
 R. Vogelsong (ONRG, UK)
 A. Karimi (EPFL, Switzerland)
 D. Carnelli (EPFL, Switzerland)
 M. Donnelly (NSWCCD, USA)
 F. Martin (NRL, USA)
 G.L. Chahine (Dynaflow, Inc., USA)
 E. Johnsen (University of Michigan, USA)
 S. Schmidt (TU München, Germany)

Some Remarks on Hydrofoil Cavitation

Roger E.A. Arndt

Saint Anthony Falls Laboratory, University of Minnesota
2 Third Avenue SE, Minneapolis, MN 55414

arndt001@umn.edu

ABSTRACT

Many types of turbomachinery must often operate in the cavitating regime. A common form of attached cavitation on turbomachinery blades is sheet/cloud cavitation. Sheet/cloud cavitation is a highly dynamic flow pattern generally considered to be highly erosive. There is a need to understand erosion mechanisms in order to develop effective erosion attenuation systems and develop effective algorithms for more advanced cavitation monitoring systems. In addition, the unsteady loads created by this form of cavitation in pumps, turbines and propellers are significant. Other issues of significance are noise and out-gassing mechanisms that create bubbly flows that cause instability in turbomachinery. At the same time these out-gassing mechanisms could have useful industrial application. Many of these issues are exacerbated by de-regulation of the power industry.

This paper reviews numerical and experimental investigations of sheet/cloud cavitation carried out at the St. Anthony Falls Laboratory and two collaborating facilities¹ for more than a decade. Although significant advances have been made in the analysis of this flow several issues are still unresolved. The purpose of this paper is to examine the overall features of the problem, review the progress made to date and suggest avenues for new investigation.

NOMENCLATURE

c	chord length of hydrofoil [m]
g	gravitational acceleration [m/s^2]
h	span of hydrofoil [m]
l	length of cavity [m]
p_v	vapor pressure of liquid [N/m^2]
p_∞	freestream static pressure [N/m^2]
Re	$= cU_\infty/\nu$. Reynolds number [-]
St	$= fc/U_\infty$. Strouhal number [-]
U	streamwise velocity [m/s]
U_∞	freestream velocity [m/s]
α	angle of attack [degrees]
ρ	fluid density [kg/m^3]
σ	$= 2(p_\infty - p_v)/\rho U_\infty^2$, cavitation number based on vapor pressure [-]

1. INTRODUCTION

Various types of cavitation on surfaces can be found in practice, including bubble cavitation, sheet cavitation, cloud cavitation, and various forms of vortex cavitation. In spite of

considerable research, there are still many features of the problem that have not been properly explored. Once cavitation occurs, a given flow field is significantly modified because the lowest pressure in the flow is typically limited to vapor pressure. The effect of cavitation on lift is directly related to the observed degradation of performance of turbomachinery due to cavitation. It is well known that the modeling of even partial, time-averaged cavities is not simple, due to the inverse character of the flow representation in the vicinity of the cavity and its wake. In addition, partial cavity models cannot explain the break-up of sheet cavitation at the trailing edge into detached cavitation clouds. The process is inherently unsteady even for steady free stream conditions. Within a certain envelope of cavitation number, σ , and angle of attack, α , the process is also periodic. Using a simple reentrant jet model, Arndt et al (1995) were able to show that for cavity lengths, l , less than about 75 % of a chord length, an estimate of frequency of oscillation is given by

$$\frac{fl}{U} = 0.25 \sqrt{1 + \sigma} \quad (1)$$

This creates a modulation of the trailing cloud cavitation that is highly erosive and very noisy. Figure 1 contains a pictorial display of the various types of cavitating flow that were observed on a NACA 0015 hydrofoil at various combinations of angle of attack, α , and cavitation number, σ . Several different cavitating regimes occur depending on the combination of σ and α .

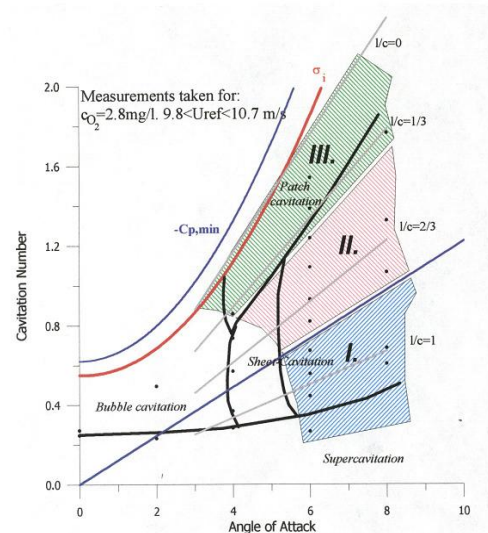


Figure 1. Types of cavitation found on the NACA 0015 hydrofoil.

¹ Versuchsanstalt für Wasserbau, Oberrach, Germany and Osaka University, Japan

The demarcation between “inception” and $-C_{pm}$ (computed) varies such that σ_i is always less than $-C_{pm}$, as expected. Note that sheet cavitation can be sub-divided into two regions such that at higher angles of attack ($\alpha \geq 5^\circ$) the flow had a wider dynamic range. At low angle of attack, say less than 4° , only bubble cavitation occurred. At intermediate angles of attack and relatively high values of σ , cavitation inception is in the form of patch cavitation.

Note that in this portrayal the demarcation between Type I and Type II oscillations occurs for a cavity length, $l/c = 0.75$.² This is predicted by inviscid theory for a thin flat plate as illustrated by Figure 2. Note in Figure 2a, that cavity length increases with decreasing σ up to a normalized cavity length of 0.75. This corresponds to Type II oscillations where Equation 1

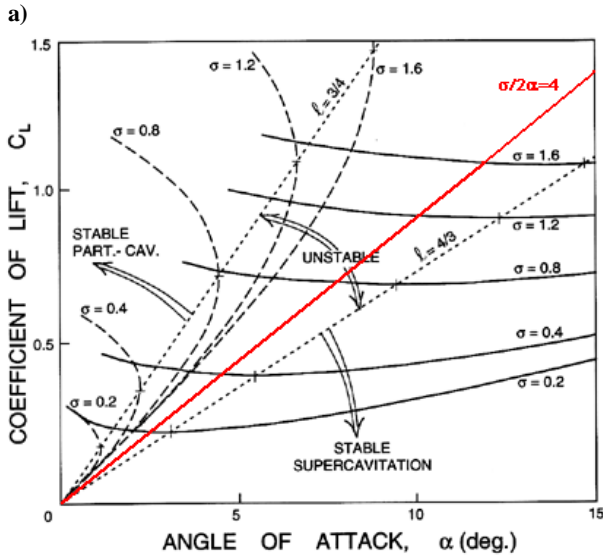
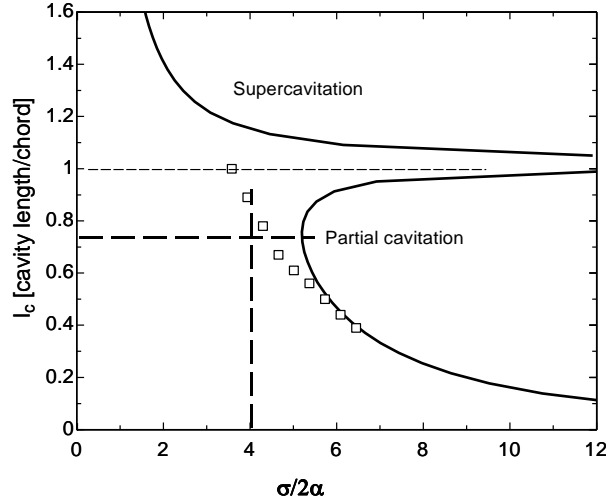


Figure 2. a) Flat plate theory. Sample experimental data for a NACA 0015 foil are shown with open circles (adapted from Watanabe et al 2001) b) Lift coefficient. Dashed lines are for partial cavitation. Solid lines are for supercavitation. The dotted lines denote the region where $dC_L/d\alpha < 0$ (adapted from Brennen 1995)

² Tunnel blockage modifies this slightly (Watanabe, unpublished)

is an approximation of the oscillation frequency. For lower σ , the flow is transitional corresponding to Type I oscillations. Figure 2b illustrates that a region of instability exists for $3/4 \leq l/c \leq 4/3$.

The significance of this demarcation is illustrated by some lift data collected in Obernach, Germany (Arndt et al, 2000, Figures 3 and 4). Note the bifurcation in the data at $\sigma/2\alpha = 4$ at which point lift oscillations are the most intense.

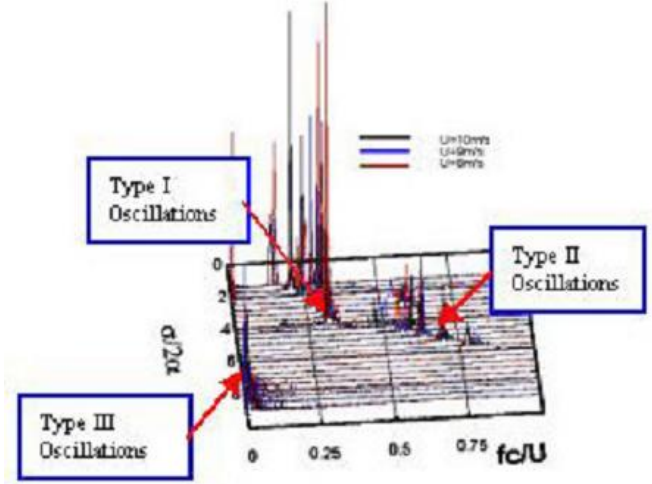


Figure 3. Measured lift spectra for a cavitating NACA 0015 hydrofoil.

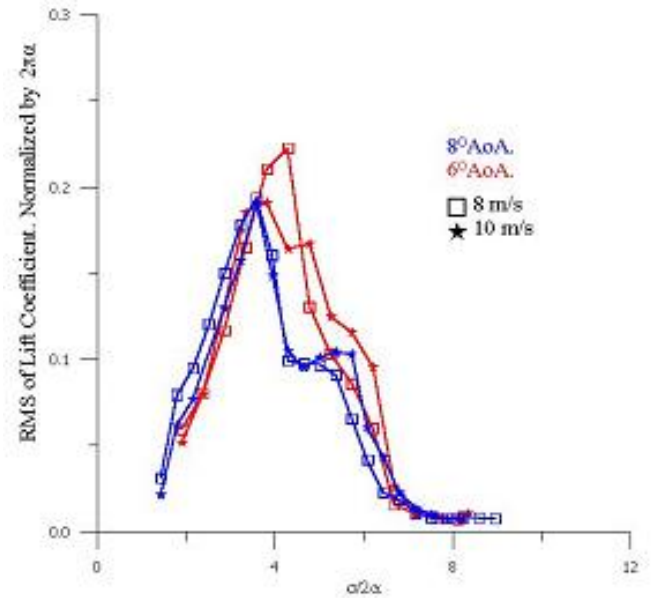


Figure 4. Normalized rms lift oscillations.

2. NUMERICAL MODELING

Cavitating flows are challenging to model numerically, since they are turbulent, highly dynamic and highly unstable two-phase, gas-liquid flows. There currently is no physical model that satisfactorily describes the phenomena associated with cavitation in the closure region. However, the events in this closure region are important, since the dynamics of oscillating partial cavities, and the associated dynamics of lift, are closely coupled to them. One method for working around this lack of a

physical model is to use Large Eddy Simulation (LES). A possible simplification of complex cavitating flows is to assume the gas-liquid flow as a virtual single phase fluid with a sharp density change when pressure drops below some critical value (Kubota et al. 1992, Song et al. 1997). Promising results have been obtained with these simulations, indicating that the approach can capture the main physics of cavitating flows (Song et al. 1997, Qin et al. 2003, Arndt et al. 2004, Qin 2004).

On the experimental side, phase-locked, time-resolved photography triggered off piezoelectric pressure sensors (essentially providing instantaneous pressure iso-surfaces of a cavitating flow) qualitatively correlates well with the LES in the wake of the hydrofoil. The identification of flow structures (which are being shed at inverse time scales of tens of, and sometimes several hundred Hz), requires Time-Resolved Particle Image Velocimetry (TR-PIV). The typical way to employ PIV in cavitating flows is to use fluorescent seeding particles, and then optically (usually long-pass) filter the scattered light so that only the fluorescent light from the particles, but not the direct reflections from the bubbles are recorded on the camera. The region where cavitation occurs is then identified by some masking technique, and excluded from cross-correlation processing. On the other hand, if one is after velocity information inside cavitation clouds, the vapor/gas bubbles can be used as “particles” (Arndt et al. 2007). Only the gas phase velocity is then being measured. This had been applied successfully to bubbly wakes resulting from air-ventilated cavities by Wosnik et al. (2004), but is somewhat more problematic in natural, vaporous/gaseous cavitation since “seeding particles” can simply disappear between frames due to condensation.

The LES identified five types of discrete, substantially periodic vortex shedding mechanisms. These mechanisms are illustrated in Figures 5a-c. In particular, cloud cavitation (having a clockwise vortical structure when flow is from right to left) is shed from the suction side of the hydrofoil. This induces a counterclockwise vortex from the pressure side, forming a vortex pair that dominates the wake structure.

The instantaneous velocity field is used to investigate the unsteady vortical structures shed from a cavitating hydrofoil and their evolution in the wake. To facilitate better analysis, the upstream-specified streamwise velocity was subtracted from the instantaneous velocity field of the whole computational domain. Figure 5a illustrates an instance of a large negative (clockwise) rotation when flow is from right to left) vortex structure containing a large amount of bubbles being shed into the wake near the trailing edge of the suction side (type A vortex) and a positive (counterclockwise rotation) vortex from the pressure side (type B vortex) that is being induced by the type A vortex. Within a short period of time, a vortex pair containing type A and type B vortices is well formed in the wake immediately downstream of the trailing edge. Since a type A vortex is typically located downstream of a type B vortex, the induced velocities tend to move the vortex pair slightly upward in the cross streamwise direction. As a result, the vortex pair moves diagonally at a speed roughly equal to the free-stream speed, which results in a slightly slower convection speed of this vortex pair in the streamwise direction. There is also a secondary negative vortex (type C vortex) formed above the suction side

near the trailing edge as is also shown in Figure 5b. This type C vortex is much weaker in strength than the type A vortex, but it also induces a corresponding secondary positive vortex (type D vortex) from the pressure side and eventually forms a secondary and weaker vortex pair in the wake (Figure 5c). The primary vortex pair, type A and type B, are periodically shed into the wake while the formation of the secondary vortex pair, type C and type D, are less regular. There is typically one secondary vortex pair between two primary vortex pairs, but occasionally two secondary vortex pairs are observed. Between the primary and secondary shedding vortices, there is a certain time period in which only positive vortices (named as type E vortices) are shed from the pressure side of the hydrofoil.

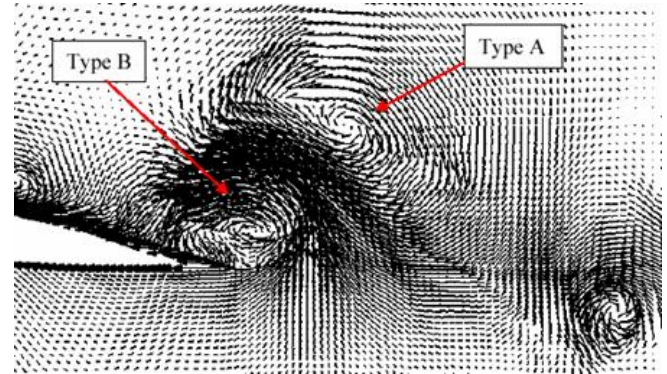


Figure 5a. A primary vortex pair (type A and B) being shed at the trailing edge of a NACA 0015 hydrofoil (note that here the angle of attack is +8 degrees).

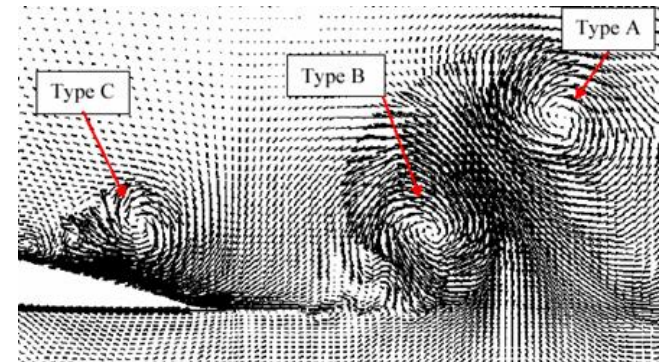


Figure 5b. The primary vortex pair (type A, B) moves into the wake at approximately a 45 degree angle, with the ejection velocity between the vortices A and B pointed at 135.

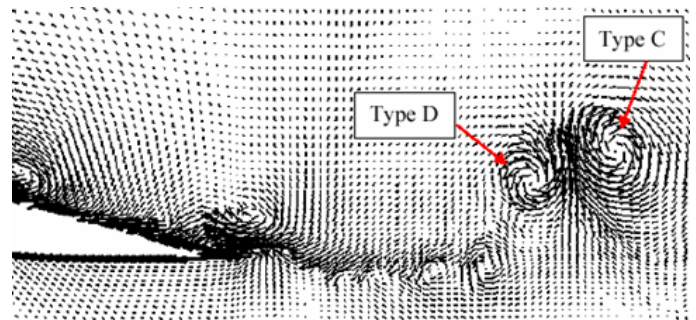


Figure 5c. Secondary vortex pair (type C and D) moving into the wake.

A unique feature of our simulations is the consideration of dissolved incondensable gas coming out of solution. This is illustrated in Figure 6. To facilitate better analysis, the upstream-specified streamwise velocity was subtracted from the instantaneous velocity field of the whole computational domain. In this figure, void fraction distribution is superimposed on the velocity vector fields of the primary vortex pair (type A and B), it can be seen that the cavitation cloud being shed appears to coincide with the shedding of the primary vortex pair. This can be compared with experiment (phase-locked strobe photography with variable time-delay triggered off pressure peaks on an instrumented hydrofoil) in Figure 7.

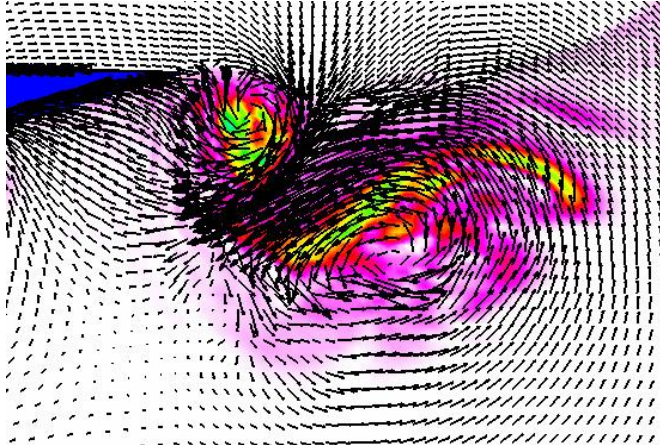


Figure 6. LES of cavitating NACA 0015 hydrofoil, the angle of attack is -8 degrees, $\sigma = 1.1$. Type A and B vortices can be seen. The void fraction of incondensable gas is overlaid in color. The cavitation cloud being shed appears to coincide with the shedding of the primary vortex pair.



Figure 7. Phase-locked photograph of cloud cavitation.

A typical PIV image acquired as a cavitation cloud is being shed in the hydrofoil wake is shown in Figure 8. The type A-B primary vortex structure can be identified. Also note that in the presentation of the experimental results the free stream velocity was also subtracted. A cross-stream ejection velocity at an angle of -135 degrees can also clearly be seen.

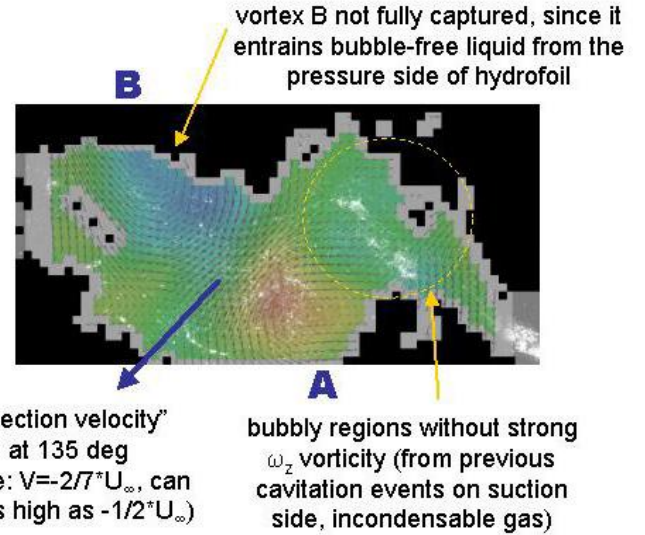


Figure 8. Velocity data in a cavitating hydrofoil wake, $\sigma = 1.1$. Primary vortex pair (type A and B) and ejection velocity are marked.

It is important to mention the interrelation between the periodically shed vortex structures and lift oscillations. This is illustrated in Figures 9 and 10. Figure 9 contains an experimental comparison between the spectral content of lift oscillations and the rate of vortex shedding into the wake. Note the strong correlation of frequency peaks in both signals. Figure 10 contains a simulation illustrating the same relationship.

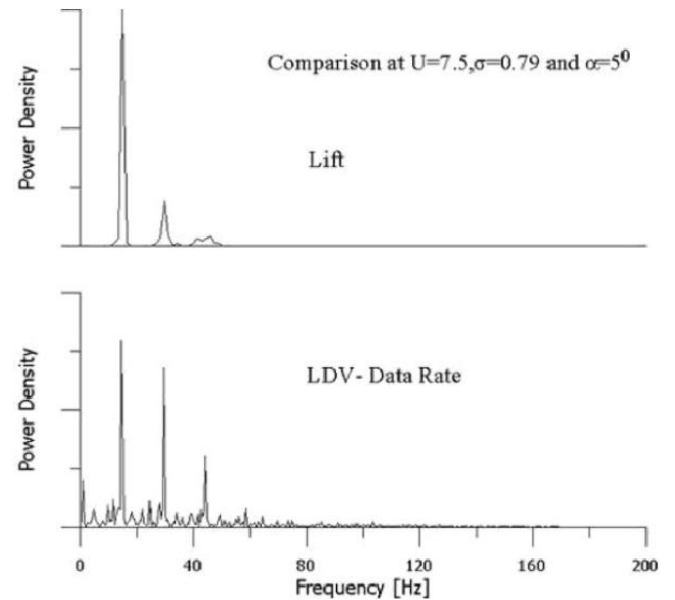


Figure 9. Comparison of lift dynamics with the FFT of data rate in a cavitating flow over a NACA 0015 hydrofoil. The fundamental frequency corresponds to a Strouhal number, $fc/U = 0.15$

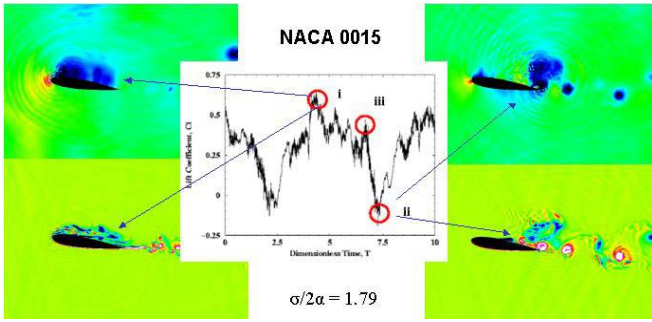


Figure 10. Relation between lift oscillation and cavitating flow structures. The upper pictures are pressure and the lower are vorticity

OTHER FACTORS

The introduction provided a brief synopsis of the general features of sheet/cloud cavitation as deduced from experiments and simulation of flow over a NACA 0015 hydrofoil. Several other geometric factors have been studied such as blade shape, and environmental factors such as water quality, surface characteristics and experimental facilities utilized in the studies.

Effect of Hydrofoil Shape

A review of earlier studies with different foil shapes is given in Fujii et al (2007). This paper was limited to a study of: three NACA foils with different thickness, and three flat plate type foils with different leading edge radius, and a special foil denoted Cav 2003 as illustrated in Figure 11. All seven shapes were studied at Osaka University, whereas only the Cav 2003 and NACA 0015 were studied in more detail at SAFL and Obernach. The Cav2003 foil is of special interest since this is the shape that was the subject of a workshop on comparison of numerical codes. A summary of the test conditions in each facility is given in Table 1.

Using high-speed video observation, Fujii et al found that the spectral characteristics of five different foil shapes were very similar as shown in Figure 12. The trend is very similar to observations made at Obernach and SAFL (Figure 13). However, the frequency of the Type I oscillations was considerably lower than observed in the other facilities. As discussed by Kawakami et al (2008), this may be due to the relatively small size and large blockage found in the Osaka water tunnel.

The results in Figure 12 show that the foil shape does not significantly affect either partial or transitional cavity oscillations. However, Fujii et al did observe differences in the flow and the cavity appearance on the various foils. This suggests that the flow details are not important for cavity oscillations. However, the component corresponding to partial cavity oscillation (Type II) can be found only for thinner foils. This shows that the foil shape affects the strength of partial cavity oscillations. Although not very clear, reentrant jets are observed both for transitional and partial cavity oscillations. It is generally accepted that the partial cavity oscillation is caused by the reentrant jet (Kawanami et al, 1997) and affected by the pressure gradient near the cavity trailing edge (Callenaere et al, 2001). This may be the reason why the strength of partial cavity oscillation was affected by the foil thickness. In the case of transitional cavity oscillations the situation is more complex. Arndt et al (2000) noted that there are two competing mechanisms for the induced shedding of cloud cavitation. At high values of $\sigma/2\alpha$, reentrant jet physics dominate with Strouhal number based on *cavity length* of $fl/U \approx 0.3$, whereas at low values of $\sigma/2\alpha$ bubbly flow shock wave phenomena dominate with a Strouhal number based on *chord length* of $fc/U \approx 0.2$. Similar results are reported by Kawakami et al (2008).

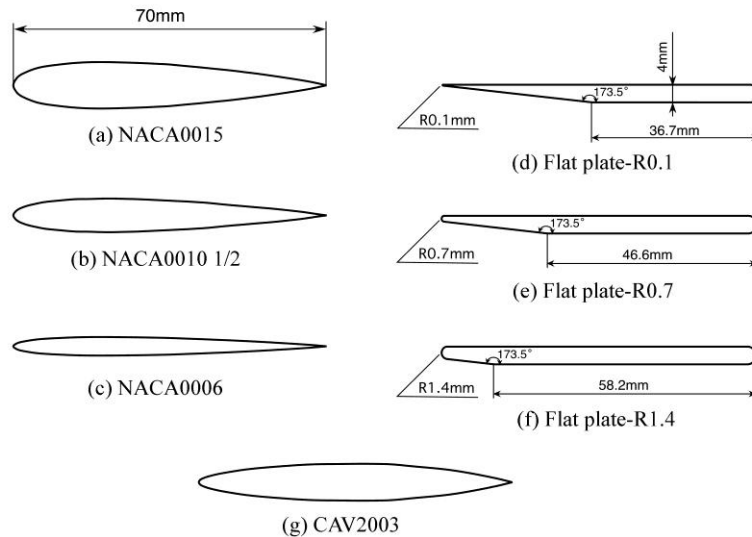


Figure 11. Foil shapes tested. The chord length was 70mm at Osaka, 81mm at SAFL and 128mm at Obernach.

Table 1: Summary of differences in each tunnel.

Tunnel and foil	Tunnel Dimensions (mm)	Foil Mounting	Chord Length (mm)	Aspect Ratio	Re	Gas Content (ppm)	Surface Finish	Roughness
Obernach	300 x 300	Fixed at both ends	128	2.35	1.02 E06	6.7	Anodized Aluminum	>1.16 μm
SAFL - Polished*	190 x 190	Cantilever	81	2.35	6.48 E05	13	Polished Steel	1.16 μm
7								
Anodized**						13	Anodized Aluminum	>1.16 μm
7								
Instrumented foil***						13	Aluminum	>1.16 μm
						7		
Osaka	100 x 70 (h x w)	Cantilever	70	1.43	3.5 E05	3.5	Polished Steel	1.16 μm

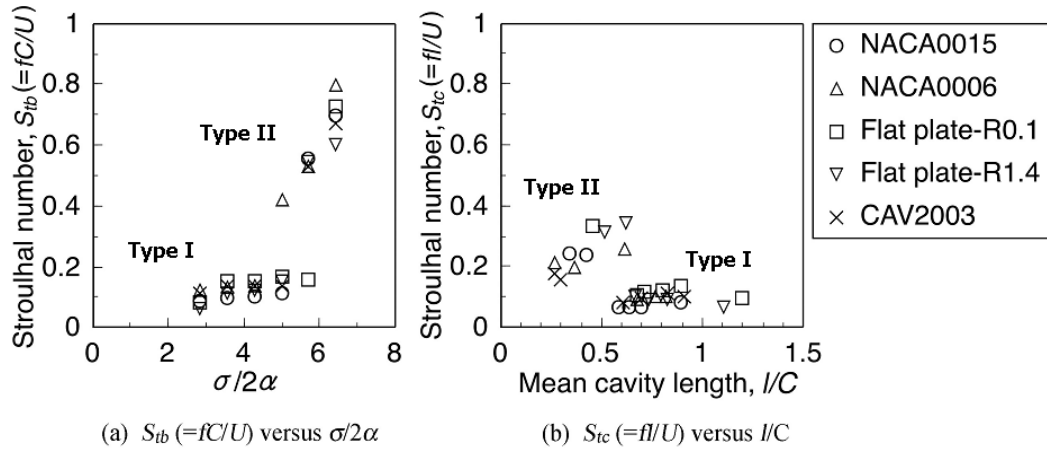


Figure 12. Oscillation frequency measured in the Osaka tunnel at an angle of attack of 8 degrees (Fujii et al., 2007).

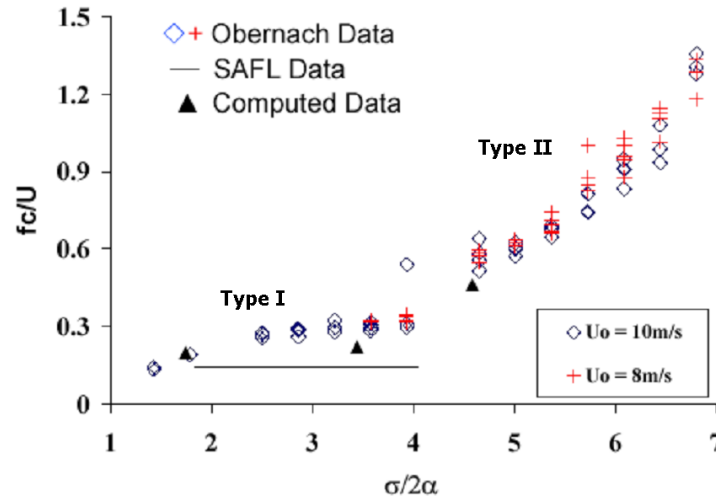


Figure 13. Video observation of the NACA 0015 foil in the Obernach tunnel. Measurements were made at an angle of attack of 8 degrees. Adapted from Arndt et al. (2000).

Although there does not appear to be a significant effect of foil shape on oscillation frequency there are other subtle differences that have not been discussed in the literature. An example is the findings of Williams et al (2009) who compared the oscillation characteristics of the Cav 2003 and NACA 0015 shapes as part of a study of the effect of surface characteristics. One of the motivations in believing that surface characteristics would play a role in sheet cloud cavitation is the observation that even under intense oscillatory flow a hydrofoil can become fully wetted during a fraction of each oscillation period. This implies that factors influencing inception are also relevant for more developed cavitation. This is illustrated in Figure 14 (Kawakami et al, 2008). Note the significant increase in dwell time for stainless steel. This was one of the factors considered in the Williams et al study as shown in Figure 15. Note that any fully wetted period occurred over a narrower range of $\sigma/2\alpha$ and the effect was much less noticeable than for the NACA 0015 foil.

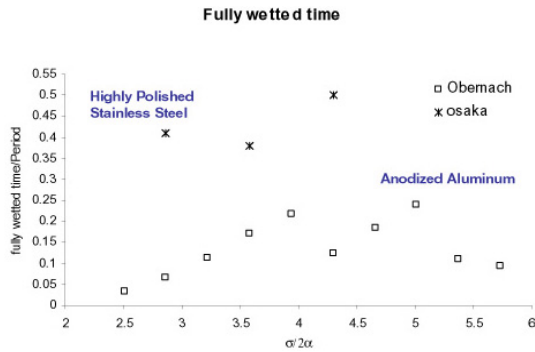


Figure 14. Fully wetted time on a NACA 0015 hydrofoil (Kawakami et al., 2008).

The reason for the differences is not fully understood. We were not able to observe any fully wetted phenomena with the stainless steel Cav 2003 foil at 6° or 8° as was the case of for observations on a NACA 0015 foil shown in Figure 14. Fully wetted phenomena were only detected at relatively low angles of attack. Hence the data in Figure 15 correspond to an angle of attack of 4 degrees. This has not been explained, but numerical simulations provide some clues. This is illustrated in Figures 16 – 18. Shown in Figure 16, similar vortex structures in the cavitating wake of the Cav 2003 foil are noted in our numerical simulations.

However, as shown in Figure 17, the simulations indicate significant differences between the unsteady loads in cavitating and non-cavitating conditions for the two foil shapes. The higher level of unsteadiness for the non-cavitating Cav 2003 foils is traced to viscous separation at the trailing edge as shown in Figure 18.

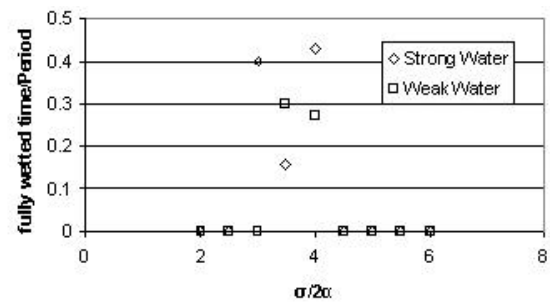


Figure 15. Fully wetted time on a stainless steel Cav 2003 hydrofoil at 4 degree angle of attack.

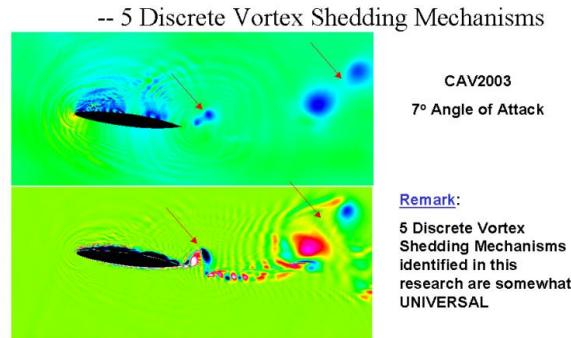
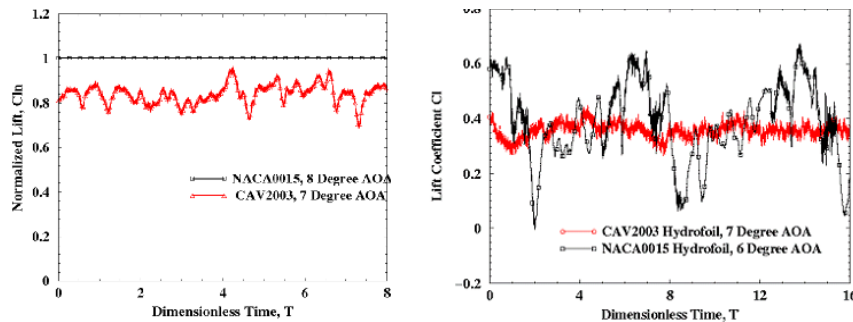


Figure 16. Numerical simulation of sheet/cloud cavitation on a Cav 2003 foil at 7 degrees angle of attack. (Qin, 2004)



Non-cavitating Condition

Cavitating Condition

Figure 17. Numerical simulations comparing oscillating loads on a Cav 2003 and NACA 0015 hydrofoils under non-cavitating and cavitating conditions.

Time Averaged Pressure Coefficients
Under Non-cavitating Conditions

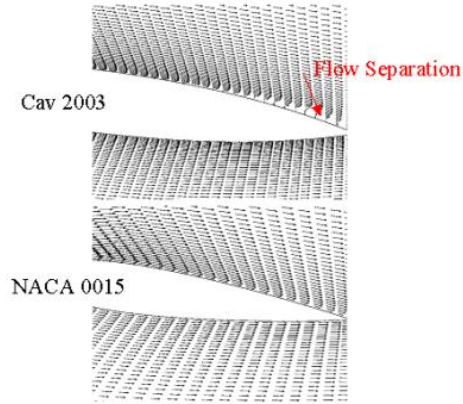
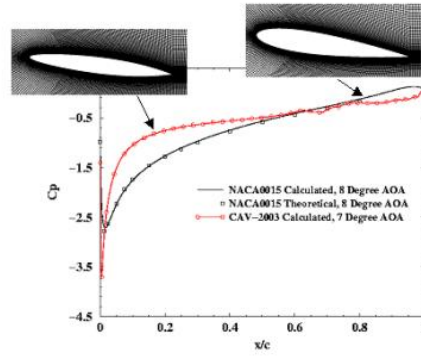


Figure 18. Calculation of non-cavitating flow over the NACA 0015 and Cav 2003 hydrofoils.

Surface Characteristics and Water Quality

As noted above, fully-wetted phenomena are a unique, albeit little known, characteristic of sheet/cloud cavitation. In the case of the Cav 2003 foil, significant dwell time in an oscillation cycle was only detected at relatively low angles of attack. This is not understood, but cavitation inception studies also provided further insight. As expected, the inception physics change drastically at an angle of attack between 2 and 3 degrees. This is due to the dramatic shift in the minimum pressure position from mid chord to the leading edge. A significant finding was that for angle of attack less than 3 degrees, there is no measurable effect of either the surface characteristics or water quality. There is, however, a significant effect of both surface characteristics and water quality at higher angles of attack, as shown in Figure 19, where the data deviate in a consistent manner from $-C_{pm}$ with increasing angle of attack. There is also a measurable effect of the type of surface and water quality. Also shown in Figure 19 is a comparison with the data of Coutier-Delgosha et al. (2007) who also performed inception measurements with the Cav 2003 hydrofoil. The agreement is very good, lending support the observations shown here.

Williams et al (2009) studied three different surfaces: anodized aluminum (hydrophilic), Teflon® (hydrophobic), and highly polished stainless steel (hydrophobic). Contact angle was

measured with a photographic technique developed by three of the undergraduates working on the project. Studies were made in both weak and strong water. Significant surface effects were found, but were unexpected in the sense that they did not correlate with measured contact angles. A full explanation for the noted effects of both water quality and surface characteristics is not at hand. However, the trend is qualitatively predicted by Amromin (2007). His results contain calculations of the difference between the minimum pressure coefficient and σ for hydrophilic and hydrophobic surfaces that indicate a measurable effect. However, his theory is for sheet cavitation whereas inception was observed to be mainly patch cavitation. In addition, the predicted difference between hydrophilic and hydrophobic surfaces was not noted in the experiments. Hence a complete explanation of our results is not at hand.

The results of this research are mixed. We found that surface characteristics have a significant effect on cavitation induced vibration and unsteadiness, but we were not able to correlate the differences with our contact angle measurements. We are continuing to pursue this research, since it shows great potential for elucidating some new cavitation physics. In this research, it was very difficult to separate the effects of surface characteristics and water quality. This is a factor that has implications for making meaningful comparisons with other data in the literature.

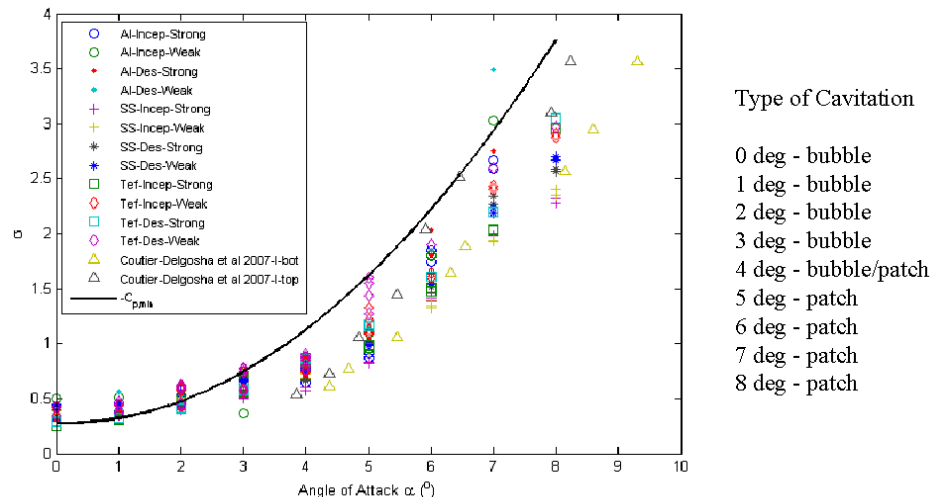


Figure 19. Inception Data for the Cav 2003 hydrofoil

SUMMARY AND CONCLUSIONS

Initial experiments and simulations utilizing LES provide a fairly coherent view of sheet/cloud cavitation. There are two types of oscillations. For cavity lengths less than about 0.75, reentrant jet physics dominate the oscillation period and a constant Strouhal number based on cavity length of about 0.3 is observed. For lower cavitation numbers, the issue is more complex since both reentrant jet physics and bubble cloud shockwave phenomena play a role. In spite of the relatively good agreement concerning oscillation frequency, observations of a cavitating NACA0015 foil in three different water tunnels revealed remarkably different cavity shedding appearance and behavior. Some of the differences were attributed to system instabilities. Harmonics in the shedding spectrum observed in the Osaka tunnel are attributed to the small size of the tunnel. In the much larger Obernach and SAFL tunnels, the harmonics are not observed. This difference is attributed to system instability since the harmonics are unique to the small Osaka tunnel. The effect of harmonics on the shedding behavior should be given careful consideration when studying cavitation instabilities in small water tunnels and inferring cavitation behavior on a full-scale model. Table 2 summarizes the observed differences and the hypothesized factor contributing to the difference.

Table 2. Summary of observed phenomena and the factors accounting for the difference.

observed difference	contributing factors
fully wetted time	gas content
	surface characteristics
spectral characteristics	gas content
	aspect ratio
visual shedding frequency	aspect ratio

In addition to a different cavitation behavior attributed to system instabilities, differences in gas content were found to significantly alter the lift spectrum of a cavitating foil. For a certain range of $\sigma/2\alpha$ near 4, the dominant frequency appears to double when the gas content is reduced by a half. This difference can be used to explain some of the discrepancies observed between tunnels.

It is also argued that surface effects can have a significant influence on fully wetted time during cavity shedding. The apparent contradiction of a long fully wetted time but high gas content in the case of the Osaka tunnel can be explained by separating inception and developed cavity observations. Surface effects play an important role in the initial inception of a fully wetted hydrofoil. Once a cavity sheet is developed, gas content is the main factor influencing cavitation behavior.

The hope is that knowledge of the effect of gas content, surface characteristics, and system characteristics will be more closely monitored in future cavitation studies. This becomes especially important when comparisons are made between water tunnels or when cavitation behavior in a water tunnel is studied in order to predict cavitation in actual applications. A more careful monitoring of these parameters will lead to a better understanding of the basic mechanisms affecting cavitation instabilities. These issues are especially important when utilizing experiments to further develop simulations.

ACKNOWLEDGMENTS

The National Science Foundation, Division of Chemical and Transport Systems in the Engineering Directorate and the Office of International Programs, and the Office of Naval Research supported most of this research. The research in Japan was supported by a Grand-in-Aid for Science Research of the Ministry of Education, Science, Sports, and Culture through a joint agreement with the National Science Foundation. Several of my colleagues played a major role in formalizing my ideas. This includes Dr. Andreas Keller of the Versuchsanstalt für Wasserbau of the Technical University Munich, Professor Yoshinobu Tsujimoto of Osaka University, Professor Morten Kjeldsen of the Norwegian University of Science and Technology and the many students who contributed over the years whose work is referenced herein. Special thanks go to Dr. Martin Wosnik, currently of the University of New Hampshire, for thoughtful discussions and countless hours of help obtaining and analyzing high-speed video.

REFERENCES

- Amromin, E.L. 2007 "Determination of cavity detachment for sheet cavitation" *J. Fluids Eng.*, v129, pp1105-1111
- Arndt, R.E.A., Ellis, C.R., Paul, S., 1995, "Preliminary investigation of the Use of Air Injection to Mitigate Cavitation Erosion," *J. of Fluids Eng.*, **117**, pp. 498-504.
- Arndt, R.E.A., Song, C.S.S., Kjeldsen, M., He, J., and Keller, A., 2000, "Instability of Partial Cavitation: A Numerical/Experimental Approach," *Proceedings of the 23rd Symposium on Naval Hydrodynamics*, Val de Reuil, France. Published by the Office of Naval Research, Naval Studies Board, National Research Council, National Academies Press, 2001
- Arndt REA, Song CCS and Qin Q (2004) Experimental and numerical investigations of cavitating hydrofoils. *22nd IAHR Symposium on Hydraulic Machinery and Systems*, Stockholm, Sweden, June 29-July 2, 2004.
- Arndt REA, Kawakami DT, Wosnik M (2007) Measurements in Cavitating Flows. In *Handbook of Fluid Mechanics*, eds. C. Tropea and J. Foss, Springer Verlag.
- Brennen, C 1995 *Cavitation and Bubble Dynamics* Oxford
- Coutier-Delgosha, O, Deniset, F, Astolfi, JA and Leroux, J-B, 2007, "Numerical Prediction of Cavitating Flow on a Two-Dimensional Symmetrical Hydrofoil and Comparison to Experiments" *Journal of Fluids Engineering*, **129**, March
- Callenaere, M, Franc, J-P, Michel, J-M and Riondet, M (2001) "The cavitation instability induced by the development of a reentrant jet" *J. Fluid Mech.*, vol. 444, pp. 223-256.
- Fujii, A., Kawakami, D.T., Tsujimoto, Y., Arndt, R.E.A., 2007, "Effect of hydrofoil shape on cavity oscillation," Accepted for publication in the *Journal of Fluids Engineering*
- Kawakami, DT, Fujii, A, Tsujimoto, Y and Arndt, REA (2008) An assessment of the influence of environmental factors on cavitation instabilities, *J. of Fluids Eng* **130**, 031303-1-8
- Kawanami, Y., Kato, H., Yamaguchi, H., Tagaya, Y., Tanimura, M., 1996, "Mechanism and control of cloud cavitation,"

Proceedings ASME symposium on Cavitation and Gas-Liquid Flows in Fluid Machinery and Devices, FED-236, 329-336.

Kjeldsen, M., Arndt, R.E.A., Effertz, M., 2000, "Spectral Characteristics of Sheet/Cloud Cavitation," *J. of Fluids Eng.*, **122**, pp. 481-487.

Kubota A, Kato H and Yamaguchi H (1992) A new modeling of cavitating flows: a numerical study of unsteady cavitation on a hydrofoil section, *J Fluid Mech*, **240**:59-96.

Qin Q, Song CCS and Arndt REA (2003) Numerical study of unsteady turbulent wake behind a cavitating hydrofoil, 5th *International Symposium on Cavitation*, Osaka, Japan.

Qin Q (2004) Numerical Modeling of Natural and Ventilated Cavitating Flows, *PhD Thesis*, University of Minnesota.

Song CCS, He J, Zhou F and Wang G (1997) Numerical simulation of cavitating and non-cavitating flows over a hydrofoil, *SAFL project report*, no.402, St. Anthony Falls Laboratory, University of Minnesota

Watanabe, S., Tsujimoto, Y., and Furukawa, A., 2001, "Theoretical Analysis of Transitional and Partial Cavity Instabilities" *J. of Fluids Eng.*, **123**, pp. 692-697.

Research on Francis turbine full-load surge

Peter K. Dörfler *, Olivier Braun*

*Andritz Hydro Ltd, Zurich

Yoshinobu Tsujimoto **

**Osaka University

peter.doerfler@andritz.com, Olivier.Braun@andritz.com

tujimoto@me.es.osaka-u.ac.jp

ABSTRACT

Francis turbines may produce spontaneous pulsation of pressure and output power when operating at very high discharge. In such cases there is a cavitating central vortex in the draft tube with variable cavity volume. The destabilizing agent is a parameter called mass flow gain factor, the derivative of cavity volume by the local discharge. Until 2010, this effect could not be properly assigned to the strongly differing discharge variations at either side of the cavity.

To enable reliable prediction of full-load stability, industrial studies have directly analyzed the vortex dynamics by means of unsteady 2-phase CFD. The response of the cavitating draft tube flow to forcing by time-dependent draft tube inflow was simulated. Based on the results, the structure and parameters of a fairly simple 1D transient model for the cavitating draft tube flow at high load have been identified. Contrary to common belief, the main contribution to mass flow gain turned out to be the upstream discharge, due to its flow-dependent swirl intensity. In addition, instability depends on a time lag caused by swirl propagation along the cavity.

NOMENCLATURE

C_c	cavitation compliance (equ. 1a)
D	draft tube intake diameter
f_{cc}	natural frequency of draft tube content
I	inertia parameter
p	static pressure
Q	discharge
R	linear resistance parameter
V_c	volume of cavity
t_d	time lag of upstream mass flow gain
χ	mass flow gain (equ. 1b)
κ	fraction of χ assigned to Q_1
1 (index)	draft tube intake
2 (index)	draft tube exit
c (index)	cavity

1. INTRODUCTION

Francis turbines are prone to 'rough running', in particular when the discharge deviates much from its value at best efficiency. Quite different physical mechanisms may be involved but most of them are due to the swirl downstream of the runner. Pressure pulsation and power swings occurring at high load [2][7], are of particular importance, because they may prevent the plant owner from utilizing the full potential output of a unit. Figure 1 gives an example of unacceptable power swings, with two Francis units operating at high load. In this case, the total station output measured at the switchyard shows a distinct beat because the two surging turbines have slightly different frequencies of pulsation.

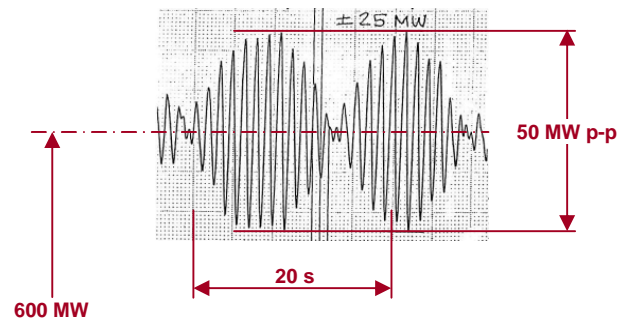


Figure 1 – Power swing due to full-load surge

Not all cases of disturbed operation at high load may be attributed to the same type of cause but quite frequently the observed phenomena follow a common pattern. The pulsation of pressure in different locations is synchronous around the turbine's draft tube. The pressure pulsation in the turbine intake is of similar magnitude and phase as in the draft tube. The pulsation frequency decreases with increasing load (i.e., discharge) and increases with increasing tail water level. Typical frequencies are between 20% and 100% of the frequency of runner rotation. By admitting or injecting air into the draft tube, the problem has been mitigated or even eliminated in a good number of cases but not in every case.

Based on the characteristics described above, the ordinary full-load must be a self-excited oscillation with a root cause quite different from the more frequent problems at partial load. There is no forcing phenomenon to be directly observed and the problem only occurs if a natural mode of the hydraulic system

exists without positive damping. In recent years, several researchers [6][8][11], have dealt with the problem and there is some consensus about the main factors contributing. The typical phenomenon of ‘full-load surge’ strongly depends on cavitation of the draft tube vortex which has, in this context, a sense of rotation against the runner. The vortex cavity has a rotationally symmetric appearance, at least in the draft tube cone just downstream of the runner.

2. CONCEPTS OF VORTEX-INDUCED INSTABILITY

Research dealing with the effects of draft tube surge in the hydraulic system began in the early 1980’s, by applying Brennen’s [1] definition of cavitation influence.

- (1a) $C = -\partial V_C / \partial p_C$ Cavitation compliance
 (1b) $\chi = -\partial V_C / \partial Q$ Mass flow gain factor

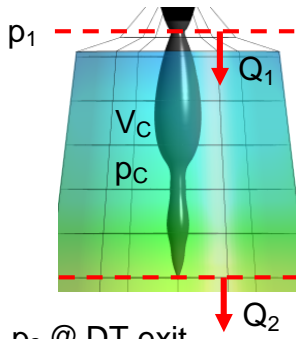


Figure 2 – Variables in a 1D draft tube model

The concept of cavitation compliance proved useful for understanding the occurrence of tailwater-dependent hydraulic resonances of the forced oscillation at partial load [3]. It could also explain the typical tendency of the full-load surge frequency to decrease with increasing turbine load.

Instability, on the other hand, can only occur if some effect introduces a suitable phase difference between the cavitation volume and local system pressure. This becomes possible due to the mass flow gain. Unfortunately, in the context of oscillation, the pulsation of discharge upstream and downstream of the cavity are quite different. It is not obvious in which manner the mass flow gain has to be assigned to these quantities. Stability calculations for simple system models show that negative mass flow gain tends to effectively destabilize the system if applied to the downstream discharge but not with the upstream discharge [10] which oscillates much less. Maybe for this reason, almost all the studies published between 1985 and 2010 [4-8],[11] were based on the assumption that the mass flow gain is controlled by the downstream discharge Q_2 :

$$(2) \quad Q_2 - Q_1 = dV_C/dt = -d/dt(C_C \cdot p_C + \chi \cdot Q_2)$$

3. BASIC STUDIES

Researchers at Osaka university performed a number of fundamental studies concerned with the effect of cavitation on flow fluctuations in a diffuser. It was shown that instability can arise downstream of a bluff body serving as cavitator, and unsteady 2-phase CFD could reproduce this phenomenon and

shown that the diffuser effect (Fig. 3), linked to downstream discharge, correctly explained the pulsation in this experiment.

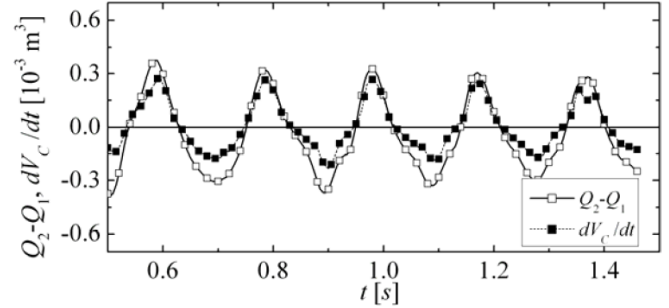


Figure 3 – Simulated instability due to diffuser effect [13]

Tsujimoto, Chen et al. also performed a numerical study [9] concerning the occurrence of self-excited oscillations in a hydraulic system depending on the length of the penstock and the turbine load. This study used estimated parameter values for vortex cavitation. Both the swirl and diffuser effect on cavitation were considered, however, based on strongly simplifying assumptions. It was concluded that instability could occur at partial load as well as at high load (Fig. 4). In this Figure, parameter α is a scale factor for the swirl effect.

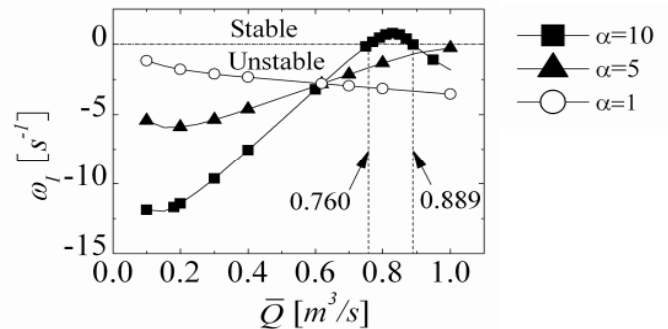


Figure 4 – Stability estimate from [9]

4. FIRST INDUSTRIAL APPLICATIONS

For a number of cases where Francis turbines or pump turbines became hydraulically unstable at high load, the 1D model comprising equation (2) was used to explain the problem. Due to the strongly destabilizing effect of this model, it was indeed always possible to explain the problem. Over many years, this was a only a matter of pure reasoning because no numbers for the mass flow gain effect were available.

Only recently, CFD permitted computation of cavity volumes V_C including its derivatives, C_C and χ , in connection with the runner and draft tube flow in actual machines. Numerical prediction of stability seemed to become possible [8]. However, in the course of practical application of this concept, it was found that instability tended to be over-predicted. Large amounts of damping effects had to be inserted in the models – for instance as ‘viscoelastic effects’ linked with phase transition - in order to comply with actually observed stability limits. It was time to question the convention for modeling the mass flow gain [10].

5. USING 2-PHASE CFD FOR DYNAMIC ANALYSIS

A simulation study [12] was performed for an existing Francis turbine of foreign make with specific speed $n_{QE,opt}=0.129$, exhibiting hydraulic instability at very high load. Within the scope of a commercial project, Andritz received the hydraulic profile and some relevant model test results from external sources. The reduced-scale model has a diameter of 350 mm. To enable comparison with model test results, the simulations were executed in model scale.

Time-dependent simulations based on the 2-phase volume of fluid (VoF) method were performed. The local mixture is described by the volume fractions γ_{vapor} and γ_{water} . The inter-phase mass transfer terms are determined by the Rayleigh-Plesset model and the turbulent scales of fluid motion are modeled by the Menter-SST model. Despite some reported deficiencies to predict local flow features, such as re-entrant jets at cavity closure and detached cavitation, it is trusted to predict a reasonable smoothed phase interface surface at saturation pressure and yield consistent phase continuity balances. Better resolution of flow details may be achieved with models resolving the largest turbulent structures in time and space. However, application of such models is out of scope for the industrial scale problem at hand with computing resources available today.

The finite volume solver ANSYS-CFX 12.1 uses a coupled approach for momentum and pressure equations while a segregated solution strategy is applied to turbulence, cavitation rate and volume fractions. Therefore, tight convergence of the inner coefficient loop iterations is more critical to solve the 2-phase flow for every time step than with comparable single-phase flows.

To maintain the computing times manageable, the flow contour was simplified to a rotationally symmetric shape with the area profile of the real draft tube. Due to the vertical axis of the real machine, the gravity field is also symmetric, and the computational domain was reduced to a narrow meridional slice of 2°; even the slice has still 150.000 hexahedral elements.

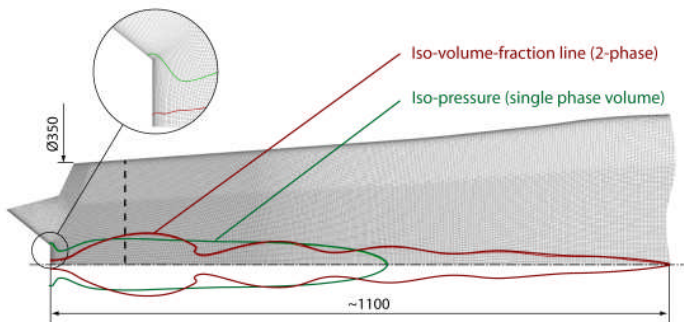


Figure 5 – Mesh grid, 1- and 2-phase results for vortex contour

The steady-state flow pattern for selected points of operation was computed using single-phase as well as two-phase CFD. In single-phase computation, a surface of constant static pressure serves as a proxy for the cavity contour, in two-phase CFD it is defined as the surface of 50% fluid volume fraction. Figure 5 compares the two results. Single-phase computation is clearly not adequate for the purpose. In the real flow, as seen in the model test, the cavity starts with a bubble

attached to the runner hub, terminating in an annular hydraulic jump, and followed by a couple of similar structures. Such typical free surface flow features as standing waves can not be represented by a single phase modeling approach. More important, the cavity volume is also different, resulting in large errors in the predicted parameters (Figure 6).

Operating Point		OP1 -5% Q	OP1	OP1 +5% Q
Cavity Volume V_c/D^3 %	1-phase	2.6	6.4	6.5
	2-phase	1.7	6.9	13.8
Picture of Vortex	1-phase			
	2-phase			

Figure 6 – Steady-state results for mass flow gain estimate

Prior to identifying the dynamic behavior of the draft tube vortex, it was necessary to clarify the requirements for spatial resolution of the CFD mesh and permissible time step. Comparative simulations showed that an extremely small mesh size was necessary.

A strong dependency of the predictions of free oscillation simulations of the time step Δt and number of coefficient loops n_{CL} imposes severe restrictions on these numerical parameters. The inaccuracies occurring with larger time steps with less coefficient loops are evident in a deviation of oscillation frequency and in a systematic deviation from continuity quantified by the ratio δ_{QV} :

$$(3) \quad \frac{dV_{CFD}}{dt} = \delta_{QV}(Q_2 - Q_1) \quad \text{with} \quad V_{CFD} = \int_V \gamma_{vapor} dV$$

By comparative computations with successively reduced time step, the maximum admissible time step was found to be 1ms. With this time step, the continuity index δ_{QV} finally attained 96%. Longer time steps produced large deviations from continuity and also considerable errors in cavitation volume, free oscillation frequency, and the other parameters.

The envisaged model structure had to be slightly more general compared to the older studies on high-load stability. These studies took it for granted the mass flow gain be based on downstream discharge, but we deemed the upstream swirl effect at least equally important, therefore both possibilities had to be accommodated. Like in [10], we allowed the mass flow gain to be distributed between the upstream and downstream discharge, with a fraction $0 \leq \kappa \leq 1$ allotted to draft tube intake discharge.

Concerning the second influence (cavitation compliance C_C), a choice has to be made between a representation by lumped or distributed parameters. For practical reasons, we opted for maintaining compliance a lumped parameter; the cavity volume too is just a single number. Using distributed parameters [11] would consider that the compressibility effect – cavity and some bubbly flow downstream of it – is indeed distributed over a finite length. The distributed equivalent of cavitation compliance would be a lowered wave speed, undergoing important variation along the flow path. As long as this dependency is not known, the computation of higher-order pulsation modes – the only possible benefit of a distributed compliance model – would remain a matter of conjecture. Even with a single compliance parameter, its most suitable location between upstream and downstream parts of the draft tube must also be determined, and expressed by the parameters I_1 and I_2 in equ. 4a and 4c below.

In the time domain, the state variables at the intake (p_1, Q_1) and exit (p_2, Q_2) of the new 1D draft tube model are related as follows:

$$\text{Upstream momentum equation} \\ p_1 - p_c = R_1 \cdot Q_1 + I_1 \cdot dQ_1/dt \quad (4a)$$

$$\text{Cavitation volume} \\ V_c = -C_C \cdot p_c - \chi \cdot (\kappa \cdot Q_1(t-t_d) + (1-\kappa) \cdot Q_2) \quad (4b)$$

$$\text{Downstream momentum equation} \\ p_c - p_2 = R_2 \cdot Q_2 + I_2 \cdot dQ_2/dt \quad (4c)$$

The 2-phase CFD model can be run in transient mode, with constant boundary conditions. If the proper draft tube pressure level is set in a small step, the initial disturbance gives rise to a free oscillation which may be used to identify some of the model parameters. The fact that this is always a damped oscillation already indicates that the main destabilizing effect is upstream and therefore excluded by the boundary condition of prescribed discharge. If the draft tube exit flow would control the mass flow gain, then the simulated oscillation would normally be normally unstable.

The procedure for parameter identification uses the results of the transient simulations. The procedure compares the time series of discharge and pressure in the intake and exit section of the draft tube, and the cavity volume. Fulfillment of two conditions is checked by computing an overall approximation error for the transient cavity volume and for the transient differential pressure. The procedure varies the model parameters and searches for a condition with minimum overall error. It uses the Nelder-Mead algorithm (simplex method) as provided by the *fminsearch* function of MATLAB.

The identification procedure was applied for different sets of assumptions about model structure. First the influence of downstream discharge was completely suppressed ($\kappa=1$). The approximation fitted very well with the unsteady CFD results. Alternative assumptions were then tested in several steps. The downstream share (κ) of mass flow gain was limited and the dead time was cancelled. For several cap values of κ up to 0.9, the best fit was always with the maximum allowed κ (line 2), and the fit clearly improved with higher κ . When the limit on κ was finally removed, the solution converged to a share of mass flow gain ($\kappa-1$) as low as 3-4% allotted to the downstream side, depending on the operating condition. During this process, both C_C and χ attained the values closest to the steady-state results when the best fit was used. For every steady-state condition of operation, several transient cases with different forcing functions were simulated. In the example shown in Figure 7, a harmonic function initiated by a transition ramp with continuous slope was used. In this example, the variation of intake discharge Q_1 was forced at about 50% of the expected natural frequency f_{CC} , and the draft tube exit pressure was kept constant. The effects of cavitation compliance and mass flow gain on the cavity volume were roughly of the same magnitude.

Other runs with 25%, 75% and 125% of f_{CC} were also computed. There was only minor scatter between the parameters resulting from different transient cases.

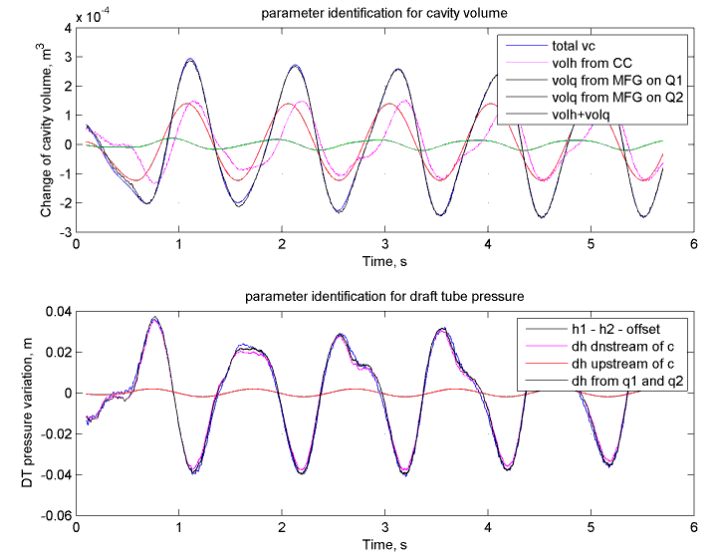


Figure 7 – Quality of fit between CFD and 1D model

In the upper part of Figure 7, the cavity volume V_c computed by CFD (blue curve) is represented as the sum of 3 terms: (1) the contribution from pressure variation via cavitation compliance (pink), (2) the mass flow gain due to delayed upstream effect (red curve), and (3) the mass flow due to downstream effect (green curve). The sum of the 3 terms is shown as a black curve; it fits very well with the blue target curve from CFD. The resulting parameter sets for the various transients simulated over any given steady-state flow differed only slightly. It can be concluded that the 1D model correctly describes the dynamic behavior of the simulated flow.

For the high-load operating point concerned in Figures 5 through 7, the κ ratio resulted as $\kappa=0.96$, in other words, only 4 per cent of the mass flow gain are acting on the downstream

discharge Q_2 . The dead time resulted as $t_d = 73\text{ms}$, compared to the runner period of 119ms , and the free oscillation period of 513ms .

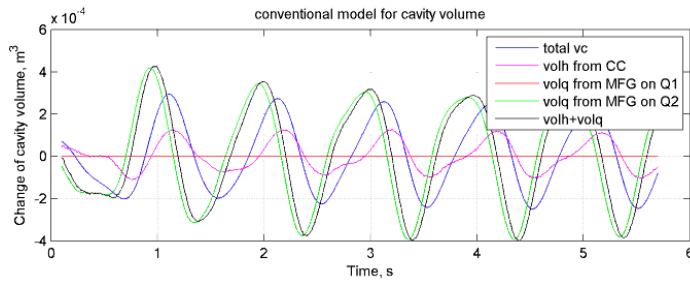


Figure 8 – Quality of fit assuming $\kappa=0$

For demonstration, the older theory using $\kappa=0$ and the C_C and χ parameters from the steady-state simulation, was also used to synthesize the computed dynamic response curves. The result is shown in Figure 8, using the same color code as in Fig. 7. Obviously, the black curve for V_C does not match the blue CFD curve; in particular the phase error is unacceptable for stability assessment.

In the original study [9] based on the downstream mass flow gain factor (diffuser effects) and the upstream mass flow gain (swirl effects), the instability occurs mainly at part load as shown in Fig. 4. However, if we assume the delay time t_d corresponding to a half of the surge period on the swirl effects, it can correctly simulate the full load surge. This was the main motivation to prepare the present joint paper.

6. CONCLUSION AND OUTLOOK

The study described in the previous chapter finally produced a realistic yet fairly simple 1D model structure for the full-load vortex dynamics to be used in the context of a system pulsation. Most of the mass flow gain effect must be assigned to the oscillation of runner exit discharge, and the time lag due to swirl transport on the vortex has to be accounted for. Using considerable simplifications, unsteady 2-phase CFD simulation is quite manageable with regard to computing time.

It was also found that numerical results for the velocity distribution at the interface between runner and draft tube were not well compatible with visual vortex observation in the reduced-scale model test. More accurate assumptions concerning this boundary condition are deemed necessary for reliable prediction of surge behavior. Also, better validation of the computed cavity shape by experiments is desirable. A further research project to thoroughly study the phenomena of high-load surge has therefore been launched. A combination of experimental and numerical research will be jointly conducted by the Laboratory of Hydraulic Machines of the Swiss Polytechnic at Lausanne (EPFL), and Andritz Hydro.

The more fundamental work at the Osaka university will also be continued. As in the earlier studies, both experimental and CFD investigations are foreseen. Again, a smaller-scale apparatus with a straight conical diffuser is being used. The effects of the upstream mass flow gain factor or the swirl effects will be studied focusing on the phase delay, by adding a model runner upstream of the conical diffuser and a straight pipe.

REFERENCES

- [1] Brennen, C.: The unsteady, dynamic characterization of hydraulic systems with emphasis on cavitation and turbomachines, Joint IAHR/ASME/ASCE Symposium, Fort Collins, Colo., June 1978, p. 97-107.
- [2] Purdy, C.C., 1979, Reducing power swings of Tarbela's turbines, Water Power & Dam Construction, April 1979
- [3] Dörfler, P.K.: System dynamics of the Francis Turbine Half Load Surge. IAHR Section Hyd. Machinery, Equipm. & Cavitation, 11th Symp. (Amsterdam, 1982), Vol. 2, Paper 39
- [4] Pülpitel, L., 1985: Low frequency pressure oscillations in hydraulic systems with a pump turbine. Hydro Turbo 85, Paper F10, p. 165-174
- [5] Koutník, J., Pülpitel, L., 1996: Modelling of the Francis turbine full-load surge, Modelling, Testing & Monitoring for Hydro Powerplants - II, Lausanne, July 1996
- [6] Koutník, J., Nicolet, Ch., Schohl, G.A., Avellan, F., 2006: Overload surge event in a pumped storage power plant, IAHR 23rd Symp. on Hydr. Mach. & Systems, Yokohama 2006
- [7] Arzola, F., Azuaje, C., Zambrano, P., Gulbrandsen, G., 2006: Undesired Power Oscillations at High Load in Large Francis Turbines Experimental Study and Solution, IAHR 23rd Symp. on Hydraulic Machinery Systems, Yokohama, Oct. 2006
- [8] F. Flemming, J. Foust, J. Koutník, R.K. Fisher, 2008: Overload surge investigation using CFD data, IAHR 24th Symp. on Hyd. Mach. & Systems, Foz do Iguassú, Oct. 2008
- [9] Tsujimoto, Y., Yonezawa K., and Chen, Ch., 2008, One-dimensional analysis of full load draft tube surge, The 4th International Symposium on Fluid Machinery and Fluid Engineering, November 24-27, 2008, Beijing, China
- [10] Dörfler, P. K., 2009: Evaluating 1D models for vortex-induced pulsation in Francis turbines, Proc. 3rd Meeting IAHR Workgroup on Cavitation and Dynamic Problems in Hydraulic Machinery and Systems, Brno 2009
- [11] Alligné, S., Maruzewski, P., Dinh, T., Wang, B., Fedorov, A., Josfin, J., Avellan, F., 2010, Prediction of a Francis turbine prototype full load instability from investigations on the reduced scale model, IAHR 25th Symp. on Hydraulic Machinery & Systems, Timisoara, Sept. 2010
- [12] Dörfler, P.K., Keller, M. and Braun, O., 2010, Francis full-load surge mechanism identified by unsteady 2-phase CFD, IAHR 25th Symp. on Hydr. Mach. Systems, Timisoara, 2010
- [13] Chen Ch., Nicolet C., Yonezawa K., Farhat M., Avellan F., Miyazawa K., Tsujimoto Y., 2010, Experimental Study and Numerical Simulation of Cavity Oscillation in a Conical Diffuser, IJFMS, Vol. 3(2010), No. 1, pp.80-90.
- [14] Chen Ch., Nicolet C., Yonezawa K., Farhat M., Avellan F., Miyazawa K., Tsujimoto Y., 2010, Experimental Study and Numerical Simulation of Cavity Oscillation in a Conical Diffuser with Swirling Flow, IJFMS, Vol. 3(2010), No. 1, pp.91-101.

Modelling Microbubble Dynamics in Biomedical Applications

Georges L. Chahine* and Chao-Tsung Hsiao
DYNAFLOW, INC.

WWW.DYNAFLOW-INC.COM

*glchahine@dynaflow-inc.com

ABSTRACT

Controlling microbubble dynamics to produce desirable biomedical outcomes when and where necessary and avoid deleterious effects requires advanced knowledge, which can be achieved only through a combination of experimental and numerical/analytical techniques. The present communication presents a multi-physics approach to study the dynamics combining viscous-inviscid effects, liquid and structure dynamics, and multi bubble interaction. While complex numerical tools are developed and used, the study aims at identifying the key parameters influencing the dynamics, which need to be included in simpler models.

1. INTRODUCTION

Microscopic bubbles are ubiquitous in nature and could interact significantly with their environment once excited. Extensive studies have elucidated these effects in diverse fields of application, e.g. ocean acoustics [1], hydrodynamics [2], sound and erosion structure protection [3,4], environmental technologies [5], and medical and biological applications [6,7].

In biological media, either naturally suspended microbubbles or man-made introduced contrast agents, can be activated through ultrasound application or as a result of significant changes in the ambient pressure due to high accelerations (astronauts, jetfighter pilots) or to rapid changes in the depth of submergence (divers, submariners). Application of ultrasound is now a common practice in medicine for both diagnostic and therapeutic use. Main applications include: sonography, Shock Wave Lithotripsy (SWL), tissue ablation, ultrasound mediated drug delivery, wound healing and tissue regeneration. High Intensity Focused Ultrasound (HIFU) is very successful in the treatment of tumors. However, numerous studies have also established that the cavitation activity could result in deleterious bio-effects such as hemolysis and hemorrhage [8-14] resulting from ultrasound- based medical treatments such as SWL or HIFU. SWL can produce acute renal injury, such as hematuria, kidney enlargement, and renal and perirenal hemorrhage and hematomas. SWL-induced injury in the kidney involves primarily vascular lesions, which extend throughout the thickness of the kidney [15]. This vascular injury is characterized by extensive damage of the endothelial cells and rupture of blood vessels, with capillary and small blood vessels being much more susceptible to SWL injury than large vessels [16]. Although experimental studies [17-19] were able to show

that cavitation bubbles are primarily responsible for the damage, the actual mechanism is still not well understood due to the difficulty in conducting experimental observations. Therefore, there is a need to complement difficult experimental observations with advanced computational tools.

Characterization and understanding of the fragmentation mechanism of a contrast agent is pivotal to its use for drug delivery. The ultrasonic fragmentation threshold depends on the initial size, shell thickness, and shell and gas properties [20,21]. Using a high intensity source and a large number of cycles may be applicable to all types and sizes of contrast agent, but cannot be applied safely in a clinical environment. Understanding of the forces involved in the breakup of a particular type of agent is therefore paramount to avoiding expensive and lengthy trial and error experiments, and to minimizing risk to patients. Presently, however, the dynamic mechanisms involved in shell breakup are not well understood. These mechanisms become even more complicated when the contrast agent 'bubble' has a thick shell and interacts with other agents and/or nearby tissues.

Experimental observations [18-19,22-25] have shown that the SWL-induced cavitation bubbles behave very differently *in vivo* than *in vitro*. Because of confinement, cavitation bubbles produced *in vivo* have their expansion significantly constrained and asymmetric and subsequent bubble collapse can be substantially weakened. These observations suggest that to accurately predict numerically cellular and tissue dynamics and potential damage due to cavitation bubbles, a full 3D fluid/structure interaction (FSI) approach is necessary. In addition, tissue surfaces are soft and deformable under stress, and the instantaneous variations in the tissue surface actually impose time dependent boundary conditions which modify the flow field and the bubble dynamics strongly influencing the resulting pressure loading from the bubble dynamics. Importance of including FSI simulation on bubble jetting has been reported by Gracewski et al. [26], which used our axisymmetric bubble dynamics code, 2DYNAPS© [27,28] and coupled it with a simple tube deformation model by Miao et al. [29].

In addition to fluid structure interactions, interaction among many bubbles is known to play an important role [30-32]. By studying interaction of laser-generated tandem microbubbles with rat mammary carcinoma cells, Sankin et al [33] showed that a single bubble did not form a re-entrant jet toward the nearby cell and thus no membrane poration was observed.

However, by introducing a second bubble with appropriate delay time and location, the first bubble was driven to form a re-entrant jet toward the cell, which resulted in a localized and directional membrane poration. This parallels our studies of bubble dynamics where flexible boundaries delay or even reverse reentrant jet formation, while presence of other nearby bubbles could provide an even stronger attractive/repulsive effect to direct the jet toward the boundary [30-32].

In this contribution we present first models to describe the dynamic behavior of 3D encapsulated bubbles with a highly viscous thick shell. We then consider microbubble interaction with nearby responding and deforming bio-materials boundaries.

2. THICK SHELL ENCAPSULATED MICROBUBBLES

The capability of delivering drug to a targeted area makes therapeutic ultrasound contrast agents attractive to chemotherapy drug development since many chemotherapy drugs are toxic to normal tissues. One such application is to suspend the drug within a highly viscous thick liquid shell encapsulating the bubble [34]. The high viscosity stabilizes the microbubble and keeps it inert until it reaches its specific target. It is then excited with an appropriate acoustic amplitude and frequency to get it to break up and release the drugs. The correct selection of the shell properties and thickness and the appropriate ultrasound characteristics renders the contrast agents powerful targeted drug delivery vehicles. Understanding breakup mechanisms is essential to control delivery.

It is known that a collapsing bubble near a boundary forms a re-entrant jet with a direction dependant on the nature of the boundary and an intensity dependant on the standoff distance [35,36]. A similar nonspherical behavior is expected with encapsulated bubbles and is the subject of the present study.

Many studies have been dedicated to developing numerical models for ultrasound contrast agents. They are most often limited to spherical models and follow Church's approach [37]. Using a thin-shell assumption, the constitutive equation of the shell is simplified and incorporated into a generalized Rayleigh-Plesset. The resulting model has been adapted to study encapsulated microbubble dynamics with known shell properties [38- 41]. The assumption of a thin solid shell is reasonable for contrast agents designed for imaging purpose, with a very thin lipid or protein shell on the order of a few nanometers. To study the dynamics and shell breakup of a thick liquid shelled contrast agent Allen *et al.* [42,43] extended the *spherical* model to include a thick liquid shell.

2.1. 3D Model Domain Decomposition

To investigate the dynamic mechanisms which cause encapsulated bubble shell nonspherical breakup, we have developed a 3-D finite-thickness shell model which couples a Navier-Stokes solver, 3DYNAPS-Vis[®], which uses a finite volume scheme and a potential flow solver, 3DYNAPS-BEM[®], which uses a Boundary Element Method (BEM) [44]. The code enables modeling of inter bubble and boundary interactions. The computational domain is subdivided into inner domains constituted of each microbubble thick viscous shell layer and an outer domain composed of the liquid hosting the shelled microbubbles (see Figure 1). In the inner domains we solve the Navier-Stokes equations to best describe the dynamics of the

highly viscous liquid shells. In the outer domain we use the Boundary Element Method. The main advantage of using the BEM is its unique ability to provide a complete solution in terms of boundary values without need to discretize the whole computational domain. This reduces the dimensions of the problem by one, allows the model to work on complicated boundary geometries, and addresses non-spherical deformations. The outer domain includes any nearby walls or free surfaces. The two solvers communicate with each other by exchanging the values of the flow variables at the shell-liquid interfaces.

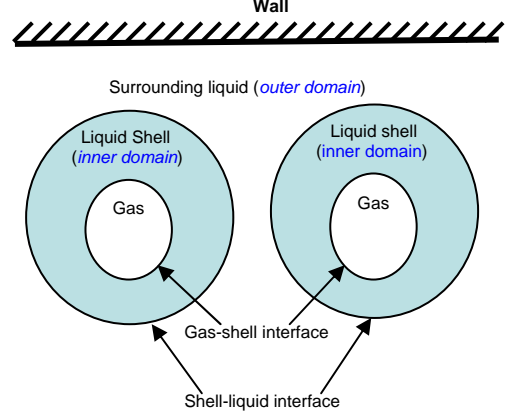


Figure 1. Sketch for illustration of the thick shell bubble problem with domain decomposition.

2.2. Outer Domain Liquid Problem

The outer domain liquid flow due to the contrast agent's motion is assumed to be irrotational and incompressible. These are conventional assumptions for bubble dynamics and allow the definition of a potential, ϕ , for the velocity \mathbf{u} ,

$$\mathbf{u} = \nabla \phi, \quad \nabla^2 \phi = 0, \quad (1)$$

A boundary integral method is used to solve (1) using Green's formula, where \mathbf{x} is a fixed point in the 'outer' liquid domain and \mathbf{y} is a point on the boundary surface S comprising all inner domains and any other boundaries,

$$\Omega \phi(\mathbf{x}) = \int_S \mathbf{n}_y \cdot \left[\nabla \phi(\mathbf{y}) \frac{1}{|\mathbf{x} - \mathbf{y}|} - \phi(\mathbf{y}) \nabla \left(\frac{1}{|\mathbf{x} - \mathbf{y}|} \right) \right] dS. \quad (2)$$

Ω is the solid angle under which point \mathbf{x} sees the liquid domain.

This equation states that if the velocity potential ϕ and its normal derivatives are known on the boundary surface S of the liquid domain, where ϕ satisfies the Laplace equation, then ϕ can be determined anywhere by integration over the boundary surface. This reduces by one the dimension of the problem of solving the Laplace equation.

2.3. Inner Domain Shell Model

To solve the viscous flow in the inner domains, the unsteady Navier-Stokes equations are used. The continuity and momentum equations in non-dimensional form can be written:

$$\frac{\partial u_i}{\partial x_i} = 0, \quad \frac{\partial u_i}{\partial t} + u_j \frac{\partial u_i}{\partial x_j} = -\frac{\partial p}{\partial x_i} + \frac{1}{R_e} \frac{\partial \tau_{ij}}{\partial x_j}, \quad (3)$$

where u_i are the Cartesian components of the velocity, x_i are the Cartesian coordinates, and p is the pressure. $R_e = \rho_s^* u^* L^* / \mu_s^*$ is the Reynolds number of the viscous shell, u^* and L^* are the

characteristic velocity and length, ρ_s^* is the shell density, and μ_s^* is its dynamic viscosity.

The effective stress tensor τ_{ij} is given by:

$$\tau_{ij} = \left[\left(\frac{\partial u_i}{\partial x_j} + \frac{\partial u_j}{\partial x_i} \right) - \frac{2}{3} \delta_{ij} \frac{\partial u_k}{\partial x_k} \right], \quad (4)$$

where δ_{ij} is the Kronecker delta. The flow field in the *inner domain* is directly simulated using (3) without any turbulence model because the Reynolds number is very small and the flow is laminar for all cases studied.

In order to simplify the treatment of the boundary conditions for complex geometries, (3) is expressed into a general time-dependent body-fitted curvilinear coordinate system (ξ, η, ζ) . The time dependent nature of this transformation allows all computations to be carried out in a fixed uniform computational domain even though components of the physical domain may be in motion. This provides a computational domain that is better for applying spatial differencing and the boundary conditions.

2.4. Boundary Conditions

2.4.1. Shell-gas interface

Kinematic and dynamic boundary conditions are applied at the gas-liquid interfaces. The kinematic conditions ensure that a particle on any surface remains on that surface. This can be written $DF/Dt = 0$, with $F(x_i, t) = 0$ being the equation of the considered surface. The dynamic conditions at $\zeta=0$ (gas-shell interfaces) impose zero shear stresses and balance of normal stresses at the interfaces

$$\left. \frac{\partial U}{\partial \zeta} \right|_{\zeta=0} = 0, \quad \left. \frac{\partial V}{\partial \zeta} \right|_{\zeta=0} = 0, \quad p = p_{gv} + \frac{2}{R_e} \left. \frac{\partial W}{\partial \zeta} \right|_{\zeta=0} - \frac{\mathcal{C}_{gs}}{W_{e,gs}}, \quad (5)$$

where (U, V, W) are contravariant velocity components in the curvilinear coordinates and \mathcal{C}_{gs} is the local curvature at the interface. For each microbubble the Weber number and the normalized gas content pressure are given by:

$$W_{e,gs} = \rho_s^* u^{*2} L^* / \gamma_{gs}^*, \quad (6)$$

$$p_{gv} = (p_g^* + p_v^* - p_\infty^*) / \rho_s^* u^{*2},$$

where γ_{gs}^* is the surface tension at the gas-shell interface and p_g^*, p_v^* , and p_∞^* are the dimensional gas and vapor partial pressures inside the bubble and the amplitude of the imposed driving pressure far from the bubble. To determine the gas pressure we assume that the amount of gas inside the bubble remains constant and that the gas satisfies the polytropic relation:

$$p_g \mathcal{V}^{*k} = \text{constant}, \quad (7)$$

where \mathcal{V}^* is the gas volume and k is a gas compression constant.

2.4.2. Shell-liquid interface

The shell-liquid interface is a liquid-liquid interface at which the boundary conditions are: continuity of the shear stresses, balance of the normal stresses, and continuity of the velocities. These can be written in non-dimensional format as:

$$\left. \frac{\partial U}{\partial \zeta} \right|_{\zeta=1} = \frac{\mu_l}{\mu_s} \tau_{l,\xi}, \quad \left. \frac{\partial V}{\partial \zeta} \right|_{\zeta=1} = \frac{\mu_l}{\mu_s} \tau_{l,\eta},$$

$$p - \frac{2}{R_{e,s}} \left. \frac{\partial W}{\partial \zeta} \right|_{\zeta=1} = P_l - \frac{1}{R_{e,s}} \frac{\mu_l}{\mu_s} \tau_{l,\zeta} + \frac{\mathcal{C}_{sl}}{W_{e,sl}}, \quad (8)$$

$$W|_{\zeta=1} = \mathbf{u}_s \cdot \mathbf{n}.$$

In the above expressions, μ_l and μ_s are the dynamic viscosities of the host liquid and the shell liquid and \mathcal{C}_{sl} is the normalized curvature of the shell-liquid interface, and γ_{sl}^* is the surface tension at the shell-liquid interface,

$$W_{e,sl} = \rho_s^* u^{*2} L^* / \gamma_{sl}^*. \quad (9)$$

\mathbf{n} and \mathbf{u}_s are respectively the local unit normal and the shell liquid velocity at the boundary. \mathbf{u}_s is provided by the solution of the outer domain. $\tau_{l,\xi}, \tau_{l,\eta}$ are the normal derivatives of the host liquid tangential velocity components in the ξ and η directions. $\tau_{l,\zeta}$ is the derivative along the normal of the normal velocity component, and P_l is the pressure in the host liquid.

2.4.3. Other boundaries

At rigid boundaries no flow across the boundary is enforced. For a rigid and stationary body surface this can be written as:

$$\frac{\partial \phi}{\partial n} = 0, \quad (10)$$

and for a moving/deforming boundary:

$$\frac{\partial \phi}{\partial n} = u_n. \quad (11)$$

At any given time step, if the velocity potential ϕ on the boundary surface S is known, the normal velocity $\partial \phi / \partial n$ can be obtained from Equation (2). For a point \mathbf{x} on the boundary, the pressure, $P_l(\mathbf{x})$, is provided by the Bernoulli equation:

$$P_l(\mathbf{x}) + \rho_l \left[\frac{\partial \phi}{\partial t} + \frac{1}{2} \nabla \phi \cdot \nabla \phi \right] = P(t), \quad (12)$$

where $P(t, \mathbf{x})$ is the imposed ultrasound pressure at the particular bubble location, \mathbf{x} . Once P_l is determined, Equation (12) can provides $\partial \phi / \partial t$. Then, the rate of change of ϕ at a given point \mathbf{x} followed in its motion can be obtained by

$$\frac{D\phi}{Dt} = \frac{\partial \phi}{\partial t} + \mathbf{u}_s \cdot \nabla \phi, \quad (13)$$

where \mathbf{u}_s is the velocity at \mathbf{x} , at the shell-liquid interface.

3. ZERO-THICKNESS SHELL MODEL

3.1. Spherical Model

In Equation (12) P_l can be determined by considering the normal stress balance across the liquid/shell interface computed in the inner domain. Great CPU advantages can be gained if the inner problems could be replaced by an equivalent zero-thickness thin shell with properties reproducing the real finite thickness shell behavior. To do this the stresses exerted by the liquid on the encapsulated bubble have to be properly captured. For the study of microbubble rupture by acoustic excitation the normal stresses are predominant and can be expressed through the normal stress boundary condition across the liquid/shell/gas interface. To do this, let's consider the dynamics of a *spherical*

thick shell microbubble with inner and outer shell radii, R_l and R_2 , respectively. The continuity equation and incompressibility of the shell material and host liquid fluid leads to:

$$u_r = \frac{\dot{R}_l R_l^2}{r^2} = \frac{\dot{R}_2 R_2^2}{r^2}, \quad \dot{R}_l = \dot{R}_2 \frac{R_2^2}{R_l^2}, \quad (14)$$

where u_r is the radial velocity. This provides a direct relationship between R_l and R_2 , the inner and outer radius of the shell.

Applying the momentum equations to both the inner and outer domain problem with the boundary equations described above leads to a non-dimensional Rayleigh-Plesset-like differential equation for R_2 , which describes the time variation of R_2 -- and thus R_l too because of (14)-- which has the following non-dimensional expression [42,47]:

$$R_2 \ddot{R}_2 \left((1 - \rho_s) + \rho_s \frac{R_2}{R_l} \right) + (1 - \rho_s) \frac{3}{2} \dot{R}_2^2 + \rho_s \dot{R}_2^2 \left(\frac{2R_2}{R_l} - \frac{1}{2} \left(\frac{R_2}{R_l} \right)^4 \right) \\ = p_v + p_g - P_\infty - \left(\frac{2}{W_{e,gs} R_l} + \frac{2}{W_{e,sl} R_2} \right) - 4 \frac{\dot{R}_2}{R_2} \left(\frac{1}{R_{e,l}} + \frac{1}{R_{e,s}} \left(\frac{R_2}{R_l} \right)^3 - 1 \right), \quad (15)$$

where $\rho_s = \rho_s^* / \rho_l^*$ and $R_{e,l} = \rho_l^* u^* L^* / \mu_l^*$. The characteristic length L^* is chosen to be the initial outer radius R_{20}^* and the characteristic velocity is $u^* = R_{20}^* / T^*$. T^* is the selected characteristic time and is the smallest of the period of the imposed acoustic waves or the bubble Rayleigh period based on ΔP the amplitude of the imposed acoustic waves:

$$T^* = \min \left[f^{-1}, \quad R_{20}^* (\rho_l^* / \Delta P)^{1/2} \right]. \quad (16)$$

In the case of a highly viscous liquid shell of thickness, d , which tends towards zero, we have:

$$R \approx R_2 \approx R_l, \quad \frac{d}{R_2} = \frac{R_2 - R_l}{R_2} \ll 1, \\ \frac{R_2}{R_l} = \frac{R_2}{R_2 - d} \approx 1, \quad \frac{1}{R_{e,s}} \gg \frac{1}{R_{e,l}}, \quad (17)$$

and Equation (15) becomes:

$$R \ddot{R} + \frac{3}{2} \dot{R}^2 = p_v + p_g - P_\infty - \frac{2}{R} \left(\frac{1}{W_{e,gs}} + \frac{1}{W_{e,sl}} \right) \\ - 4 \frac{\dot{R}}{R} \frac{1}{R_{e,l}} - 12 \frac{d}{R_{e,s}} \frac{\dot{R}}{R^2}, \quad (18)$$

If we ignore in the thin-shell model the layer thickness variations, d can be replaced by its initial value d_0 , and we can define an equivalent Weber number, W_e , a dilatational parameter, κ^s , and a simplified thin-shell differential equation:

$$R \ddot{R} + \frac{3}{2} \dot{R}^2 = p_v + p_g - P_\infty - \frac{2}{R} \frac{1}{W_e} - 4 \frac{\dot{R}}{R} \left(\frac{1}{R_{e,l}} - \frac{\kappa^s}{R} \right). \quad (19)$$

$$1/W_e = 1/W_{e,gs} + 1/W_{e,sl}, \quad \kappa^s = 3d_0/R_{e,s}$$

In dimensional form the dilatational coefficient is given by

$$\kappa^{s*} = 3d_0 \mu_s. \quad (20)$$

3.2. 3D Nonspherical Model

This same concept can be applied to develop a 3D zero-thickness shell model. In this model, the dynamics boundary condition at the contrast agent/liquid interface is obtained by analogy with the spherical zero-thickness model, through balancing the pressure in the liquid at the interface with the partial gas and vapor pressures, an *equivalent* surface tension, and *equivalent* viscous and dilatational normal stresses:

$$P_l = p_g + p_v - \frac{2}{W_e} \frac{1}{R} - 4 \frac{\dot{R}}{R} \left(\frac{1}{R_{e,l}} - \frac{\kappa^s}{R} \right). \quad (21)$$

To adapt (21) to a 3-D *equivalent* zero-thickness model, the boundary condition at the microbubble liquid interface (5) is modified such that, as in the spherical bubble case, the Weber number and the curvature between the gas and the shell liquid are replaced by an equivalent Weber number and an equivalent curvature respectively, i.e.

$$W_{e2} \rightarrow \text{is replaced by} \rightarrow W_e \\ \mathcal{C}_{gs} \rightarrow \text{is replaced by} \rightarrow \mathcal{C} \quad (22)$$

Similarly the simple viscous normal stress term is replaced, by analogy to the spherical case, by an equivalent term that accounts for both the viscosity of the bulk liquid the viscosity of the shell material and the thickness of the material:

$$\frac{2}{R_e} \frac{\partial W}{\partial \zeta} \Big|_{\zeta=0} \rightarrow 2\dot{R}\mathcal{C} \left(\frac{1}{R_{e,l}} - \frac{\mathcal{C}\kappa^s}{2} \right) \quad (23)$$

As a result, the normal stress boundary condition is written as:

$$P_l = p_v + p_g - \frac{\mathcal{C}}{W_e} - \mathcal{C} \left(\frac{2}{R_{e,l}} - \frac{\kappa^s}{2} \right) \frac{\partial \phi}{\partial n}. \quad (24)$$

In the equivalent zero-thickness model, as expressed in(17), the inner and outer bubble shell radii become the same, and we chose here the outer radius, R_{20}^* , as the equivalent microbubble radius to track and use for the computations.

4. FINITE ELEMENT STRUCTURE MODEL

To simulate the interaction between the encapsulated bubbles and deformable tissues, we couple the fluid solvers with a structure dynamics solver. With σ being the Cauchy stress tensor, the structure motion equations are:

$$\rho \frac{d\mathbf{u}}{dt} = \rho \mathbf{g} + \nabla \cdot \sigma, \quad (25)$$

If we denote \mathbf{F} the deformation gradient tensor, then the Cauchy stress tensor is:

$$\sigma = \det(\mathbf{F}) \mathbf{F} \mathbf{S} \mathbf{F}^T, \quad (26)$$

where \mathbf{S} is the second Piola-Kirchoff stress tensor:

$$S_{ij} = 2 \frac{\partial W}{\partial C_{ij}}. \quad (27)$$

The Cauchy deformation tensor is $C_{ij} = F_{ki} F_{kj}$, and W is the strain energy function which can be modeled differently according to the types of tissues [48,49]:

The boundary condition at the surface of the tissue with the pressure provided by the BEM solution is:

$$\mathbf{n} \cdot \sigma \cdot \mathbf{n} = P. \quad (28)$$

The motion of the tissue in response to the fluid pressures is simulated using finite elements. This provides the new position of the structure and the normal velocities at the surface (or $\partial\phi/\partial n$) needed for the BEM procedure, and allows the solution to proceed in time.

5. NUMERICAL METHODS

5.1. Potential Flow Solver

To solve Equation (2) numerically with the boundary element method, we discretize the surfaces of all objects into triangular panels. The surface integrals become a summation over all panels of the influence of singularity distributions over each individual panel. It is necessary to assume a relation between ϕ and $\partial\phi/\partial n$ at a surface node with the values of these quantities at the discretized nodes. Here, we assume that these quantities vary linearly over a panel with the values determined by the values at the surrounding nodes. Equation (2) can then be expressed in a matrix form as:

$$\bar{\mathbf{B}} \frac{\partial\phi}{\partial n} = (a\pi\mathbf{I} + \bar{\mathbf{A}})\phi, \quad (29)$$

where \mathbf{I} is an $N \times N$ identity matrix, and $\bar{\mathbf{A}}$ and $\bar{\mathbf{B}}$ are $N \times N$ influence coefficient matrices. With ϕ known on all boundary nodes, (29) is a linear system of N equations and can be readily solved for N unknowns of $\partial\phi/\partial n$, using classical methods such as LU decomposition and Gauss elimination.

5.2. Viscous Navier-Stokes Flow Solver

To solve Equations (3), 3DYNAPS-VIS[®] uses a finite volume formulation and the artificial-compressibility method [50], in which a time derivative of the pressure is added to the continuity equation with β an artificial compressibility factor:

$$\frac{1}{\beta} \frac{\partial p}{\partial t} + \frac{\partial u_i}{\partial x_i} = 0. \quad (30)$$

The solution procedure is then to march in pseudo-time until continuity is satisfied. To obtain a time-dependent solution, a Newton iterative procedure is performed at each physical time step. First-order Euler implicit difference formula are applied to the time derivatives. The spatial differencing uses a flux-difference splitting scheme based on Roe's method [51] and van Leer's MUSCL method [52] for obtaining the first-order and the third-order fluxes respectively. A second-order central differencing is used for the viscous terms. The flux Jacobians required in an implicit scheme are obtained numerically. The resulting system of algebraic equations is solved using the Discretized Newton Relaxation method [53] in which symmetric block Gauss-Seidel sub-iterations are performed before the solution is updated at each Newton iteration.

5.3. Coupling the two Liquids and a Deformable Structure

The boundary conditions given in Section 2.4.2 are key for coupling the Navier-Stokes solver and the potential flow solver. The procedure, illustrated in Figure 2, is summarized as follows:

- Volume grids are generated for the inner domains, and surface grids are generated for the outer host liquid domain.
- The Navier-Stokes equations are solved for the viscous liquid in the shells with the shell-liquid interfaces normal velocities provided by the host liquid potential solver.

- Shell interfaces are updated with the kinematic boundary conditions and the boundary pressures are calculated.
- Green's equation is solved to provide the velocity potential at the shell/liquid interface.
- Structure dynamics equations are solved using computed liquid pressures. This provides new normal velocities and positions, then the procedure is repeated as time evolves.

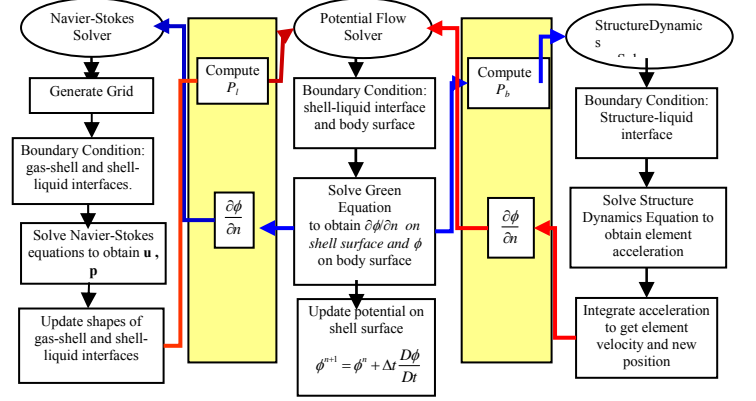


Figure 2. Flow chart of the numerical procedure for coupling the Navier-Stokes, potential flow, and structure dynamics solvers.

6. EXAMPLE APPLICATIONS

6.1. Encapsulated Bubble Dynamics Near Rigid Wall

The results and computations in this study focus on oil-shelled microbubbles developed for drug delivery, e.g. triacetin shell (ImaRx Therapeutics). We consider triacetin-shelled bubble in water. Triacetin has a density: 1,100 kg/m³, viscosity: 0.028 kg/ms, surface tension at gas-triacetin interface: 0.008 kg/s², surface tension at triacetin-water interface: 0.006 kg/s². Unless specified otherwise, we consider the initial bubble radii $R_{10} = 1.2\mu\text{m}$, $R_{20} = 1.7\mu\text{m}$ for all the results shown below.

6.1.1. Finite-Thickness Shell Model

The non-spherical deformations due to the presence of the wall become much more significant as the driving pressure amplitude becomes higher. To study the effect of a rigid wall on contrast agent dynamics, we present below 3-D numerical simulations for an acoustically driven contrast agent near a rigid wall at two initial standoffs, $X = 2.6$, and $4.6\mu\text{m}$.

Figure 3 and Figure 4 show the encapsulated bubble shape time variations during the first oscillation period. Also shown are the pressure contours in the viscous liquid of the shell. All shapes are shown in a cut plane perpendicular to the wall going through the bubble center. The shelled bubble is initially in a uniform pressure field with of 0.1Mpa, and is subjected to a sinusoidal acoustic wave with $P_a = 1\text{Mpa}$ and $f = 2.5\text{MHz}$. As expected, the smaller standoff case results in more significant non-spherical deformations. The presence of the wall imparts a non-spherical pressure distribution on the shell which deforms. More importantly the dynamics lead to a non-uniform shell liquid thickness distribution during the oscillations. During the bubble growth phase, the shell retains a more or less uniform thickness, then becomes thicker and thicker on the side opposite to the wall, where a jet usually takes place. Concurrently, the

shell becomes thinner and thinner at the side nearest to the wall potentially leading to starvation of the shell liquid and breakup.

Using a linear stability analysis [47], we have also confirmed that the most unstable mode due to a 3-D perturbation is when the bubble starts a jet at one end and breaks up through thinning at the other end.

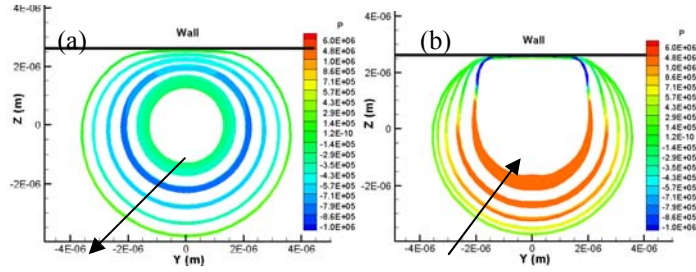


Figure 3. Encapsulated microbubble shape variations and pressure contours near a rigid wall when subjected to a sinusoidal acoustic wave with $P_a=1\text{Mpa}$, $P_{atm}=0.1\text{Mpa}$ and $f=2.5\text{MHz}$. (a) Bubble growth. (b) Bubble collapse with $R_{10}=1.2\mu\text{m}$, $R_{20}=1.7\mu\text{m}$. Initial standoff of $2.6\mu\text{m}$.

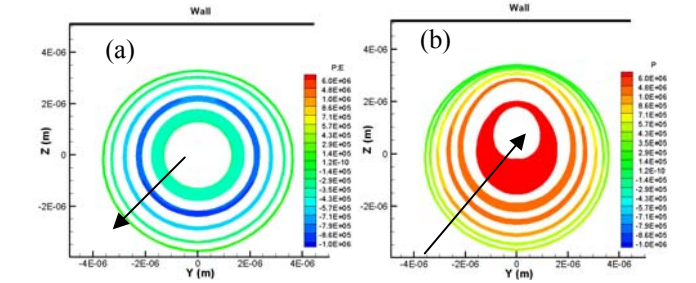


Figure 4. Encapsulated microbubble shape variations and pressure contours near a rigid wall when subjected to a sinusoidal acoustic wave with $P_a=1\text{Mpa}$, $P_{atm}=0.1\text{Mpa}$ and $f=2.5\text{MHz}$. (a) Bubble growth. (b) Bubble collapse with $R_{10}=1.2\mu\text{m}$, $R_{20}=1.7\mu\text{m}$. Initial standoff of $4.6\mu\text{m}$.

Figure 5 and Figure 6 show the encapsulated microbubble shape variations and normal velocity contours at three time steps as seen in the outer domain. (Two bubbles are shown to represent the rigid wall.) In the figures, the second set is at the time the microbubble attains its maximum size, while the third set is the last time step before the simulations were terminated for the $X=2.6$ case and the last time step before the rebound for the $X=4.6\mu\text{m}$ case.

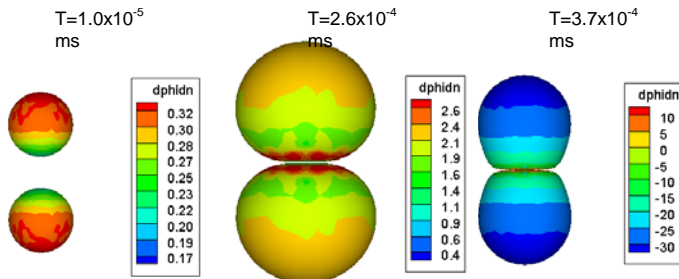


Figure 5. Encapsulated microbubble shape variations and normal velocity 3D contours at three times as seen in the outer domain. Conditions of Figure 3.

Figure 7 shows a comparison of the time history of the microbubble equivalent radius for three standoff cases. It is seen that the presence of the wall only has a slight influence on the maximum growth size of the bubble. The simulations for the 2.6 and $3.6\mu\text{m}$ cases were terminated due to numerical instability as the shell became extremely thin and the 3D grid became overly squeezed, while the simulation for the $X=4.6\mu\text{m}$ case was able to continue and the rebound was observed.

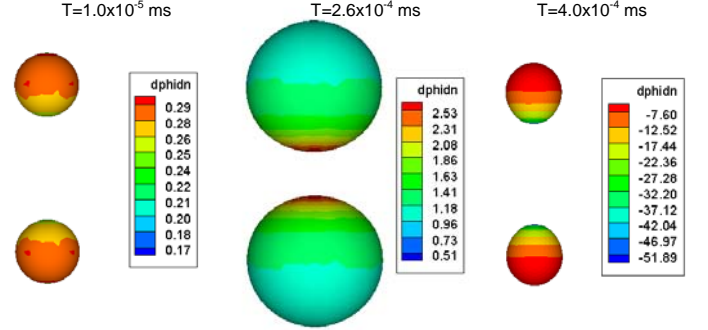


Figure 6. Encapsulated microbubble shape variations and normal velocity contours at three time steps as seen in the outer domain. Conditions of Figure 5.

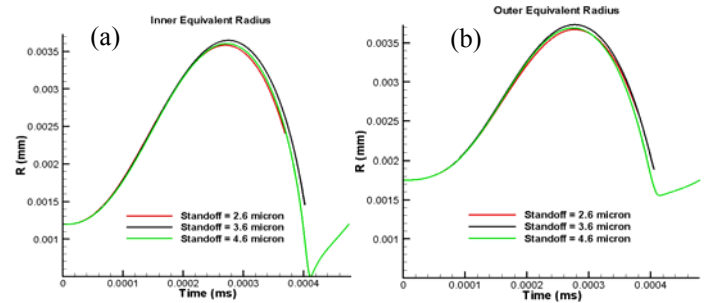


Figure 7. Encapsulated microbubble equivalent radius versus time for three different standoff cases; (a) inner equivalent radius vs. time, and (b) outer equivalent radius vs. time.

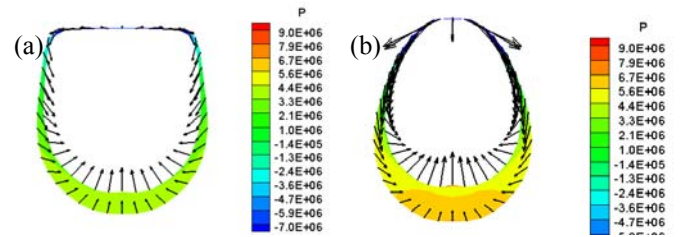


Figure 8. Encapsulated microbubble shape near a wall at the last time step before the simulations were terminated for (a) $X=2.6$, and (b) $X=3.6\mu\text{m}$. The velocity vectors are shown plotted on both the shell/liquid and the shell/gas interfaces.

Figure 8 shows more solution details with the velocity vectors plotted on both shell/liquid and shell/gas interfaces at the last time step before the simulations were terminated for the $X=2.6$ and $X=3.6\mu\text{m}$ cases. Figure 9 shows the solutions at the time steps before and after the rebound for the $X=4.6\mu\text{m}$ case. A re-entrant jet with a high normal velocity is seen for the 2.6 and $3.6\mu\text{m}$ cases just starting to form at the thick-shell side

away from the wall. At the thin-shell side, close to the wall, the shell is seen stretching with high tangential velocities pulling the shell apart. Continuous shell thinning and stretching at the near-wall side indicate the tendency of the shell to break up there. For the $X=4.6 \mu\text{m}$ case, the shell remained thick everywhere and was not stretched near the wall side. As a result the microbubble was able to rebound after reaching its minimum volume.

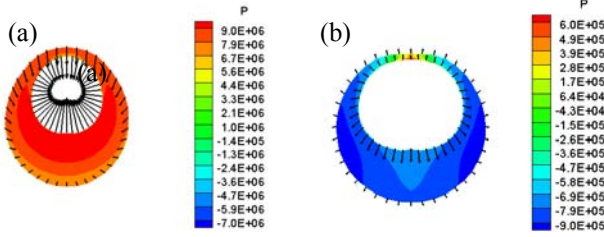


Figure 9. Encapsulated microbubble shape near a wall right before and after rebound for the $X=4.6 \mu\text{m}$ case. The velocity vectors are shown plotted on both the shell/liquid and the shell/gas interfaces.

6.1.2. Shell Thickness and Standoff Effects on Shell Break-up

It has been shown that an explosion bubble may become pinched off into an hourglass shape and cut into two instead of forming a re-entrant jet during its collapse, depending on its initial distance above a cylindrical or flat boundary [55]. For the current problem, other parameters such as shell thickness, shell material, initial bubble radius, acoustic pressure amplitude, and frequency may also influence the type of bubble breakup. To focus only on the effect of stand-off and shell thickness on the shell breakup a series of simulations for a triacetin-shelled bubble with an initial mid-thickness radius of $1.45 \mu\text{m}$ under ultrasound acoustic excitation with $P_a=1 \text{ Mpa}$, and $f=2.5 \text{ MHz}$ were conducted. The simulations for each case were continued for more than one oscillation cycle unless breakup occurs earlier.

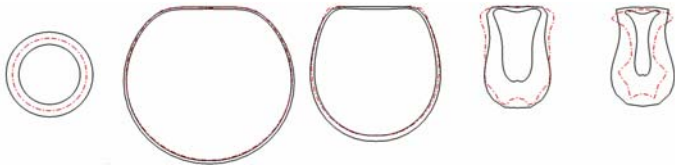


Figure 10. Comparison of the bubble shape variations between the 3D finite-thickness model and the zero-thickness shell model at several time steps during the first bubble oscillation cycle.

Figure 11 shows a diagram of the bubble shapes at the end of the first bubble oscillation cycle. We can subdivide the diagram into four zones. In Zone A, a classical re-entrant jet is formed. In Zone B, a ring type jet is formed. In Zone C, the bubble is found to pinch off into two. In Zone D, the bubble survives and the surface does not become multi-connected during the first cycle. Based on this diagram, the bubble break-up in Zones A and B could be the best conditions for drug or gene delivery. This is because the break-up of the bubble in the first cycle allows lower ultrasound doses and the re-entrant jet can help drug or gene particles penetrate the cell membrane. Although the bubble also breaks up due to pinch-off in Zone C within the first cycle, there is no vectoring jet to enhance sonoporation.

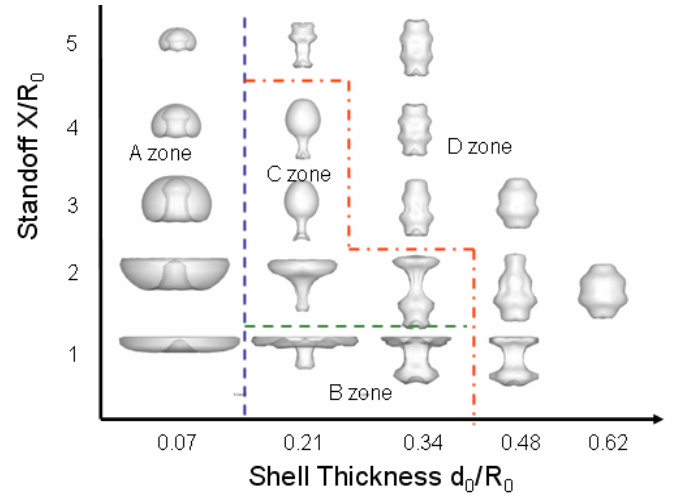


Figure 11. Diagram of bubble shapes for different shell thicknesses and standoffs.

6.2. Tandem Bubbles between Two Parallel Plates.

The models presented above were applied for the simulation of the studies conducted by Zhong's group [24,25,33]. In the model the 3D interaction between two bubbles confined between two parallel disks $50 \mu\text{m}$ apart is considered. The liquid density is $\rho=10^3 \text{ kg/m}^3$, the kinematic viscosity is $\gamma=10^{-6} \text{ m}^2/\text{s}$, the ambient pressure is $p_{\text{amb}}=101235 \text{ Pa}$, the vapor pressure is $p_v=2300 \text{ Pa}$, and the max bubble radius $R_{\text{max}}=25 \mu\text{m}$. The radius of the considered disk is 1 mm . Actually, the radius of the disk, even though much larger than the maximum bubble size, is quite important as we will show later.

In Figure 12 a top view of the dynamics of in-phase tandem bubbles is shown. The bubbles are generated simultaneously. During collapse, re-entrant jets develop in opposite directions. It is seen that 3DynaFS© reproduces quite well the observations.

Figure 13 shows an out-of-phase tandem bubbles case. The second bubble is generated with a $2 \mu\text{s}$ delay after the initiation of the first bubble. It expands, causing the jet forming in the first bubble to speed up to a much faster speed. This is used to produce poration of nearby single cells [24,25,33]. Here again, it is seen that 3DynaFS© reproduces well the observations.

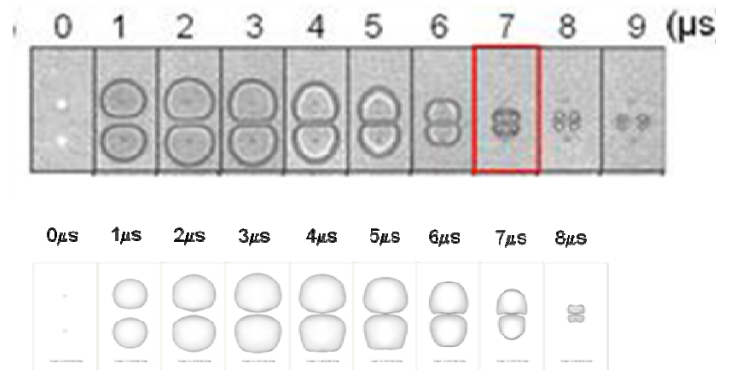


Figure 12. In-phase tandem bubbles dynamics, top view, and comparison with experiment

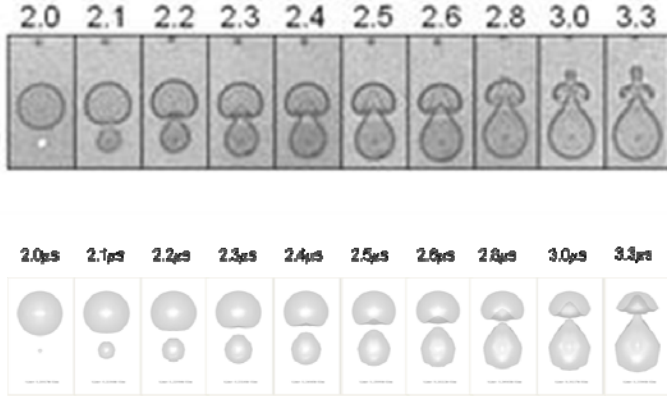


Figure 13 Out-of-phase tandem bubble dynamics, top view, and comparison with experiment of Zhong et al [24,25,33].

The bubbles in this problem actually transition from a 3D shape to a quasi cylindrical shape during the dynamics as the spacing between the plates could be smaller than the maximum bubble radius. This imposes strong constraints on the gridding of the bubbles and the plates that the code can solve. A more important issue is that of the size of the confinement domain. In both the experimental and numerical configurations, because of the confinement, it is very important to know where the “ambient” or “reference” pressure is imposed. Assuming the bubble dynamics occurs in channels or in between disk plates and that the pressure is imposed at the edges of these channels of disks, the sizes of the confined space have a strong influence on the bubble dynamics. For example, Figure 14 shows the dynamics (equivalent radius vs. time) of a confined bubble between two disk plates, when everything is kept the same but the diameter of the disks. The figure shows both 3DYNFS results as well as the Navy compressible code, Gemini, results [54]. This is to remove arguments made that this is a compressibility effects. The reason for the behavior is purely dynamics and is directly connected to the inertia of the liquid in the confined region, which changes with the size. Thus, one has to be very careful in identifying where the reference pressure is imposed for fine experiments or simulations involving such conditions.

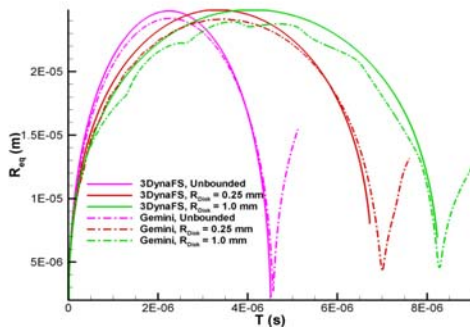


Figure 14. Effect of the disk size on dynamics bubble between two rigid plates at a gap of 50 μm for $R_0=2\mu\text{m}$, $R_{\text{max}}=50\mu\text{m}$, $P_{\text{amb}}=1 \text{ atm}$. Incompressible and compressible solutions. Notice that in all cases the diameter of the disk is very large compared to the bubble size and to the size of the gap between disks.

6.3. Bubble Dynamics Near Deformable Bio-Materials

The interaction of a collapsing bubble with a nearby tissue is complex and has received a lot of attention by the research community because of the potential for tissue or vessel damage [e.g.19,24,25,33,56,57]. The tissue significantly deforms during the bubble dynamics and observations indicate potential occurrence of both poration [33] and invagination [19] depending on the experimental configuration. In this section, we investigate modeling the tissue as an elastic material and we compute its dynamics using a structure code. The process is simulated with the BEM/FEM coupling method described above. We illustrate this with the interaction between a flat thick tissue block and a bubble initially at equilibrium before a sinusoidal acoustic pressure is applied. The acoustic pressure starts with a negative half cycle so that the bubble initially grows and then collapses near the tissue. Figure 15 shows the geometric set-up where the tissue is modeled as a large and thick rectangular plate. In the simulations, the bottom of the plate is held rigid. To better resolve the dynamics near the bubble, the grid size is locally refined. The dynamics are related to the initial bubble size R_0 , initial standoff distance X to the tissue, the material properties such as the density ρ_{tissue} , elasticity modulus E , and the frequency f and amplitude P_a of the acoustic pressure. The elastic modulus of bio-materials varies in a very wide range (see e.g. [57]). Since the elasticity is a crucial parameter for this problem, we show the results for three elastic moduli: $E = 10\text{kPa}$, 100kPa and 1000kPa .

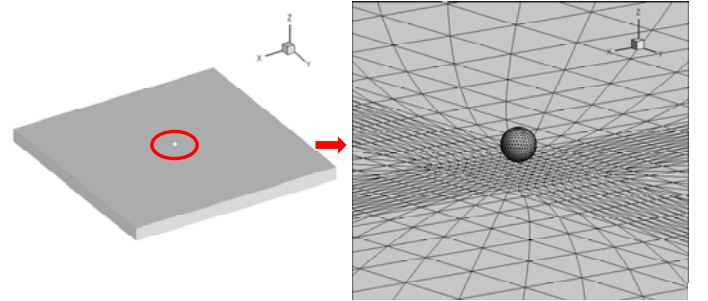


Figure 15. Geometry of the problem and the grid.

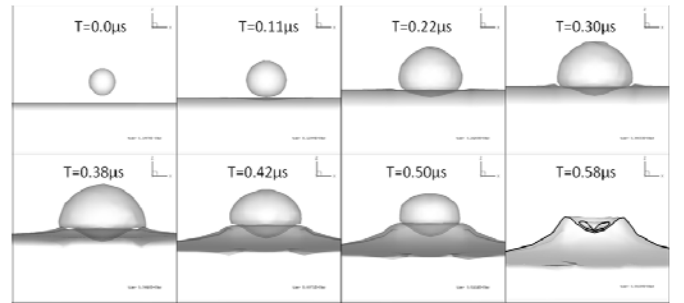


Figure 16. Snapshots for the deformation and bubble shape for the initial standoff $X=1.5R_0$ and the elastic modulus $E=10\text{kPa}$. $R_0=2\mu\text{m}$, $f=2\text{MHz}$, $P_a=1 \text{ MPa}$.

Figure 16 shows sequential snapshots of the tissue deformation and bubble shapes for an initial standoff $X = 1.5R_0$ ($3\mu\text{m}$) and $E = 10 \text{ kPa}$. Figure 17 shows the corresponding bubble equivalent radius and the 3D view of the tissue surface shape at collapse. Initially, while growing, the bubble pushes in

and dimples the tissue locally, while the surrounding low pressure sucks the tissue surface towards the bubble.. When the positive half cycle of the pressure starts, the growth rate is reduced and at approximately 3/4 cycle the bubble reaches its maximal size and then collapses forming a reentrant jet towards the much raised surface of the material. For this case, a reentrant jet is formed toward the tissue at the end of the collapse as shown in the 3D view in Figure 17.

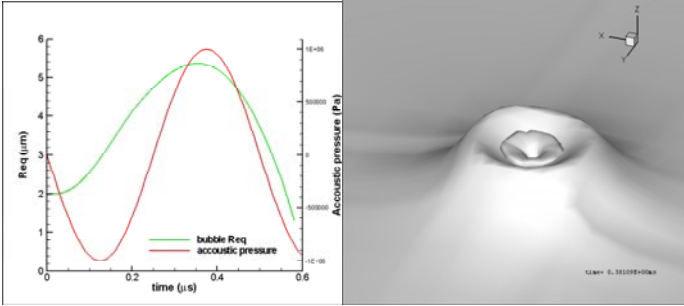


Figure 17. Equivalent bubble radius Req (left) and the 3D view of the tissue surface shape at the bubble collapse (right) for the initial standoff $X=2R_0$ and the elastic modulus $E=10\text{kPa}$. $R_0=2\mu\text{m}$, $f=2\text{MHz}$, $P_a=1\text{ MPa}$.

Figure 18 shows snapshots of the tissue deformation and bubble shapes for similar conditions but with an initial standoff $X = 3.0R_0$ ($6\mu\text{m}$) and an elastic modulus $E = 1,000\text{kPa}$. Figure 19 shows the corresponding equivalent bubble radius and the 3D view of the tissue surface shape at the bubble collapse for this case. Compared with the case shown above, since the bubble is farther away from the tissue, the suction effect is much weaker and it takes a longer time for the bubble to touch the tissue. At the same time, the bubble size varies with time due to the pressure change. The bubble collapses on the tissue surface after two pressure cycles. The overall tissue deformation is less than that for $E = 10\text{kPa}$ case and there is no crater in this case.

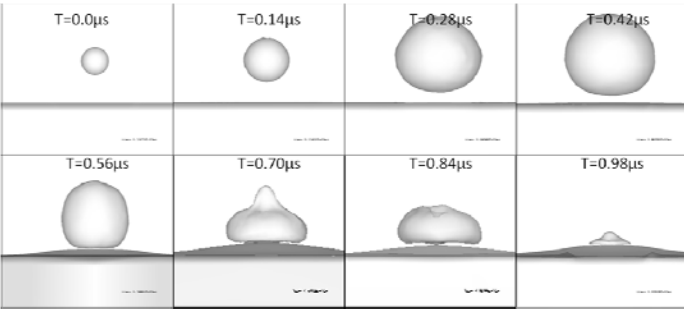


Figure 18. Snapshots for the deformation and bubble shape for the initial standoff $X=3R_0$ and the elastic modulus $E=10^3\text{kPa}$. $R_0=2\mu\text{m}$, $f=2\text{MHz}$, $P_a=1\text{ MPa}$.

The bubble shapes and tissue deformation at bubble collapses for different elastic modules and initial standoff distances are shown in Figure 20. For all the cases shown, the tissue ends up with a bulge and the overall bulge size decreases as the rigidity increases.

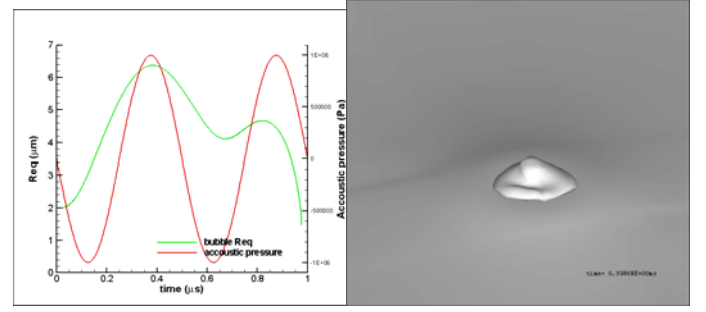


Figure 19. Equivalent bubble radius Req (left) and the 3D view of the tissue surface shape at the bubble collapse (right) for the initial standoff, $X=3R_0$ and the elastic modulus $E=1,000\text{kPa}$.

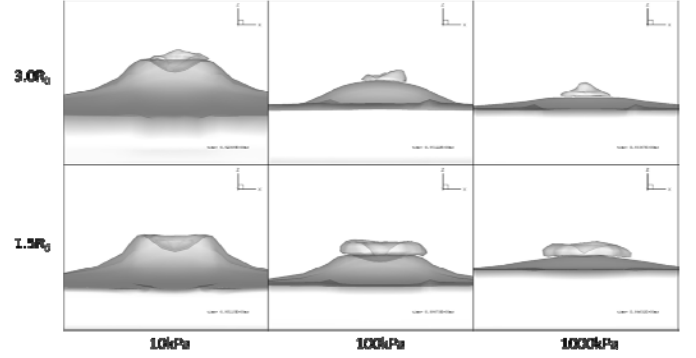


Figure 20. Side view of the tissue deformation at different elastic modulus and initial standoff distance conditions.

6.4. Bubble Dynamics in a Tube.

Simulations of a bubble dynamics in a flexible tube were carried out for studying the dynamics of a cavitation bubble inside a blood vessel simulated as a circular tubular linear elastic material with density 0.96 g/cm^3 . The Young's modulus is set at 1.08MPa and the Poisson ratio at 0.499 . The dynamics of a bubble initially spherical and initially placed at an off center location inside the circular tube is shown in Figure 21 (side and top views). As the bubble size expands, it pushes the liquid and the tube outward. As it collapses, two jets aligned with the tube center axis form on the bubble. This creates large pressures at the vessel wall, causing it to deform significantly.

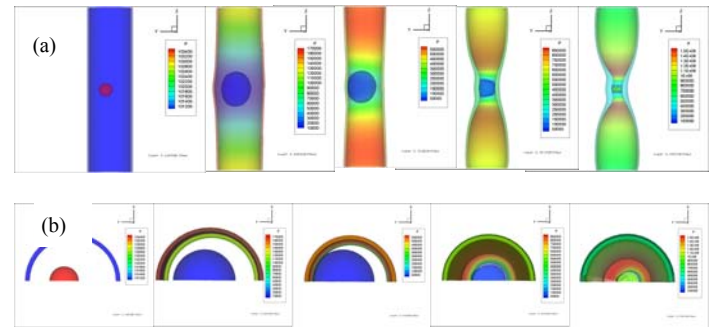


Figure 21. Pressure field for a bubble collapse in blood vessel: (a) side view at center cross cut plane, (b) top view

To illustrate the effect of the wall flexibility on the bubble dynamics, Figure 22 compares for the same geometry and initial conditions a rigid and a flexible tube ($\rho=1.0\text{ g/cm}^3$, $E=2.017\text{MPa}$

and $\nu = 0.48$). The inner radius of the tube is 0.15mm, the outer radius is 0.32mm, and the length is 1.25mm. A 20 μ m bubble is placed at the center of the tube. As shown in the figure, in the flexible tube the bubble expands slightly faster, reaches a slightly larger maximum volume, while the motion of the wall causes oscillation. Then the bubble collapses slower and the jet takes longer time to develop.

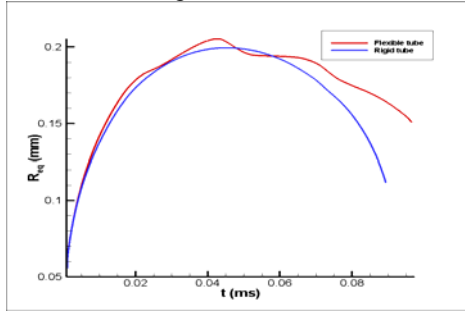


Figure 22. Bubble equivalent radius versus time inside flexible and rigid tubes with a diameter of 50 μ m for $R_0=20\mu$ m, $R_{max}=200\mu$ m and $P_{amb}=1$ atm.

As for the case of the confined bubbles between two plates, for a finite tube the length affects the bubble dynamics significantly for the same reasons. Figure 23 shows for a rigid tube the effect of the tube length. The bubble period continues to increase as the tube length is increased and it is essential to know the correct dimensions to conduct an accurate experiment or a correct modeling. This again is due to the changes in the inertia of the liquid entrained by the motion of the bubble in the tube.

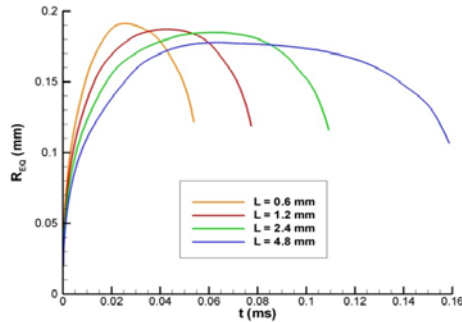


Figure 23. Tube length effect on bubble dynamics inside a rigid tube with a diameter of 50 μ m for $R_0=20\mu$ m, $R_{max}=200\mu$ m and $P_{amb}=1$ atm.

7. CONCLUSIONS

We have presented in this communication our on-going efforts to develop computational tools to enable the study of the complex interaction between acoustic forcing, natural or encapsulated microbubbles, confinement areas, tissues, and vessels. To be able to do so, three-dimensional descriptions of the dynamics are required and involve viscous flow modelling, large free surface deformations, large free surface oscillations, as well as fully coupled fluid-structure interaction capabilities. We have mainly described the methods applied and illustrated this with some examples. We used these examples to discuss some physical aspects of the problems studied.

Concerning the dynamics of microbubbles encapsulated with a highly viscous liquid shell, it appears that the shell exerts a strong effect on the stability of the microbubble making the

formation of a re-entrant jet more difficult. Indications are that the breakup mechanism for a thick-shelled microbubble near a wall may be dominated by drainage of the film around the bubble in the bubble region closer to the wall as opposed to re-entrant jet breakup for a regular microbubble. We have also presented here a diagram, which illustrate that the breakup mechanism depends highly on the combination shell thickness and standoff of the bubble from the boundary.

Numerical modelling of bubble dynamics near tissues is dominated by the use of the appropriate constitutive properties of the modelled tissue. The examples we have shown here indicate that an elastically deforming material experiences strong extensions and compressions indicating potential for both invagination and poration. Accurate modelling requires better understanding of the tissue properties and the proper mechanical models to be used.

The numerical tools presented here are very useful in helping design advanced concepts and conduct experiments such as those involving tandem microbubbles. Effects such as confinement, interaction between the bubbles, and deformation of the boundaries can be accurately studied and desirable outcome for a new design can be predicted quite accurately. Finally, such studies illustrate the need for accurate experimental definition of the conditions to enable correct simulation setups.

ACKNOWLEDGMENTS

This work was supported by the National Institute of Biomedical Imaging and Bioengineering at NIH, under SBIR Phase I and Phase II programs. Several people at DYNALOW have significantly contributed to these studies including Dr. Quan Zhang and Dr. Jie Zhang, which we thank for their efforts and contributions. Dr. Zhong, Duke University, shared with us the experimental results of his group and enabled our comparison with the impressive results they have achieved. We are grateful for this cooperation.

REFERENCES

- 1 Melville, W.K., Loewen, M.R., and Lamarre, E., "Bubbles, Noise and Breaking Waves: A Review of Laboratory Experiments", Natural Physical Sources of Underwater Sound: Sea Surface Sound (2), Kerman, B.R., ed., Kluwer, Dordrecht, 483-501, 1993.
- 2 G.L. Chahine, "Numerical Simulation of Bubble Flow Interactions" Journal of Hydrodynamics, Vol. 21 (3), pp 316-332, June 2009
- 3 Haines, J. R., Riemer, B. W., Felde, D. K., Hunn, J. D., Pawel, S. J., and Tsai, C. C., "Summary of cavitation erosion investigations for the SNS mercury target", Journal of Nuclear Materials, Volume 343, Issue 1-3, p. 58-69., 2005.
- 4 Arndt, R.E.A., "Cavitation in Fluid Machinery and Hydraulic Structure," Annual Review of Fluid Mechanics, 13, 273-328, 1981.
- 5 Tchobanoglous G., Wastewater Engineering: Treatment, Disposal, Reuse, 2nd Ed., Metcalf & Eddy, 1979.
- 6 Miller, D.L., "A Review of Ultrasonic Bioeffects of Microsonation, Gas-Body Activation, and Related

- Cavitation-Like Phenomena,” *Ultrasound in Medicine and Biology* 13, 443-470, 1987.
- 7 Pishchalnikov, Y.A., Sapozhnikov, O.A., Bailey, M.R., Williams, J.C., Cleveland, R.O., Colonius, T. Crum, L.A., Evan A.P., and McAteer J.A., “Cavitation bubble cluster activity in the breakage of kidney stones by lithotripter shockwaves,” *J Endourol* 17, 435-446, 2003.
 - 8 Rooney, J.A., “Hemolysis near an Ultrasonically Pulsating Bubble,” *Science* 169, 869-871, 1970.
 - 9 Miller, D.L., Gies, R.A., Chrisler, W.B., “Ultrasonically Induced Hemolysis at High Cell and Gas Body Concentration in a Thin-Disc Exposure Chamber,” *Ultrasound in Med. & Boil.* 13, 625-633, 1997.
 - 10 Evan, A.P. and Willis, L.R., “Extracorporeal Shock Wave Lithotripsy: Complications. In: Smith’s Textbook on Endourology,” Smith AD, Badlani GH, Bagley DH, Clayman RV, Docimo SG, Jordan GH, Kavoussi LR, Lee BR, Lingeman JE, Preminger GM, Segura JW (eds), Hamilton, Ontario, Canada, BC Decker, Inc, pp: 353-365, 2007.
 - 11 McAteer, J.A. and Evan, A.P., “The Acute and Long-Term Adverse Effects of Shock Wave Lithotripsy,” *Semin Nephrol* 28: 200-213, 2008.
 - 12 Delius, M., “Medical Applications and Bioeffects of Extracorporeal Shock Waves,” *Shock Waves* 4, 55-72 , 1994.
 - 13 Knapp, P.M., Kulb, T.B., Lingeman, J.E., et al. “Extracorporeal Shock Wave Lithotripsy Induced Perirenal Hematomas,” *J. Urol.*, 139, 700-703, 1988.
 - 14 Silberstein, J., Lakin, C.M., Parsons, L. K., “Shock Wave Lithotripsy and Renal Hemorrhage,” *Reviews in Urology*, 10 (3), 236-241.
 - 15 Evan, A. et al., “Renal trauma and the risk of long-term complications in shock wave lithotripsy,” *Nepron*, 78, 31-8, 1998.
 - 16 Evan, A. and McAteer, J.A., “Q-effects of Shock Wave Lithotripsy”, in *Kidney Stones: Medical and Surgical Management*, Coe FL, Favus MJ, Pak CYC, Parks JH, Preminger GM (eds): Philadelphia, Lippincott-Raven Press 1996, 549-570.
 - 17 Dalecki, D., Raeman, C.H., Child, S.Z., Penney, D.P., Mayer, R., Cartensen, E.L., “The Influence of Contrast Agents on Hemorrhage Produced by Lithotripter Field,” Xing, C., Gracewski, S., Carstensen, E.L., *Ultrasound in Med. & Boil.* 23, 1435-1439, 1997.
 - 18 Zhong, P., Cioanta, I., Zhu, S., Cocks, F.H., Preminger, G.M., “Effects of Tissue Constraint on Shock Wave-Induced Bubble Expansion in vivo,” *J. Acoust. Soc. Am*, 104 (5), 3126-3129, 1998.
 - 19 Chen, H., Brayman, A.A., Bailey, M.R., Matula, T.J., “Blood Vessel Rupture by Cavitation,” *Urol Res.* 39, 321-326, 2010.
 - 20 Chang, P.P., Chen, W.S., Mourad, P.D., Poliachik, S.L. & Crum, L.A., “Thresholds for inertial cavitation in Albunex suspensions under pulsed ultrasound conditions,” *IEEE Trans Ultrason. Freq. Control.* 48, 161-170, 2001.
 - 21 Chen, W.S., Matula, T. J., Brayman, A.A. & Crum, A.A., “A Comparison of the fragmentation thresholds and inertial cavitation doses of different ultrasound contrast agents,” *J. Acoust. Soc. Am.* **113** (1), 643-651, 2003.
 - 22 Neuhausel DJ, “Lithotripsy, a Survey”, *Journal of Clinical Engineering*, 12, 283-295, 1987.
 - 23 Clark, J.Y., Thompson, I.M. and Optenberg, S.A., “Economic Impact of Urolithiasis in the United States,” *J Urol.* 154, 2020-2024 (1995).
 - 24 Zhong, P., Cocks, F.H., Cioanta, I., and Preminger G.M, “Controlled, Forced Collapse of Cavitation Bubbles for Improved Stone Fragmentation During Shock Wave Lithotripsy,” *Journal of Urology: Investigative Urology*, 158, 2323-2328, 1997.
 - 25 Zhong, P., Xi, X.F., Zhu, S., Cocks, F.H., and Preminger G.M. “Recent Developments in SWL Physics Research”, *Journal of Endourology*, 13(9), 611-617, 1999a.
 - 26 Gracewski, S.M, Miao, H., Dalecki, D., “Ultrasonic Excitation of a Bubble near a Rigid or Deformable Sphere: Implications for Ultrasonically Induced Hemolysis,” *J. Acoust. Soc. Am.*, 117 (3), 1-8, 2005.
 - 27 Chahine, G. L. & Duraiswami, R. “Method For Calculating 2-D and 3-D Underwater Explosion Bubble Behavior in Free Water and Near Structures,” *NSWC Dahlgren Division Report NSWCDD/TR-93/44*, 1993.
 - 28 Chahine, G. L., Duraiswami, R. & Kalumuck, K. M., “Boundary Element Method For Calculating 2-D and 3-D Underwater Explosion Bubble Loading On Nearby Structures Including Fluid-Structure Interaction Effects,” *NSWC Dahlgren Div. Rpt. NSWCDD/TR-93/46*, 1997.
 - 29 Miao, H., Gracewski, S.M, Dalecki, D., “Ultrasonic Excitation of a Bubble Inside a Deformable Tube: Implications for Ultrasonically Induced Hemorrhage,” *J. Acoust. Soc. Am.*, 124 (4), 2374-2384, 2008.
 - 30 Chahine, G.L., “Cavitation Dynamics at Microscale Level,” *Journal of Heart Valve Disease*, Vol. 3, 102-116, 1993
 - 31 Chahine, G.L., “Numerical Studies of the Interaction of Multiple Underwater Explosion Bubbles” *73rd Shock and Vibration Symposium*, Newport, RI, November 18-22, 2002.
 - 32 Chahine, G.L. and Duraiswami, R., “Dynamical Interactions in a Multi-Bubble Cloud,” *Journal of Fluids Engineering*, 114(4), 680-686, 1992.
 - 33 Sankin, G.N., Yuan, F., Zhong, P., “Pulsating Tandem Microbubble for Localized and Directional Single Cell Membrane Poration,” *Phys. Rev. Lett.*, 105 (7), 2010.
 - 34 Unger, E., McCreery, T.P., Sweitzer, R., Caldwell, V. & Wu, Y., “Acoustically active lipospheres containing paclitaxel: A new therapeutic ultrasound contrast agent,” *Invest Radio*, 12, 886-892, 1998.
 - 35 Chahine, G.L., “Experimental and asymptotic study of nonspherical bubble collapse,” *Applied Scientific Research*, 38, 187-197, 1982.
 - 36 Zhang, S., Duncan, J. H., & Chahine, G.L., “The final stage of the collapse of a cavitation bubble near a rigid wall,” *J. Fluid Mech.*, 257, 147–181, 1993.
 - 37 Church, C.C., “The effects of an elastic solid surface layer on the radial pulsations of gas bubbles,” *J. Acoust. Soc. Am.*, 97(3), 1510-1521, 1995.
 - 38 Allen, J.S., Kaneko, Y., Yoshizawa, S. & Matsumoto, Y., “Development and appliation of contrast agent model,” *Fifth International Symposium on Cavitation*, Osaka, Japan, November 1-4, 2003.

- 39 Hoff, L., Sontum, P.C. & Hovem, J.M., "Oscillations of polymeric microbubbles: Effect of the encapsulating shell," J. Acoust. Soc. Am., 107(4), 2272-2280, 2000.
- 40 Ma, J., Yu, J., Fan, Z., Zhu, Z., Gong, X. & Du, G., "Acoustic nonlinearity of liquid containing encapsulated microbubbles," J. Acoust. Soc. Am., 116(1), 186-193, 2004.
- 41 Sarkar, K., Shi, W.T., Chatterjee, D. & Forsberg, F., "Characterization of ultrasound contrast microbubbles using in vitro experiments and viscous and viscoelastic interface models for encapsulation," J. Acoust. Soc. Am., 119(1), 2005.
- 42 Allen, J.S., May, D.J. & Ferrara, K.W., "Dynamics of therapeutic ultrasound contrast agents," Ultrasound in Med. & Biol., 29(6), 805-816, 2002.
- 43 May, D. J., Allen, J.J. & Ferrara, K.W., "Dynamics and fragmentation of thick-shelled microbubbles," IEEE Transactions on Ultrasonics, Ferroelectrics, and Frequency Control, 49(10), 1400-1410, 2002.
- 44 Hsiao, C.-T., Lu, X. and Chahine, G. L., "Three-Dimensional Modeling of the Dynamics of Therapeutic Ultrasound Contrast Agent," Ultrasound in Med. & Biol, 36 (12), 2065-2079, 2010.
- 45 Chahine, G.L., "Interaction between an oscillating bubble and a free surface," Journal of Fluids Engineering, 99, 709-716, 1977.
- 46 Chahine, G.L., Perdue, T.O. & Tucker, C.B., "Interaction between underwater explosion bubble and a solid submerged body," DYNAFLOW INC. Technical Report 89001-1, August. 1989.
- 47 Hsiao, C.-T., Lu, X. Z, and Chahine, G. L.. (2007), "3D Modelling of the dynamics of therapeutic ultrasound contrast agents," DYNAFLOW, INC. NIH SBIR Phase I final Technical Report 2M6018-NIH-1.
- 48 Von Maltzahn WW and Besdo D. Wiemer W, "Elastic Properties of Arteries: A Nonlinear Two-Layer Cylindrical Model," J Biomech, 14, 389-397, 1981.
- 49 Daoud, M.I., Lacefield, J.C., "Three-Dimensional Computational Modeling of High-Frequency Ultrasound Imaging of Murine Liver and Liver Metastases," J. Acoust. Soc. Am., 128 (4), Pt.2, 2364, 2010.
- 50 Chorin, A. J., "A numerical method for solving incompressible viscous flow problems," Journal of Computational Physics, 2, 12-26, 1967.
- 51 Roe, P. L., "Approximate Riemann solvers parameter vectors and difference schemes," Journal of Computational Physics, 43, 357-372, 1981.
- 52 van Leer, B., "Towards the ultimate conservative difference scheme. Second order sequel to Godunov's method," Journal of Computational Physics, 32, 101-136, 1979.
- 53 Vanden, K. & Whitfield, D. L., "Direct and iterative algorithms for the three-dimensional Euler equations," AIAA-93-3378, 1993.
- 54 Wardlaw, A.B., Luton, J.A., Renzi, J.R., Kiddy, K.C., McKeown, R.M., "The Gemini Euler Solver for the Coupled Simulation of Underwater Explosions" NSWCIHD/IHTR-2500, 2003.
- 55 Chahine, G. L., "Numerical and experimental study of explosion bubble crown jetting behavior." Dynaflow, Inc. Technical Report 96003-1-ONR., 1997.
- 56 Chen, H., et al., "Blood vessel rupture by cavitation," Urological research, p. 1-6, 2010.
- 57 Ohl, S., E. Klaseboer, and B. Khoo, "The dynamics of a non-equilibrium bubble near bio-materials," Physics in Medicine and Biology, 54: p. 6313, 2009

High Intensity Focused Ultrasound – a Powerful Technique

Gail ter Haar* Joint Department of Physics, Institute of Cancer Research: Royal Marsden Hospital,
Sutton, Surrey, UK

gail.terhaar@icr.ac.uk

ABSTRACT

It is assumed that diagnostic ultrasound as used for imaging the fetus *in utero* is harmless for the baby, and this despite the fact that only 20-40% of the energy transmitted through the maternal skin is used to form the image, the rest remaining in the tissue through which it passes. The energy levels used in most forms of diagnosis are sufficiently low (~20mW) that its safety is a reasonable assumption. However, if the incident acoustic power is significantly increased, then the absorbed energy may be used to therapeutic advantage. This is the case for physiotherapy ultrasound where temperature rises of ~2-3°C are sought, for hyperthermic treatments of cancer where an increase of 6-8 °C are required, and for High Intensity Focused Ultrasound (HIFU) where temperatures in excess of 56°C are needed. Power levels of ~ 200W are used for HIFU, ~10,000 times those used in imaging.

In HIFU, a high power ultrasound beam is focused at a distance from its source using either geometric or electronic beam shaping. The focused nature of the HIFU beam has the potential to provide a non-invasive treatment of deep-seated tumours. When large tumours are the target for destruction, the focused beam is moved so as to “paint out” the required volume with the focal region.

HIFU has been shown to be a useful technique for the treatment of tumours of the prostate, kidney, liver, breast, pancreas and bone. First treatments have recently been carried out in the brain. Despite the very large numbers of patients that have been exposed to HIFU (>800,000) large scale clinical trials have not so far been undertaken in the West, apart from in the prostate, but early indications are encouraging.

1. INTRODUCTION

By far the most common application of ultrasound in medicine is its use for imaging and diagnosis. Here, it has an unprecedented safety record, with no epidemiological evidence of harm, the only confirmed effect being an increase in left handedness in boys.

In fact, the therapeutic potential of ultrasound waves was explored before its diagnostic uses, and it was known in 1928 that it could produce effects in biological models [1]. The heating potential of an ultrasound beam was well recognized,

and Horvath [2] was one of the first to suggest that ultrasound beams might have potential benefit in cancer therapy. In the 1950's the Fry brothers in Illinois were looking for a method of destroying selective regions of the brain for neuro-behavioural studies. Their solution was to use highly focused, high intensity beams to create localized thermal damage [3]. In the 1950's this technique, which came to be known as High Intensity Focused Ultrasound (HIFU) was used clinically with some success for the treatment of Parkinson's disease and in the early 1970's for the treatment of glaucoma, but the introduction at the same time of the drug L-dopa for Parkinsonism and of lasers in ophthalmology meant that HIFU fell out of favour [4,5]. Recently there has been an upsurge in interest, with HIFU's potential for the treatment of malignant and benign tumours being actively investigated in the clinic.

2. PRINCIPLES OF HIFU

An ultrasound beam may be focused using a plane transducer fronted by a lens or a bowl shaped element. A more commonly used alternative uses a multi-element phased array that can be focused and steered electronically [6]. The beam characteristics are determined by the transducer geometry and ultrasound frequency. For the treatment of deep seated tumours, long focal lengths (typically 8-15cm) are chosen, and frequencies of 0.8 – 1.7 MHz. When closer targets are of interest for example, the prostate (when treated *per rectum*), then shorter focal lengths and higher frequencies are preferred (3-4 MHz, focal lengths 3-6 cm).

The principle of HIFU is that the peak of the focused ultrasound field is placed within the tissue volume of interest. If the intensity is sufficiently high, the temperature within the focal volume is raised to cytotoxic levels, but the intensity elsewhere in the field is insufficient to cause cell damage. It is well known from tissue hyperthermia studies that temperatures of 56°C held for 2 seconds lead to instantaneous cell death. At these temperatures the same effect is obtained by halving the heating time and raising the temperature by 1°C. This temperature – time relationship is believed to be valid for temperatures above 43°C, and is incorporated into the concept of thermal dose, which is often used to describe HIFU treatments. For conventional hyperthermia treatments, synergistic effects with radiotherapy and chemotherapy are sought when temperatures of 43°C are maintained for an hour.

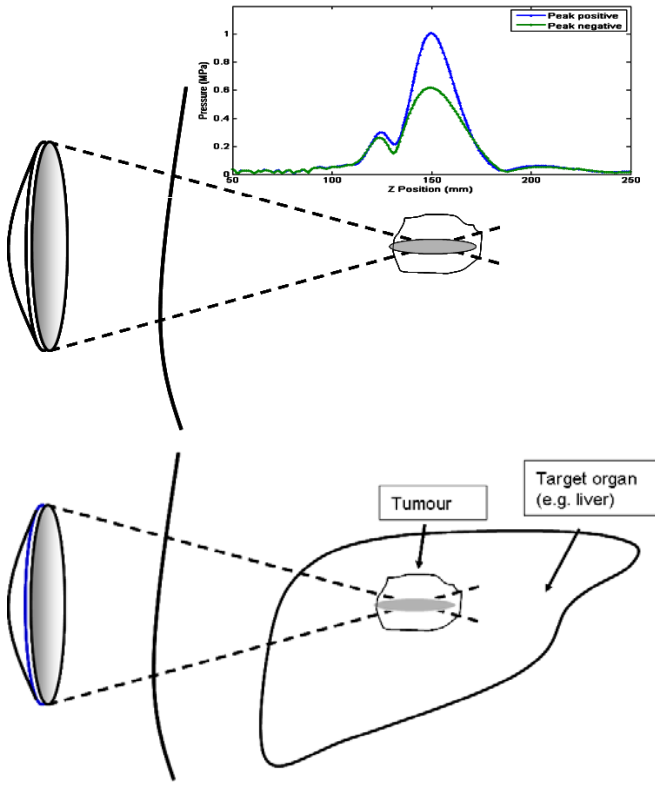


Fig 1. top. Principle of HIFU. bottom. Schematic showing the pressure distribution on the beam axis. Tissue destruction only occurs within the focal region.

Heat treatments are therefore often referred to in terms of equivalent time at 43°C, t_{43} , where

$$t_{43} = tR^{T_{43}-T} \quad (1)$$

is the time at 43°C that will produce an equivalent thermal effect as a temperature T maintained for a time t [7]. R is a constant which has been shown to be 2 for $T > 43^\circ\text{C}$ and 4 for $T < 43^\circ\text{C}$. For thermal ablation treatments such as HIFU, a t_{43} of 240 minutes is often used as an indicator of successful damage.

The amount of tissue heating obtained is related to the acoustic intensity. In a plane wave, the relationship between the intensity incident on the surface of tissue (I_0) and the intensity at a depth x into tissue ($I(x)$) may be written as:

$$I(x) = I_0 e^{-\mu x} \quad (2)$$

Where μ , the intensity attenuation coefficient, is a sum of contributions from absorption (μ_a) and scatter (μ_s) such that $\mu = \mu_a + \mu_s$. The contribution of absorption to attenuation may be 60-80% of the total. The rate of heat deposition, \dot{Q} , is given by the expression $\dot{Q} = \mu I$ per unit volume. If there is no heat loss out of the volume by conduction, convection or radiation, this may also be written as:

$$\dot{Q} = \rho C \frac{dT}{dt} \quad (3)$$

where ρ is the density, C is the heat capacity and $\frac{dT}{dt}$ is the rate of temperature change. By combining these equations, we get $\frac{dT}{dt} = \frac{\mu I}{\rho C}$ (4). The attenuation coefficient, μ , is frequency dependent, varying approximately as $\mu = \mu_0 f^{1.1}$. The choice of frequency for HIFU treatments therefore becomes a compromise between a sufficiently low frequency to reach clinically useful depths in tissue, and one that is sufficiently high to achieve cytotoxic temperatures when absorbed by tissues at the focus [8]. It has been shown that focal intensities in excess of 1000 W cm^{-2} are required for frequencies of 1-2 MHz.

The distribution of intensity along and transverse to the axis at the focus is approximately Gaussian, and ablation is achieved out to the radius at which the required thermal dose is reached. The damaged tissue volume is referred to as a “lesion”. The temperature at the centre of the lesion may rise to a level at which tissue water boiling occurs. An additional cell damage mechanism in the ultrasound field is acoustic cavitation. Cavitation may occur wherever the negative pressure amplitude exceeds the threshold required for bubble nucleation. This is likely to occur first at the beam focus. It has been shown that bubble activity is associated with enhanced local heating [9].

It has been shown using histological methods that the margin between live and dead cells at the lesion’s edge is ~6 cells wide [10]. Figure 2. shows histology from a lesion. The very sharp demarcation between live and dead cells can be clearly seen. Apoptotic cells are seen in this region 6 hours after HIFU treatment. The cells in the centre of the lesion are heat fixed. In order to take full advantage of the highly localised nature of tissue destruction, it is important to have excellent treatment guidance and monitoring ability. Both ultrasound and magnetic resonance imaging (MRI) have been used for this. Each has its own advantages and disadvantages. MRI arguably provides better anatomical imaging, but ultrasound provides information in real time. Treatment monitoring with MRI uses contrast enhanced T1w images to show the ablated volumes, whereas that with ultrasound relies on the creation of aggregations of gas bubbles (whether from tissue water boiling or clusters of bubbles formed by acoustic cavitation) to show tissue destruction by the enhanced back scatter that results. Currently, only MR thermometry is available clinically. Ultrasound based thermometry is still only experimental.

3. APPLICATIONS OF HIFU

Clinical uptake of HIFU is still in its infancy. Multi-centre trials of MR guided ablation of uterine fibroids have yielded good results, and this treatment is becoming more readily available [11]. The only cancer application of HIFU that is in common clinical use at present is for the treatment of prostate cancer. This ultrasound guided technique uses a combined imaging and therapy trans-rectal probe. The treatment usually only involves a single treatment, under light general anaesthetic. Imaging of prostate cancer is extremely difficult, and it is not possible to see the tumour foci using diagnostic ultrasound techniques. The goal of these treatments is therefore either the destruction of the whole gland, or partial ablation of regions

known to contain cancer. The precise nature of the damage allows sparing of the neurovascular bundles, thus reducing side effects. Although it is early days, long term results with prostate HIFU are looking promising [12].

Both ultrasound and MR guided HIFU are being explored for tumour treatment in a number of other organs. The non-invasive nature of the treatment renders it of particular interest for targeting cancer in the liver, kidney and pancreas [13]. Figure 2 shows an example of a kidney treated through the intact skin using a single treatment under light general anaesthetic. The lack of uptake of contrast agent a year after treatment indicates the loss of blood supply to the tumour, and tissue death. A considerable challenge lies in passing sufficient ultrasound energy through the rib cage to reach deep seated abdominal tumours, while retaining a focus, and without depositing too much energy at the rib surface, causing local tissue damage. Bone presents a significantly higher acoustic impedance than tissue, and thus incident ultrasound energy is reflected strongly at its surface. In addition, ultrasound energy is rapidly absorbed by bone, with the creation of shear waves. No definitive solution has, as yet, been found to the rib problem, although the use of time reversal (adaptive focusing) techniques to provide transmission of a focused beam through the skull bone has opened the possibility of using HIFU in the treatment of brain disorders. This technique uses a large area transducer to reduce the incident power at the skull surface, thus reducing the probability of deleterious effects. Here, the ability to damage a closely defined region selectively while sparing overlying tissue is of particular importance [14]. There is increasing evidence that HIFU can also provide pain palliation, with especial interest in reducing pain resulting from bone metastases [15]. New clinical non-cancer applications are under investigation, with the reduction of benign tumours of the parathyroid, cardiac ablation and the treatment of glaucoma being the most advanced [16-18].

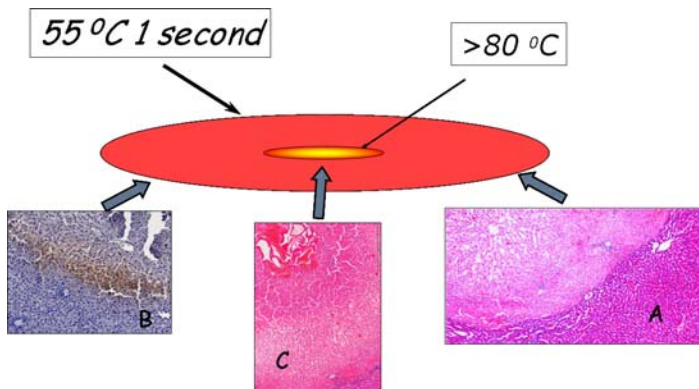


Fig. 2. The boundary of the HIFU lesion is defined by the contour at which the temperature has been maintained at 55°C or greater for 1 second or longer. (A) Haematoxylin & Eosin (H&E) stain showing the microscopic appearance of the boundary of the lesion in rat liver – the darker region is viable tissue. (B) Cleaved caspase 3 stain of lesion boundary, 6 hours after exposure, showing the rim of apoptotic cells. (C) H & E stain showing the centre of the lesion, and tissue disruption

caused by tissue water boiling. (pictures courtesy of Chaturika Jayadewa)

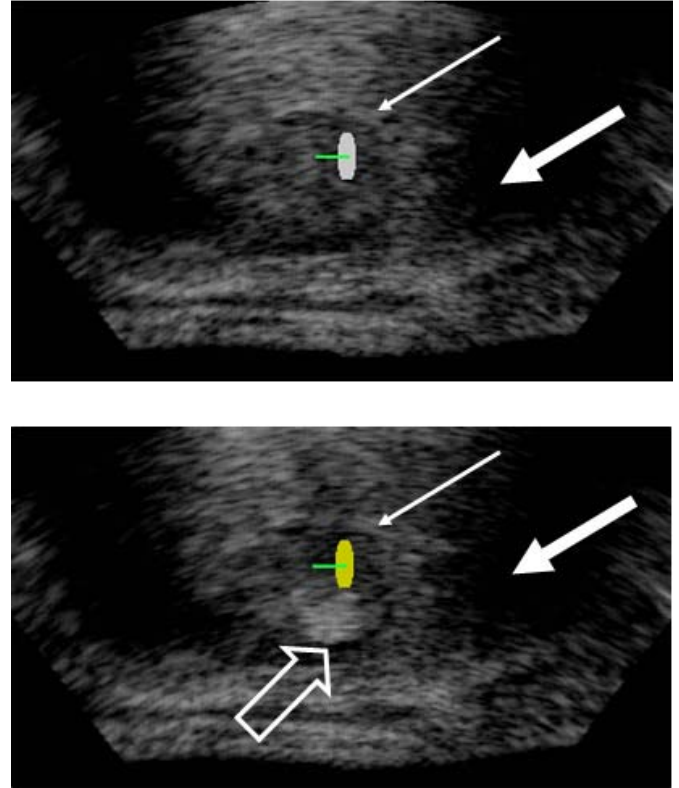


Fig. 3 Ultrasound image of a tumour of the liver (narrow arrows). The shadow cast by the ribs can be clearly seen (thick arrows), as can the skin surface (bottom of scan). Top image shows the tumour before HIFU exposure, lower image shows the tumour following exposure, with the hyperechoic region where treatment is complete (hollow arrow) being clearly evident.

4. CONCLUSIONS

HIFU has considerable potential to give good clinical benefit for a number of applications. However, with the exception of prostate treatments, the current lack of large scale long term clinical trials means that clinical evidence for its efficacy is weak at this stage, with results being largely anecdotal. As the number of available HIFU devices increases, this situation should change. HIFU offers the potential for single treatments on a day case basis for many tumours. Its non-invasive nature makes it a particularly attractive treatment option.

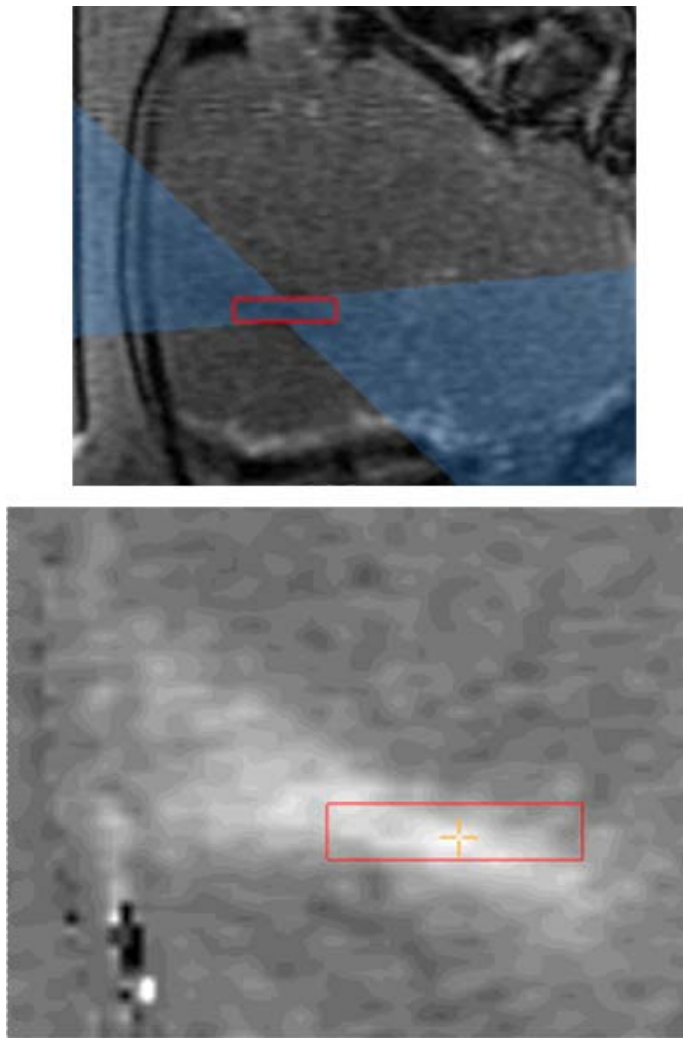


Fig.4 T1 weighted MR image showing the entry of the HIFU beam into a uterine fibroid (top), and the subsequent image of the treated tissue (bottom)

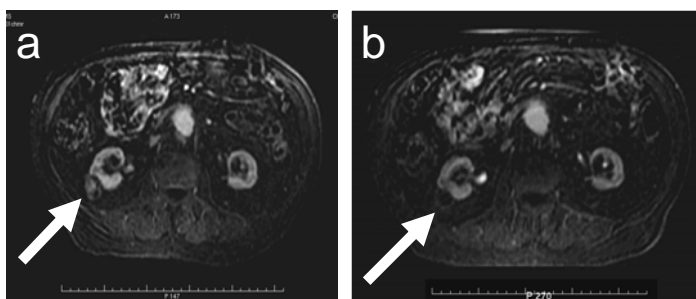


Fig.5 Contrast enhanced T1 weighted MR images showing a kidney tumour before (a) and 1 year after (b) extracorporeal HIFU treatment. The absence of contrast agent uptake at a year indicates the lack of viable tissue. (Courtesy of D.Cranston Churchill Hospital, Oxford)

REFERENCES

1. Harvey, E.N. and Loomis, A.L. (1928). High frequency sound waves of small intensity and their biological effects. *Nature* 121, 622.
2. Horvath, J. (1944). Ultraschallwirkung beim menschlichen Sarkom. *Strahlentherapie* 75, 119–125.
3. Fry WJ, Mosberg Jr WH, Barnard JW, Fry FJ. (1954) Production of focal destructive lesions in the central nervous system with ultrasound. *J Neurosurg.*11, 471-8.
4. Ballantine, H.T., Bell, E. and Manlapaz, J. (1960). Progress and problems in the neurological application of focused ultrasound. *J. Neurosurg.* 17, 858–876.
5. Lizzi FL, Coleman DJ, Driller J, Franzen LA, Jakobiec FA. (1978) Experimental, ultrasonically induced lesions in the retina, choroid, and sclera. *Investigative Ophthalmology & Visual Science.*17, 350-60.
6. ter Haar GR, Coussios CC. (2007) High Intensity Focused Ultrasound (HIFU): physical principles and devices. *Int. J. Hyperthermia* 23, 89-104
- 7 Sapareto DG, Dewey WC (1984): Thermal dose determination in cancer therapy. *Br J Radiation Oncology Biol Phys Med*;10,787-800
8. Hill CR (1994) Optimum acoustic frequency for focused ultrasound surgery *Ultrasound in Med & Biol.* 21, 270-277
- 9 Holt RG, Roy RA. (2001)Measurements of bubble-enhanced heating from focused, MHz-frequency ultrasound in a tissue-mimicking material. *Ultrasound in Medicine and Biology.* 27, 1399-412.
- 10 ter Haar, G.R. and Robertson, D. (1993). Tissue destruction with focused ultrasound in vivo. *Eur. Urol.* 23 (Suppl. 1), 8–11.
- 11 Shen S-H, Fennessy F, McDannold N, Jolesz F, Tempany C Image-Guided Thermal Therapy of Uterine Fibroids (2009) *Semin Ultrasound CT MRI* 30,91-104
- 12 Illing R & Chapman A. (2007) The clinical applications of high intensity focused ultrasound in the prostate. *Int. J. Hyperthermia* 23, 183-191
- 13 Leslie T & Kennedy JE. (2007) High intensity focused ultrasound in the treatment of abdominal and gynaecological diseases. *Int. J. Hyperthermia* 23, 173-182
- 14 Hynynen K & Clement G. (2007) Clinical applications of focused ultrasound - the brain. *Int. J. Hyperthermia* 23, 193-202
15. Chen W. & Zhou K. (2005) High-intensity focused ultrasound ablation: a new strategy to manage primary bone tumors *Curr Opin Orthop* 16,494-500
- 16 Esnault, O., Franc, B., Chapelon, J.-Y. (2009) Localized ablation of thyroid tissue by high-intensity focused ultrasound: Improvement of noninvasive tissue necrosis methods *Thyroid* 19, 1085-1091
- 17 Otsuka R, Fujikura K, Abe Y, Okajima K et al (2007) Extracardiac Ablation of the Left Ventricular Septum in Beating Canine Hearts Using High-Intensity Focused Ultrasound. *Am Soc Echocardiogr* 20,1400-1406
- 18 Charrel, T., Aptel, F., Birer, A., Chavrier, F., Romano, F., Chapelon, J.-Y., Denis, P., Lafon, C. (2011) Development of a Miniaturized HIFU Device for Glaucoma Treatment With Conformal Coagulation of the Ciliary Bodies *Ultrasound in Medicine and Biology* 37, 742-754